



Provided by the author(s) and University of Galway in accordance with publisher policies. Please cite the published version when available.

Title	Decoding the kinematic and ionisation structure of axisymmetric nebulae
Author(s)	Fitzgerald, Karol
Publication Date	2021-08-04
Publisher	NUI Galway
Item record	http://hdl.handle.net/10379/16890

Downloaded 2024-04-17T16:26:35Z

Some rights reserved. For more information, please see the item record link above.





OÉ Gaillimh
NUI Galway

Decoding the Kinematic and Ionisation Structure of Axisymmetric Nebulae

by

Karol Fitzgerald

A thesis submitted in partial fulfilment for the
degree of Doctor of Philosophy

in the



Centre for Astronomy

School of Physics

National University of Ireland Galway

Under the supervision of

Dr Matt Redman

Declaration

The work in this thesis is based on research carried out at the Centre for Astronomy, School of Physics, National University of Ireland, Galway. No part of this thesis has been submitted elsewhere for any other degree or qualification and it is all my own work unless referenced to the contrary in the text.

Copyright © 2021 N.U.I. Galway

“The copyright of this thesis rests with the author. No quotations from it should be published without the author’s prior written consent and information derived from it should be acknowledged.”

Acknowledgements

There are so many people that I want to thank and acknowledge in helping and supporting me along my PhD path, the three most important are firstly Liz, my wife who saw me at my lowest, helped me up and kept me going. Even with the birth of our children, Liz didn't hesitate in supporting and reminded me to enjoy and learn as much as I could. Second is my supervisor, Matt Redman, who without question is as fine a person you can meet and without doubt a supervisor I aspire to become someday. Matt's knowledge, advice, support, understanding and patience along my journey was excellent. The third is my very good friend Eamonn Harvey, who has helped me more than he will ever know. I really enjoyed our chats, walks along the river Corrib during lunch and especially the laughs along the way.

The following people have also helped hugely in my research, both academically and being supportive when it was needed, Salam Dulaimi, Eoin O Connor, Nicola Keaveney, Nevenoe Guegan, Christophe Morisset, Tracey Moore, Shane Feeney, Rhona Heenan, Lisa-Marie Browne, my GRC committee and many other academics and staff in the School of Physics, NUI Galway. I would also like to acknowledge the time and input given by those that contributed to the user-stories and evaluating PYCROSS.

People have said to me that they don't know how I managed it all, the truth is that I don't know myself, but it wouldn't have been possible without support from family, an excellent supervisor and great friends, thank you all very, very much.

I dedicate this thesis to my mum and dad who sadly, will never know my achievements, but never doubted my potential. Prior to starting my PhD I was a husband, since then I have become a father to two fantastic little men Oisín and Odhrán, the rest of my life is dedicated to you both.

"You're only given one little spark of madness.

You mustn't lose it"

— Robin Williams

Abstract

The aim of the thesis was to develop a code and pipeline for generating 3D photoionisation models of axisymmetric nebulae to better understand their observed structure and composition. This was achieved through a new code that amalgamated the features of popular (but separate) codes in astronomy; a 3D morpho-kinematic modelling application called SHAPE, a well known, large-scale spectral synthesis code called CLOUDY and PYCLOUDY, a Python library that handles CLOUDY. The resulting code presented in this thesis was called PYCROSS, an acronym for “PYCLOUDY *Rendering of SHAPE Software*”.

The steep learning curves traditionally experienced when developing and using new codes overshadows the necessity for a formal software development lifecycle. As software development and coding is becoming an essential skill for new astronomers, who are often required to create their own codes for specific purposes, employing and adhering to a software development lifecycle during developing will help meet milestones while managing complex projects, thus ensuring reliability and quality. Here, a formal software development lifecycle and test driven development approach is described and employed in the development of the PYCROSS code. A detailed account of the code development, installation, functionality, user interface and operational overview is given using both theoretical and actual stellar objects.

Creating photoionisation models for known planetary nebulae and novae can only be accomplished when there is sufficient information to determine the most significant physical parameters of the nebula and the central star. Presented here are novel approaches for various scientific methods/pipelines that can be employed with PYCROSS to generate photoionisation models. Over the course of this thesis PYCROSS has been used to develop, for the first time, 3D photoionisation models of novae V5668 Sagittarii (2015), V4362 Sagittarii (PTB 42) as well as planetary nebulae LoTr 1 and MyCn 18.

Dissemination of Research

Publications arising from this work

- *Using the Agile software development lifecycle to develop a standalone application for generating colour magnitude diagrams.*

K. Fitzgerald, L–M. Browne and R. Butler

Astronomy & Computing, Volume 28, July 2019 ([Fitzgerald et al., 2019](#))

- *Introducing PYCROSS: PYCLOUDY Rendering Of SHAPE Software for pseudo 3D ionisation modelling of nebulae.*

K. Fitzgerald, E.J. Harvey, N. Keaveney and M.P. Redman

Astronomy & Computing Volume 32, July 2020 ([Fitzgerald et al., 2020](#))

- *PYCROSS pseudo 3D ionisation modelling of planetary nebula MyCn 18*

K. Fitzgerald, M.P. Redman, E.J. Harvey, and C. Morisset

Astronomy & Computing – *In preparation*

Publications using PYCROSS code

- *Polarimetry and Spectroscopy of the ‘Oxygen Flaring’ DQ Herculis-like: V5668 Sagittarii (2015).*

E. J. Harvey, M. P. Redman, M. J. Darnley, S. C. Williams, A. Berdyugin, V. E. Piirola, **K. Fitzgerald** and E. G. P. O Connor

Astronomy & Astrophysics, Volume 611, March 2018 ([Harvey et al., 2018](#))

- *Two New Nova Shells associated with V4362 Sagittarii and DO Aquilae.*

E.J. Harvey, M.P. Redman, P. Boumis, S. Akras, **K. Fitzgerald**, S. Dulaimi, S.C. Williams, M.J. Darnley, M.C. Lam, M. Kopsacheilli and S. Derlopa.

Monthly Notices of the Royal Astronomical Society Volume, September 2020 ([Harvey et al., 2020](#))

-
- *Shock shaping, nebular spectroscopy of Nova V906 Car/ASSAN-18fv*
E.J. Harvey, E. Aydi, L. Izzo, C. Morriset, M. Shrestha, P. Molaro and **K. Fitzgerald**
Monthly Notices of the Royal Astronomical Society – *In preparation*

Other collaborative publications

- *Untangling the lightcurves of tight dwarf binaries 2MASS J1314+13AB and 2MASS J0746+20AB.*
S. Dulaimi, R. P Boyle, **K. Fitzgerald**, A. Golden and R. F Butler
Astronomy & Computing – In preparation
- *The Light Curve Fitter: A novel application for deconvolving two superimposed sinusoidal waves*
K. Fitzgerald, S. Dulaimi, R. P Boyle, A. Golden and R. F Butler
Astronomy & Computing – In preparation

Abbreviations & Acronyms

ADASS	Astronomical Data Analysis Software and Systems
ADF	Abundance Discrepancy Factor
AGB	Asymptotic Giant Branch
ALFOSC	Alhambra Faint Object Spectrograph and Camera
ASDL	Agile Software Development Lifecycle
AU	Astronomical Unit
C13 / C17	CLOUDY 13 / 17 (Version)
CEL	Collisionally Excited Lines (forbidden lines)
CMD	Colour Magnitude Diagram
CN	Classical Novae
CV	Cataclysmic Variable
FLIER	Fast Low-Ionisation Emission Regions
GISW	Generalised Interacting Stellar Winds (model)
GUI	Graphical User Interface
HRS	High-Resolution chelle Spectrograph
HST	Hubble Space Telescope
ING	Isaac Newton Group
IRAF	Image Reduction and Analysis Facility
ISM	Interstellar medium
ISSAC	Infrared Spectrometer And Array Camera
IUE	International Ultraviolet Explorer
LIS	Low Ionisation Structures
MASH	Macquarie/AAO/Strasbourg H [?] Planetary Galactic Catalog
MOCASSIN	MOnto CARlo SimulationsS of Ionised Neulae
NIR	Near Infrared
NIR	Nordic Optical Telescope
OCL	Optical Recombination Line
PNe	Planetary Nebulae (PN singular)
PNN	Planetary Nebula Nucleus

PYCross	PYCloudy Rendering of SHAPE Software
RG	Red Giant
SALT	South African Large Telescope
SDLC	Software Development Life Cycle
SDSS	Sloan Digital Sky Survey
SNR	Super Nova Remnant
SNe Ia	Super Nova Type Ia
SyNe	Symbiotic Nebulae
SySt	Symbiotic Stars
TDD	Test Driven Development
TNR	Thermo Nuclear Explosion
TP-AGB	Thermal Pulsing AGB
UML	Unified Modelling Language
VLT	Very Large Telescope
WFPC2	Wide Field & Planetary Camera 2

Contents

Declaration	ii
Acknowledgements	iii
Abstract	iv
Dissemination of Research	v
Abbreviations & Acronyms	vii
List of Figures	xii
List of Tables	xv
1 Introduction	
1.1 Introduction	2
1.2 Planetary nebulae	3
1.2.1 Evolution of planetary nebulae	6
1.2.2 Morphology & structure	11
1.2.3 Chemical composition	16
1.2.4 Shaping mechanisms	19
1.3 Symbiotic Stars	23
1.4 Novae	28
1.4.1 Types of novae	29
1.4.2 Nova shells	32
1.5 Thesis Overview	35

2	Software development in astronomy	38
2.1	Introduction	39
2.2	Modelling software	40
2.3	Software development	44
2.3.1	Programming paradigms	46
2.3.2	Agile software development	48
2.3.3	Software testing	54
2.3.4	Code freezing	56
2.4	PYCLOUDY Rendering of SHAPE Software	57
2.4.1	PYCROSS functionality	60
2.4.2	SHAPE data cube text file	65
2.4.3	User interface & operational overview	66
2.5	Summary and conclusion	70
3	PYCROSS pipeline for novae & planetary nebulae	72
3.1	Introduction	73
3.2	Modelling nova remnants	74
3.2.1	V5668 Sagittarii (2015)	75
3.2.2	V4362 Sagittarii (PTB 42)	78
3.3	Modelling PNe	81
3.3.1	Planetary nebula LoTr 1	82
3.4	Summary and conclusion	88
4	Photoionisation modelling of the Etched Hourglass Nebula – MyCn 18	90
4.1	Introduction	91
4.2	The Etched Hourglass Nebula – MyCn 18	91
4.3	SHAPE morpho-kinematic Model	98
4.4	PYCROSS photoionisation modelling	101
4.5	PYCROSS CLOUDY nebular diagnostics	108
4.6	Summary and conclusion	110

5	Summary and future work	112
5.1	Summary	113
5.2	Future work	116
	Bibliography	120

List of Figures

1.1	Stellar evolution of a star	4
1.2	Planetary nebulae	6
1.2a	M27 (Dumbbell Nebula) - The first detected PN	6
1.2b	NGC 6543 (Cat's Eye Nebula) - First spectral study of a PN	6
1.3	Internal structure and thermal pulse cycle of a AGB star	9
1.3a	AGB Structure	9
1.3b	AGB thermal pulse cycle	9
1.4	Collage of PN morphologies	10
1.5	Model to Explain the Different Shapes of Planetary Nebulae.	11
1.6	FLIER of NGC 7009 (The Saturn Nebula)	15
1.7	NGC 6543 revealing structures	16
1.8	PNe Interstellar Winds Model (Soker, 1992)	19
1.9	Evolution models for PNe (Nordhaus & Blackman, 2006)	22
1.10	Schematic of components of a symbiotic binary	24
1.11	Symbiotic Nebula: Hen2-104 (The Southern Crab Nebula)	27
1.12	Classical Nova	29
1.13	Nova light curve morphology (Bode & Evans, 2008)	30
1.14	Multi-epoch expanding novae shells (Santamaría <i>et al.</i>, 2020)	34
2.1	PNe M2-9 and SHAPE model	43
2.2	Agile software lifecycle	49
2.3	PYCROSS UML diagram	53
2.4	PYCROSS: PYCLOUDY rendering of SHAPE software	58
2.5	High-level operational overview of PYCROSS	59

2.6	PYCROSS operational flowchart GUI	60
2.7	PYCROSS colour map examples	64
2.8	PYCROSS zoom functionality	69
3.1	SHAPE model of V5668 Sgr (Harvey et al., 2018)	75
3.2	V5668 Sgr spectral line profiles & PYCROSS models Harvey et al. (2018)	76
3.3	PYCROSS scientific pipeline for nova V4632 Sgr	79
3.4	LoTr 1 SHAPE model mesh (3D module)	83
3.5	LoTr 1 slit 1 comparison	85
3.6	LoTr1 PYCROSS photoionisation cuts	86
3.7	LoTr1 PYCROSS photoionisation model - emissions 40°	87
4.1	Etched Hourglass Nebula MyCn 18 (Sahai et al., 1999)	93
4.2	HST WFPC2 images of MyCn 18 (Sahai et al., 1999)	94
4.3	Geometric analysis of MyCn 18 (Clyne et al., 2014)	96
4.4	SHAPE 3D mesh model of MyCn 18	99
4.5	Frontal view of MyCn 18 3D SHAPE model	100
4.6	3D SHAPE model & render of MyCn 18	100
4.7	SHAPE quadrant and slice of MyCn 18 input into PYCROSS	101
4.8	SHAPE data cube generation of MyCn 18	102
4.9	PYCROSS photoionisation models: [NII], H α , and [OIII]	103
4.9a	[N II] (6583Å)	103
4.9b	[N II] (6583Å)	103
4.9c	H α (6562Å)	103
4.9d	H α (6562Å)	103
4.9e	[O III] (5007Å)	103
4.9f	[O III] (5007Å)	103
4.10	NGC 6720 – The Ring Nebula	105
4.11	90° MyCn 18 photoionisation models: [O I], H I, [O III] and He II	106
4.11a	[O I] – 6300Å – 90°	106

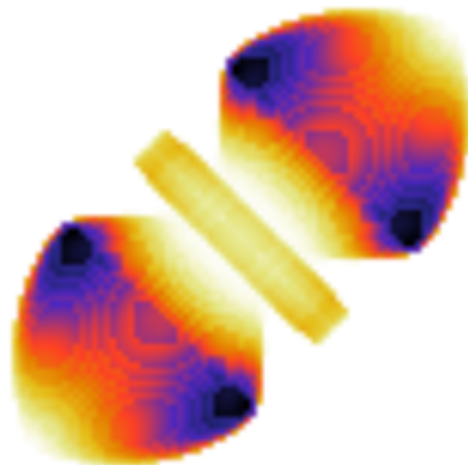
4.11b	H I – 4861Å – 90°	106
4.11c	[O III] – 5007Å – 90°	106
4.11d	He II – 4686Å – 90°	106
4.12	0° MyCn 18 photoionisation models: [O I], H I, [O III] and He II . . .	107
4.12a	[O I] – 6300Å – 0°	107
4.12b	H I – 4861Å – 0°	107
4.12c	[O III] – 5007Å – 0°	107
4.12d	He II – 4686Å – 0°	107
4.13	SHAPE model angle components	109

List of Tables

1.1	PNe Morphological Classification Codes (Sahai <i>et al.</i>, 2011)	13
1.2	Nebular and auroral T_e & N_e diagnostic line ratios (Tsamis <i>et al.</i>, 2003)	17
1.3	Binary System Classification for PNe (Soker, 1997)	20
1.4	Summarisation of PNe population synthesis models (Boyle, 2018)	21
2.1	Agile SDLC versus Traditional SDLC models (Leau <i>et al.</i>, 2012) .	52
2.2	Rubric used in deciding on the SDL for this project (Sami, 2012) .	52
2.3	PYCross class characteristics	55
2.4	Platform specific freezing codes for Python	57
3.1	PYCross case studies: development and findings	73
3.2	Table of parameters for both inner and outer shells of LoTr 1 from Tyndall <i>et al.</i> (2013)	84
4.1	C13 and C17 input emission line comparison	92
4.2	CLOUDY (C17) parameters used in PYCross	104
4.3	MyCn 18 model temperature diagnostics	109

Chapter 1

Introduction



1.1 Introduction

Stars spend most of their lives on the main sequence (MS) burning hydrogen in the core, and over time evolve to the red giant branch (RGB) and asymptotic giant branch (AGB) to eventually become a white dwarf (WD). Stars approaching the end of the AGB phase are surrounded by a shell formed from ejected material as a result of mass loss and thermal pulses. Once mass loss ends, the core expands as it is no longer restricted by the dense shell of ejected material which has been carried away by a super wind. There now exists a distinct separation between the star and the ejected material, the core contracts and envelope expands with surface temperatures rising to $\sim 3 \times 10^4$ K. At this temperature the atoms in the ejected material become ionised causing the nebula to shine and become a planetary nebula (PN) (see [Figure 1.1](#)).

A binary star system consists of two stars that are gravitationally bound to each other. Different phenomenon will occur depending on their orbital separation, for example in binary systems with close orbital separations cataclysmic variables are observed. A cataclysmic variables occur when a WD accretes hydrogen-rich material from its companion, typically a giant or low-mass star, resulting in a thermonuclear runaway explosion that expels material $\sim 2 \times 10^{-4} M_{\odot}$ at velocities $\sim 1000 \text{ km s}^{-1}$ and is known as a nova or Type Ia supernova. The fate of more massive stars ($\gtrsim 8 M_{\odot}$) is in contrast to the more graceful progression to becoming a PN. In this scenario a high mass star will evolve into a supergiant by successively consuming its hydrogen, helium, carbon, nitrogen, oxygen and neon. Once all fuel is gone its central core collapses under its own gravity and explodes, ejecting a mass $\sim 10 M_{\odot}$, leaving a neutron star or black hole (depending on the initial mass of the star). Binary systems with wider orbital separation (hundreds of days) will result in symbiotic stars and symbiotic nebula.

Planetary nebulae (PNe) and novae are an extremely rich source of information; determining the chemical composition and structure of their surrounding nebula allow to understand the internal processes of the parent stars and chemical evolution of the Galaxy as their ejected material will mix with the interstellar

medium. Novae are unlike PNe, which shed their outer layers gracefully, and are instead characterised by bright eruptions that create and expel rare elements into the interstellar medium.

The aim of the research presented in this thesis is to develop a novel code and pipeline for generating photoionisation models of PNe and novae to enhance our understanding of their structure and composition. This was achieved through a new software package that amalgamated selected features of known codes in astronomy. These include a 3D morpho-kinematic modelling and reconstruction tool for astrophysical objects called SHAPE (Steffen & Koning, 2011), a large-scale spectral synthesis code designed to simulate physical conditions within an astronomical plasma and then predict the emitted spectrum called CLOUDY (Ferland *et al.*, 1998; van Hoof *et al.*, 2000; Ferland *et al.*, 2013, 2017), and PYCLOUDY, a Python library that handles CLOUDY. The result is PYCROSS, an acronym for “PYCLOUDY *Rendering of SHAPE Software*”.

In the following sections of this chapter an overview of the evolving WD is presented to highlight the effect and influence within PNe, symbiotic nebulae and the various classifications of novae. This chapter concludes with a breakdown of the remaining work within this thesis.

1.2 Planetary nebulae

The first observation of a PN took place in 1764 by French astronomer Charles Messier. Messier, an avid comet hunter, was compiling a catalogue of fixed, diffuse celestial objects to aid fellow comet hunters in their search for elusive transient objects, i.e. comets. The object was entered as the 27th object in the Messier catalogue² (M27 - Messier 27) which today is also known as the Dumbbell Nebula or NGC 6538 (Figure 1.2a). Approximately 20 years later, German-born British astronomer William Herschel designated this object as a ‘*Planetary Nebula*’³; due

¹ © 2008 Pearson Education, Inc., publishing as Pearson Addison-Wesley

²Detailed Messier catalogue: <http://astropixels.com/messier/messiercat.html>

³Nebula in Latin refers to cloud or fog

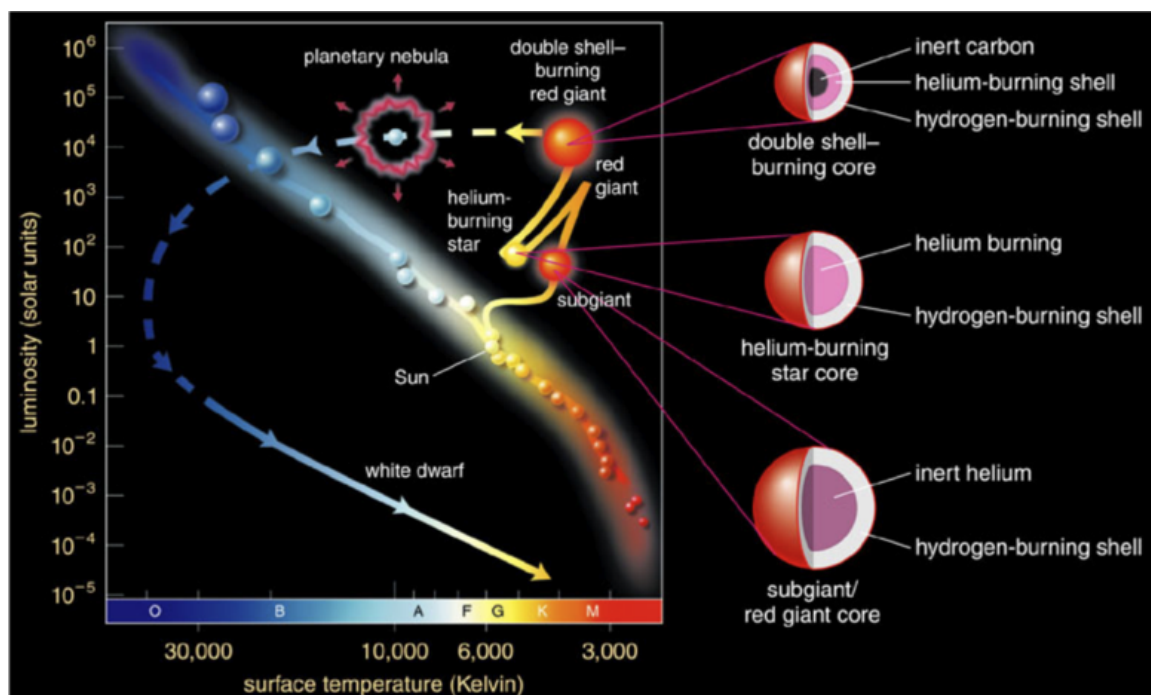


Figure 1.1: Stellar evolution of a star. HR diagram modified¹ to illustrate the path a star takes to become a PN

to its planet appearance resembling that of the planet Uranus, consisting of a disc like shape and hue as observed from his telescope.

Huggins and Miller [1864a; 1864b] acquired the first spectral data for NGC 6543 (Cats Eye Nebula, Figure 1.2b). Based on stars they believed to be observing, Huggins and Miller expected the data to reveal strong continuum and absorption features, instead the spectrum consisted of a single emission line. Further investigations disclosed that this line could be further resolved into three separate lines, the first and strongest being the Balmer line of hydrogen ($H\beta$), the second and third however, could not be identified as they were of unknown wavelengths. This discovery lead Huggins and Miller to believe that they had discovered a new element which they named ‘*neblium*’.

Progress was somewhat stifled until the early part of the 20th century at which point significant discoveries were made in a short time. Hubble (1922) discovered a correlation between the magnitude of the central star (CS) and the size of the PN and hypothesised that the emission-line spectrum of PN was a direct result of the nebula absorbing the continuous radiation from the central

star. [Bowen \(1928\)](#) inferred that the unknown emission lines (nebulium), was a direct result of transitions only possible in extremely low-density gas. These transitions dominate the spectra of PNe, (where densities are typically lower than 10^4 cm^{-3}) are not replicable on Earth and gave rise to the term ‘*forbidden lines*’. The following year [Perrine \(1929\)](#), investigating emission lines in PNe, observed that they were broad, in some instances split. Perrine correctly interpreted this to the nebula expanding.

Theoretical understanding of the true origins of PNe began when [Shklovsky \(1956a,b, 1957\)](#) proposed that the immediate predecessor of a PN was that of a rapidly evolving red giant (RG) star that had detached and ejected its atmosphere over several thousands of years to become a white dwarf (WD). The ejected envelope would then become ionised gas, from the intense radiation field of the central WD, and form a PN. This was determined by comparing the expansion velocities of PNe with the escape velocity of red giants. [Shklovsky \(1956a,b, 1957\)](#) also accredited the formation of PNe as the most powerful supplier of gas to the interstellar medium (ISM) with a mass of $\sim 0.7 M_{\odot}$ per year appearing in the galaxy due to this mechanism, several hundred times exceeding the amount ejected by all the novae (see [section 1.4](#)).

[Abell & Goldreich \(1966\)](#) reaffirmed [Shklovsky](#) theories by using the expansion velocities of PN and the escape velocities of RG stars to argue that PNe are the result of the ejected atmospheres of RG stars. Using [Shklovsky](#) estimate for the total number of galactic PNe, 6×10^4 , and a lifetime of 2×10^4 yr, [Abell & Goldreich \(1966\)](#) showed that PNe form at a rate of approximately 3 per year: the same order as the number of stars leaving the main sequence. They suggested that practically all low-mass stars will go through the PN stage, establishing the importance of understanding the evolution of PN in the scheme of stellar evolution. While [Shklovsky \(1956a,b, 1957\)](#) successfully drafted a scenario for PN evolution, the details of the transition from a sun-like star to PN remained unknown for another 30 years until the discovery of the thermal pulsing Asymptotic Giant Branch (AGB) star, their mass loss and interstellar winds. The following

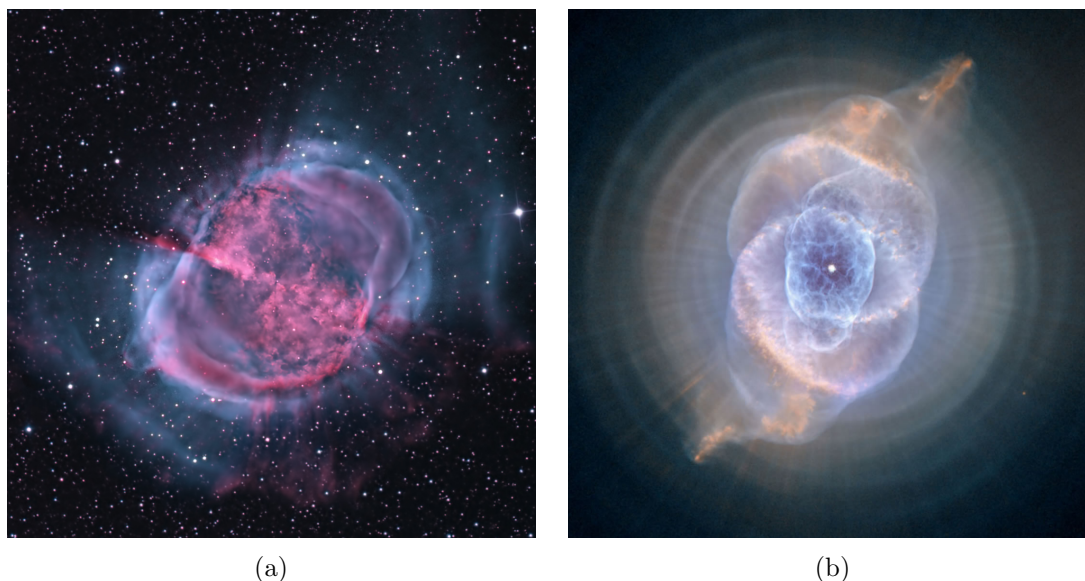


Figure 1.2: (a) M27 - The first discovered PN. This bi-colour image depicts colours emitted in hydrogen (blue-magenta-red) and oxygen (green). (© *Bill Snyder*). (b) In 1864 William Huggins acquired spectra for PN NGC 6543 - Cats Eye Nebula and discovered the spectrum was dominated by emission lines rather than continuum. 65 years later Charles Perrine correctly inferred that the nebula was expanding. (© *NASA*).

sections discuss how low to intermediate mass stars evolve to become PNe.

1.2.1 Evolution of planetary nebulae

There is no universal definition for PNe, however, their existence is dependent on two components: a circumstellar shell of certain mass and density and a hot central star to ionise it. An expanding shell and expansion velocities ($\sim 25 \text{ km s}^{-1}$) imply a dynamical lifetime of $\sim 10^4 \text{ yr}$ ([Kwok, 2000](#)). There exists “*mimics*” that are symbiotic systems, however, the PNe community tend to include these objects in their interests. This section will describe the evolutionary track and mechanics a star undergoes on its journey to become a PN. A more detailed description of each phase is presented in [Prialnik \(2009\)](#).

Main Sequence: Low to intermediate mass stars ($\sim 0.8 M_{\odot} - 8 M_{\odot}$) will over time evolve to become PNe, the evolutionary track for a sun-like star is illustrated in [Figure 1.1](#). As a star progresses along the MS its inner composition is changing, fusing hydrogen to helium. The fusion process will be the proton-proton chain

or CNO cycle for stars with masses $M_* \lesssim 2M_\odot$ and $M_* \gtrsim 2M_\odot$ respectively. As the helium core grows the hydrostatic equilibrium within the star is disrupted, once a critical mass is reached (Schönberg-Chandrasekhar limit) the helium core is unable to support the overlying layers against gravitational collapse. The star's core begins to contract and heat, core temperatures are further accelerated from hydrogen fusion occurring in the adjacent layer, causing the envelope to expand while decreasing its effective temperatures and the star ascends to the red giant branch (RGB).

Red Giant and Horizontal Branch: During this phase the star is still in a state of flux with a contracting core and expanding envelope. It is important to note that due to the star's larger radius the gravitational binding energy of the outer layers is diminished. As a result, stellar winds accelerate atoms in the photosphere beyond escape velocity resulting in mass loss, ensuring the remaining WD core will never reach the Chandrasekhar mass limit⁴. As the star's luminosity and opacity rise, a fully convective envelope forms and extends from outside the hydrogen burning shell to the surface. This convective envelope reaches layers where nuclear fusion byproducts reside, pulling the '*ashes*' to the surface, resulting in the first occurrence of a process known as '*dredge-up*'. The core contraction phase is slow, temperatures within the core and surrounding burning shell rise while the core material becomes degenerate. In low mass stars ($M_* \lesssim 2M_\odot$) when the core mass is $\sim 0.5M_\odot$, temperatures reach the helium burning threshold causing the helium to trigger a thermonuclear runaway event known as a '*helium flash*'. The tremendous rise in temperature removes the degeneracy of electrons allowing the core to expand. Stars with core masses $M_* \gtrsim 2M_\odot$ do not experience the helium flash as the core temperatures required for helium fusion are reached before electron degeneracy. During a star's transition along the horizontal branch (HB) it fuses helium in its core, producing carbon and subsequently oxygen in a manner similar to that of the MS. Once the helium reserves are drained the core

⁴The Chandrasekhar Limit of $1.4 M_\odot$ solar masses, is the theoretical maximum mass a white dwarf star can have without collapsing into a neutron star or black hole.

will once again contract and heat while its envelope will expand, cool and become redder. After the exhaustion of helium, these stars, consisting of a carbon-oxygen core, represent the beginning of the AGB, the last burning phase and immediate progenitor of a PN (Herwig, 2005).

Asymptotic Giant Branch: Paczyński (1971a,b) introduced a modern understanding of central star evolution of PNe by presenting post evolutionary tracks of AGB stars with hydrogen envelopes of cores of various masses. As central stars of PNe have luminosities of $\sim 10^4 L_{\odot}$, Paczyński (1971a,b) suggested that the only candidates suitable are that of double shell burning AGB stars (see Figure 1.3a), due to the similar luminosities as that of the central stars of PN. Paczyński (1971a,b) showed that the effective temperature of an AGB star will change very little as long as the star has an extensive hydrogen envelope, also an AGB star will not evolve to the blue side of the HR diagram (Figure 1.1) until the hydrogen envelope mass drops to a very small value. These evolutionary models were improved by Schönberner (1979, 1981, 1987) by introducing the effects of thermal pulses generated from the star (see Figure 1.3b). Schönberner’s models showed that hydrogen burning central stars evolve approximately three times faster than helium burning stars in the parts of the HR diagram where PNe are found.

Prialnik (2009) divides the AGB into two phases: (i) the early-AGB, where the hydrogen-burning shell extinguishes as a result of envelope expansion, and the luminosity is provided by helium shell burning; (ii) the thermal pulsing AGB (TP-AGB) which begins with reigniting hydrogen in a thin shell.

The lifetime of the early AGB phase is $\sim 10^7$ yr, depending on the core mass. Hydrogen-shell burning is the dominant source of energy for approximately 90% of the TP-AGB phase. The mass of the helium shell below the hydrogen burning shell increases, this leads to an increase in the triple- α reaction rate and eventually thermonuclear runaway known as a ‘*thermal pulse*’. This lasts until the helium shell over-expands and cools and the star returns to a steady state of hydrogen-

⁵Redrawn by Mary Geer Dethero as part of her undergraduate student internship.

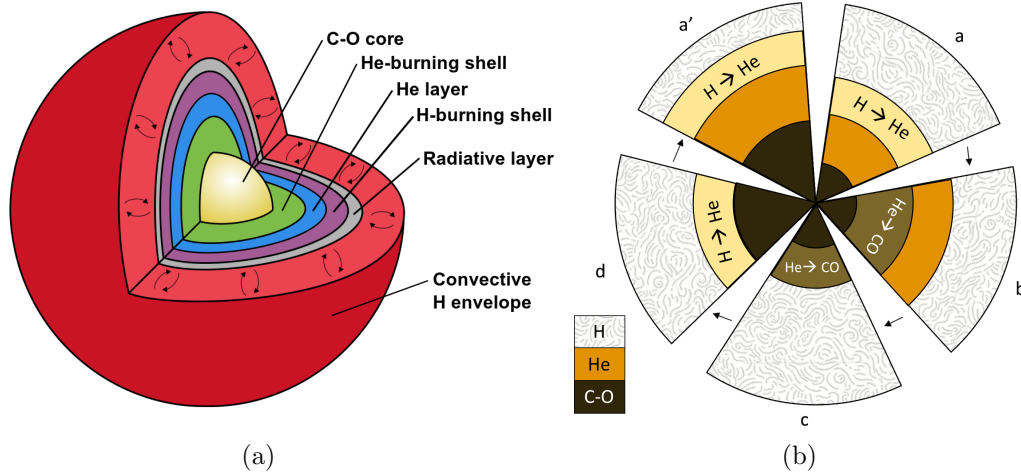


Figure 1.3: (a) The internal structure and layers of an AGB star (Persson, 2014). (b) Thermal pulse cycle of a AGB star (Priyalnik, 2009)⁵, Stages a and d consist of hydrogen shell burning, while stages b and c consist of helium shell burning. During stage c, the outer convective zone extends inwards beyond the helium burning shell’s boundary. This process dredges hydrogen and helium burning products to the surface which are mixed into the envelope. Stage a’ and a are similar except that the carbon-oxygen core has grown.

shell burning. During this AGB phase, the number of thermal pulses a star experiences will depend on its mass. Kwok (2000) outlines a number of interesting events during each thermal pulse: (i) at the helium flash, the temperature inside a flash driven convective shell is high enough for nitrogen to be converted into neon; (ii) after the flash, the base of the convective envelope dredges up heavy elements; (iii) for stars of higher mass, nuclear burning can occur at the bottom of the convective envelope where carbon is converted to nitrogen and the stellar luminosity can reach very high values.

Due to the double burning shell, long series of thermal pulses and strong stellar wind, stars suffer significant mass loss ranging from $10^{-9} M_{\odot}$ to $10^{-4} M_{\odot}$ per year. Once mass loss ceases the core expands as it is no longer burdened supporting the massive envelope. As the remaining envelope contracts a void is created between the star and the ejected material. Temperatures of the newly exposed CS or ‘planetary nebula nucleus’ (PNN) rise significantly ($\sim 30,000$ K) to ionise the atoms of the ejecta. Nuclear burning continues in the remaining shell of the carbon-oxygen core until its mass falls below $10^{-3} M_{\odot} - 10^{-4} M_{\odot}$ after which it can no longer maintain the high temperatures required for nuclear

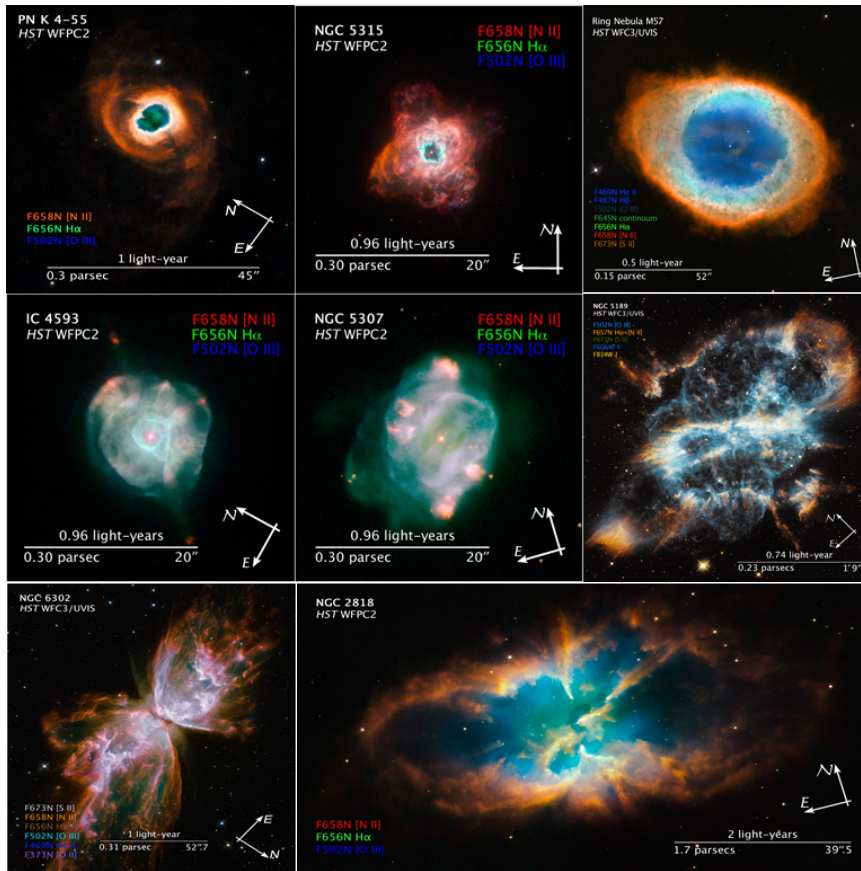


Figure 1.4: Collage of PN morphologies. © <http://hubblesite.org/images/>

burning. Gradually, the luminosity and ionising power of the PNN fades as the nebula continues to expand, eventually disappearing, the remaining central star continues its evolution to become a cool WD (Priyalnik, 2009).

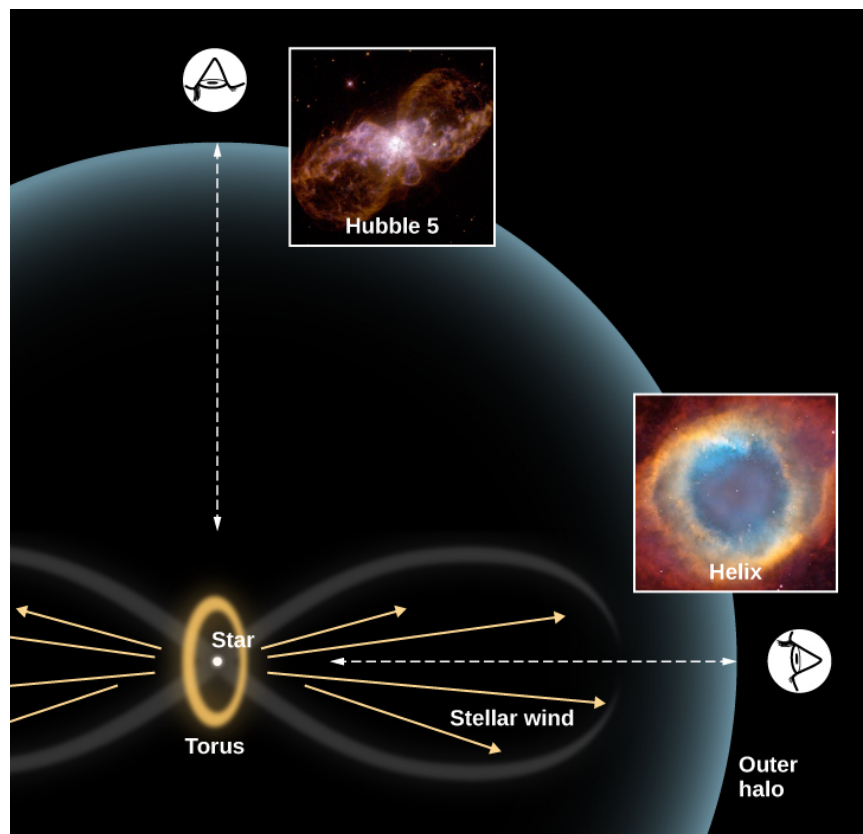


Figure 1.5: An example of a bipolar PN viewed from different angles. Viewing the nebula face on will result in a elongated bipolar nebula similar to Hubble 5. The heat generated by the fast winds causes each lobe to expand. Viewing along the poles results in a more circular nebula with a central cavity similar to the Helix nebula. The torus may be as a result of a close binary or symbiotic star at the centre of the nebula. Credit “Hubble 5”: modification of work by Bruce Balick (University of Washington), Vincent Icke (Leiden University, The Netherlands), Garrelt Mellema (Stockholm University), and NASA/ESA; credit “Helix”: modification of work by NASA, ESA, C.R. O’Dell (Vanderbilt University), and M. Meixner, P. McCullough. © <https://pressbooks.online.ucf.edu/astronomybc/chapter/22-4-further-evolution-of-stars/>

1.2.2 Morphology & structure

PNe have an extremely diverse range of morphologies, examples of which can be seen in [Figure 1.4](#). This variance in morphology may be due to the angle from which they are being viewed, meaning that the majority of PNe have a similar geometric shape; a hot central star surrounded by a thick torus of gas with winds escaping from the poles, see [Figure 1.5](#). While this figure gives examples where PNe are being viewed from the front and along the poles, it is important to note that PNe are often viewed at intermediate angles, resulting in more elaborate

and complex structures.

There are many known inherited and evolutionary factors that influence the morphologies of PNe: initial mass, physical conditions of the interstellar or circumstellar medium surrounding the post AGB star, stellar wind that produces the shell, fast winds from the central star and the possible presence of a companion star. One of the greatest challenges in PN research is understanding the origin and evolution of these varying morphologies (Kwok, 2000). This section will discuss morphology classification, structural components and possible shaping mechanisms.

Curtis (1918) pioneered the first large scale study of morphologies of 78 PNe over a three-year period, classifying them, based on their appearance into one of six classes. Since then, subsequent classification schemes have been proposed based on better understanding achieved with the onset of digital detectors and higher angular resolution. A common classification scheme employed by astronomers is that proposed by Stanghellini *et al.* (1993) who studied 111 galactic PN to determine if there was a correlation between their morphology and the evolution of the central star, classifications include: (i) stellar, (ii) elliptical, (iii) bipolar, (iv) symmetric, and (v) irregular.

A more recent and extremely detailed classification scheme was presented by Sahai *et al.* (2011) (Table 1.1) who extended that of Stanghellini *et al.* (1993) by reviewing over 119 images taken from surveys carried out with HST/WFPC2. This comprehensive morphological classification system⁶ focuses on young PNe as they best show the influences or symmetries imposed on them by the dominant physical processes operating at the first and primary stage of the shaping process.

Macro & Micro Structures: Observing and interpreting stellar objects beyond our solar system is difficult as 3D volumetric objects are observed as 2D projections. Detecting and distinguishing detailed macro- and micro-structures within PNe has improved significantly with higher resolution detectors.

⁶A continuation of their work (Sahai *et al.*, 2007), commonly referred to as SMSC07. In this table the italicised text for primary classes and secondary characteristics are new additions to the older morphological classification system SMSC07.

Table 1.1: PNe Morphological Classification Codes (Sahai *et al.*, 2011)

PRIMARY CLASSIFICATION: Nebular Shape	
B	Bipolar
M	Multipolar
E	Elongated
I	Irregular
<i>R</i>	<i>Round</i>
<i>L</i>	<i>Collimated Lobe Pair</i>
<i>S</i>	<i>Spiral Arm</i>
SECONDARY CLASSIFICATION	
Lobes	
o	Lobes open at ends
c	Lobes closed at ends
Central Regions	
w	Central region is (relatively) dark and shows an obscuring waist
<i>t</i>	<i>Central region is bright and has a toroidal structure</i>
<i>bct</i>	<i>Central region is bright and barrel shaped</i>
<i>bcr(c)</i>	<i>Barrel has closed ends</i>
<i>bcr(o)</i>	<i>Barrel has open ends</i>
<i>bcr(i)</i>	<i>Irregular structure present in barrel interior</i>
Central Star	
*	Central star evident in optical images
*(nnn)	Star is offset from the centre of symmetry and one or more nebular structures, nnn is maximum offset in miliarcsec
Other Nebular Characteristics	
an	Ansaes
ml	Minor lobes
sk	A skirt-like structure around the primary lobes
<i>ib</i>	<i>An inner bubble structure inside the primary nebular structure</i>
<i>wv</i>	<i>A patterned structure, such as a weave or a mottling</i>
<i>rg</i>	<i>Rings projected on lobes</i>
<i>rr</i>	<i>Radial rays</i>
<i>pr</i>	<i>One or more pairs of diametrically opposed protrusions on the primary geometrical shape</i>
<i>ir</i>	<i>Additional unclassified nebular structure lacking symmetry, not covered by primary or secondary classifications</i>
Point Symmetry	
ps(m)	Due to the presence of two or more pairs of diametrically opposed lobes
ps(am)	Due to diametrically opposed ansae
ps(s)	Overall geometric shape of lobes is point-symmetric
<i>ps(t)</i>	<i>Waist has point symmetry structure</i>
<i>ps(bcr)</i>	<i>Barrell-shaped central region has point-symmetric structure</i>
<i>ps(ib)</i>	<i>Inner bubble has point-symmetric structure</i>
Halo	
h	Halo is present
h(e)	Halo has elongated shape
h(i)	Halo has indeterminate shape
h(a)	Halo has centro-symmetric arc-like features
h(sb)	Halo shows searchlight beams
<i>h(d)</i>	<i>Halo has a sharp outer edge, or shows a discontinuity in its interior</i>

Macro-structures (halos, shells and rims) have been known for some time (Duncan, 1937). Morphological studies of halos by Chu *et al.* (1987) led them to suggest they be classified into two types: Type I halos having faint and filamentary material detached from the primary shell, and Type II halos showing bright and amorphous structures attached to the main shell. The diameters of Type I halos range from $\sim 0.5 \text{ pc} \gtrsim 1 \text{ pc}$ and are often nearly static, Type II halos are expanding at velocities similar to those of the primary shell, furthermore, some elliptical PNe are found to have spherical halos, suggesting morphology develops after the AGB phase.

Micro-structures are small structures, such as jets, knots and filaments, located near the outer edges of the rims of PNe and are formed as a result of instabilities. Knots contain a large fraction of the entire ejecta of the star, by which the material is trapped in shielded molecular zones. Cometary knots are dark objects with luminous tails pointing away from the central star and contain a higher concentration of matter. It has been suggested that fast winds from the central star pass through these dense regions, which are slowly being evaporated, causing the evaporated gas to be swept backwards. (O'Dell & Handron, 1996; O'Dell *et al.*, 2002).

Spectroscopic analysis by Balick *et al.* (1994) of NGC 6543, NGC 6826 and NGC 7009 showed that knots ($\sim 0.01 \text{ pc}$) observed in [N II] and [O I] lines, are in low ionisation states, have high supersonic velocities ($\sim 50 \text{ km s}^{-1}$) and a shorter kinematic age than the gas surrounding them. Balick *et al.* (1994) named these as '*fast low-ionisation emission regions*' (FLIER), also known as ansae. Gonçalves *et al.* (2001) compiled a list of 50 PNe where these microstructures were observed in [N II], [S II], [O II] and [O I] lines (forbidden lines) and described them as '*low ionisation structures*' (LIS). Gonçalves *et al.* concluded that LIS are present indistinctly in all morphological classes of PNe, indicating that their formation is not necessarily connected with the processes responsible for the asphericity of the main morphological components of PNe. FLIERs are a special subclass of LIS in which symmetric pairs of low ionisation knots exhibit opposite, supersonic

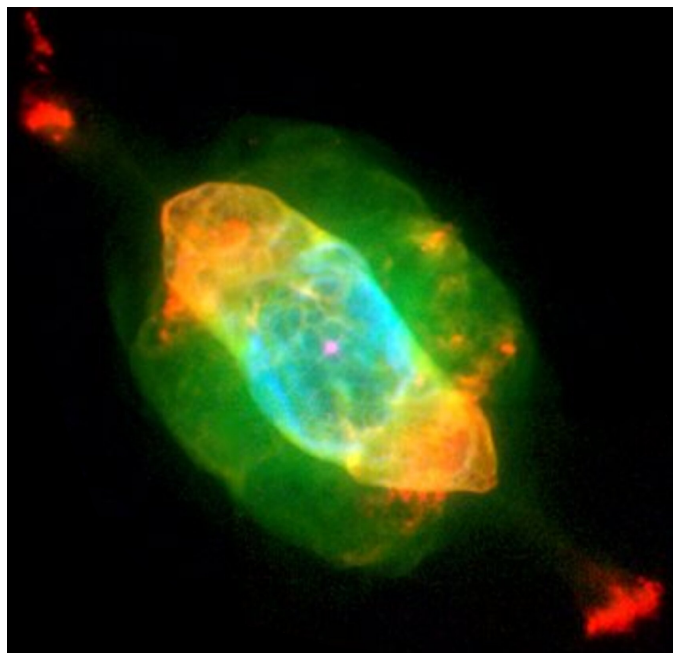


Figure 1.6: HST WFPC2 image of NGC 7009 (The Saturn Nebula) showing prominent FLIERS and jets along the major axis. © NASA

Doppler shifts.

High resolution imaging may detect shapes, however, better understanding of the three dimensional structure is achieved when this data is coupled with spatially resolved spectra to determine the kinematics of the gas within the nebula. Phillips *et al.* (2010) used narrow-band imaging from HST, mid-IR imaging from Spitzer, space-based mid-IR spectra (from ISO and Spitzer), and ground-based IR and optical, long-slit spectra at a variety of positions on NGC 7009 (see Figure 1.6). This combination of data allowed for the creation of extinction maps; identify shock fronts, FLIERS and other features to generate a more complete picture of the nebula.

(Shaw, 2012) demonstrated the importance of obtaining the most favourable observational conditions possible and also highlighted the utility of combining multiple, narrow-band images to reveal ionisation stratification and the detection of jets emanating from the vicinity of the CS of NGC 6543. As can be seen in Figure 1.7, the centre image clearly shows the effects of AGB wind and how it interacts with the ISM. The HST image on the bottom left of Figure 1.7, shows the remnant features of gas ejection on the AGB in the form of concentric rings.

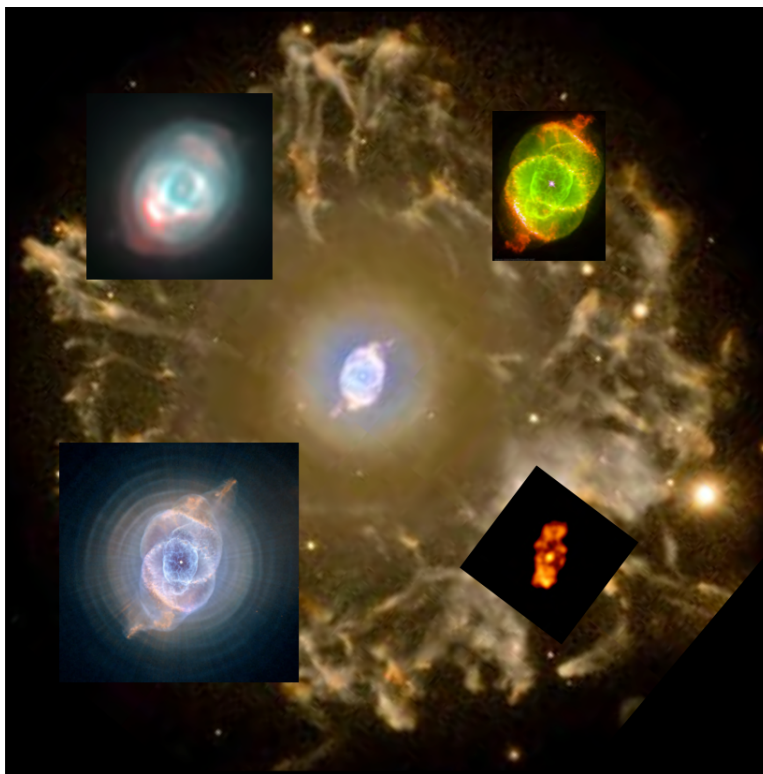


Figure 1.7: Image taken from [Shaw \(2012\)](#) demonstrating the advantages of deep, multi-band image of NGC 6543 (credit: R. Corradi/IAC) showing a large halo (centre). Superimposed are four multi-band images of the nebular core: an amateur ground-based image (upper left), a multi-band image from HST (upper right; credit: J.P. Harrington and K.J. Borkowski, and NASA), a deep HST exposure with compressed dynamic range (lower left; credit: NASA, ESA, HEIC) and an X-ray image from CXC (lower right; credit: Chu et al. and NASA).

In this example, the image on the top left is taken from a ground based telescope, is of no comparison to that of the multi-band image from HST, top right. With an improved angular resolution of a factor of 10, this image revealed ionisation stratification and the detection of jets emanating from the vicinity of the central star. Finally, the image on the lower right (X-ray) helped understand the role of pressure from hot gas and the dynamics of this PN.

1.2.3 Chemical composition

Thus far, the evolution of PNe from MS star to WD has been outlined and the varying morphologies, classification schemes and shaping mechanisms have been described. In all aspects it is critical to establish the physical evolution of the parent star, or stars in the case of a binary. Understanding the chemical

Table 1.2: Nebular and auroral T_e & N_e diagnostic line ratios (Tsamis *et al.*, 2003)

Electron Temperature (T_e)	
[O III]	$(4959 \text{ \AA} + 5007 \text{ \AA}) / (4363 \text{ \AA})$
[N II]	$(6548 \text{ \AA} + 6584 \text{ \AA}) / (5754 \text{ \AA})$
[O II]	$(3727 \text{ \AA}) / (7320 \text{ \AA} + 7330 \text{ \AA})$
[S II]	$(4068 \text{ \AA}) / (6731 \text{ \AA} + 6716 \text{ \AA})$
Electron Density (N_e)	
[Ar IV]	$(4740 \text{ \AA}) / (4711 \text{ \AA})$
[Cl III]	$(5517 \text{ \AA}) / (5538 \text{ \AA})$
[S II]	$(6731 \text{ \AA}) / (6716 \text{ \AA})$

composition of PNe is equally important as the ejected material mixes with the ISM, giving rise to chemical enrichment processes.

PNe spectra consist predominately of emission lines, a result of ionisation from UV radiation emitted from the central WD and interaction of electrons within the nebula. These lines are categorised as either recombination lines: formed when an ion and an electron combine, leading to a cascade of the electron down to the ground state, or collisionally excited lines: formed when electrons collide with atoms or ions within the gas, and excite them. When these excited atoms or ions revert to their ground state, they will emit a photon, and are known as ‘*forbidden lines*’ (see [section 1.2: Planetary nebulae](#)), and denoted by square brackets, (e.g [N II], [O III] etc.).

Emissions lines can be further categorised as being nebular or auroral, and are identified by their transitions from higher to lower excitation states. Examples of nebular and auroral lines include doubly ionised oxygen lines [O III] at 4959 Å and 5007 Å (nebular) and [O III] 4363 Å (auroral) whose ratio is used to determine electron temperatures (T_e) in nebular plasmas (see [subsection 3.2.1, Figure 3.2](#)). Examples of other nebular and auroral line ratios used to determine electron densities (N_e) and T_e are listed in [Table 1.2](#).

Abundances of elements within a nebula are expressed as a ratio to hydrogen, spectroscopic analysis can determine chemical composition, density, velocities and temperatures of regions within a nebula, showing lines from many elements

from which abundances can be derived. Peimbert (1978) classified PNe based on their chemical abundances (H, He, C, N, NE and O) into the following four types: Type I: PNe rich in He and N, resulting from higher mass progenitors $\gtrsim 2.5M_{\odot}$, Type II: PNe evolving from lower mass stars than that of Type I. PNe like these have lower abundances, Type III: High velocity PNe ($\Delta v > 60 \text{ kms}^{-1}$) that are iron-poor and Type IV: PNe that have a slight deficiency of helium relative to other PNe.

An important and current problem in abundance determinations in PNe and H II regions (regions of ionised gas surrounding a young massive star) is the existence of a discrepancy between the abundances determined with forbidden lines and those determined by recombination lines. The ratio of these derivations is defined by the abundance discrepancy factor (ADF). Gaseous nebula have an ADF in the range of 2 – 3, in PNe this can be as high as 70 (Torres-Peimbert, 2015). It has been argued that the ADF in PNe is due to: (i) chemical inhomogeneities (fluctuations or variations), (ii) temperature inhomogeneities in chemically homogeneous objects and (iii) the destruction of solid bodies inside PNe that produce cool and high-metallicity pockets (see Peimbert *et al.*, 2017, and authors therein). Corradi *et al.* (2015) investigated the abundance discrepancy problem in three PNe (Abell 46, Abell 63 and Ou5) with close binary central stars (orbital periods of ~ 10 hrs) and common envelope evolution and showed all to have a large ADF. Corradi *et al.* does not solely credit the high ADF to close binaries and debates that the origins of the metal rich gas present in the nebula may also be influenced by nova-like outbursts, planetary material and the destruction and engulfment of circumbinary Jovian planets. The elemental enrichment/depletion expected for planets destroyed during the evolution of a PN is still uncertain, thus, further investigation is necessary to determine the planet shaping hypothesis. A deep spectroscopic study of the microstructures (knots, jets, etc.) and main nebula is required in order to compare their compositions and determine the ADF.

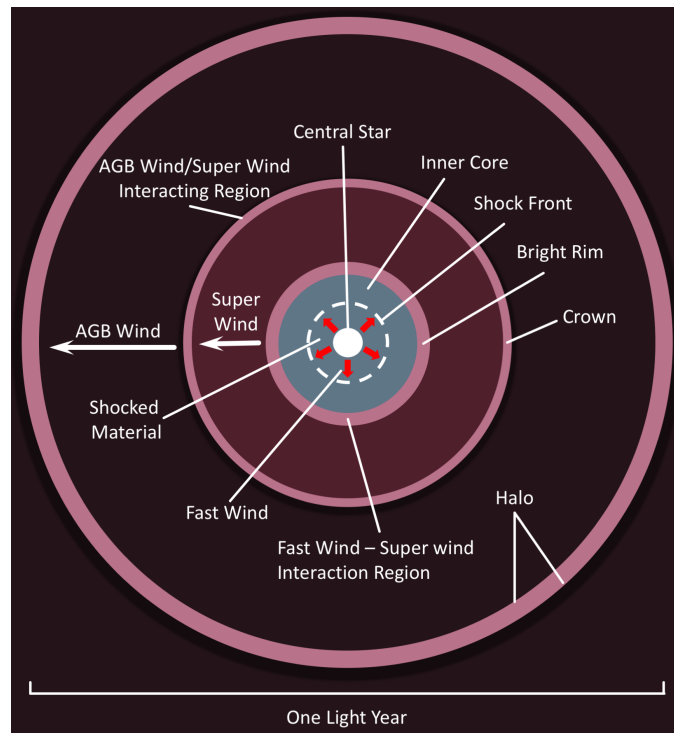


Figure 1.8: The fast winds of the central star distribute gas to different regions. As fast winds collide with denser and slower super wind, a bright rim is formed. Further out, super winds interact with material shed earlier in the star’s evolution which forms the crown. The wind created during the AGB phase has travelled further away from the central star, may compress outlying interstellar matter resulting in a brightened halo. Image adapted and recreated from (Soker, 1992)

1.2.4 Shaping mechanisms

As previously stated, one of the greatest challenges in PN research is understanding the origin, morphologies and mechanisms that shape them. Regarding shaping mechanisms, PNe can be categorised as being spherical ($\sim 20\%$ (Parker *et al.*, 2006b)) or aspherical (bipolar or elliptical). One of the first models to investigate the shaping of PNe was presented by Kwok *et al.* (1978). The ‘*interstellar wind model*’ (ISW) proposed that a slow, dense, super wind originating from an AGB central star is later swept up by a faster tenuous wind emanating from the emerging WD. A compressed, dense thin shell is formed where it is then ionised; both winds are said to act hydrodynamically, see Figure 1.8. While this model explains the shell structure, expansion velocity and density of PNe formation, it cannot account for the variety of morphologies and microstructures as discussed in previous sections.

Table 1.3: Binary System Classification for PNe (Soker, 1997)

Class	Likely Outcome
Extremely Wide Binaries* $T_{\text{orb}} \gg T_{\text{PNF}} \sim 10^5$ yrs, $a \gtrsim 5000$ au	Progenitors of PN that did not interact with any companion. Possible formation of small bubble inside the nebula.
Wide Binaries $T_{\text{orb}} \sim T_{\text{PNF}}$	Displacement of the central star Asymmetrical nebulae Jets bent in the same direction
Close Binaries (Avoiding a common envelope)	Bipolar PN (from a disc around the companion). Expansion velocity: faster for a WD than for a main-sequence companion)
Common Envelope (Substellar Companions)	Elliptical PNe; halo likely to be elliptical as well.

* T_{orb} : Orbital Period, T_{PNF} : Total formation and life time of the PN $\sim 10^5$ yrs, for orbital separations of $\gtrsim 5000$ au

The varied and striking morphologies displayed by PNe cannot be explained by single star scenarios, to this end researchers have focused on stellar rotation, magnetic fields and stellar/substellar companions as possible scenarios to explain the aspherical morphologies found in PNe. Rapid rotation can lead to equatorial mass-loss and the formation of highly axisymmetric structures like rings and polar caps. However, it has been demonstrated that rapid rotation cannot reproduce bipolar axisymmetric structure as the rotation rates required are impossibly high for single stars. Strong magnetic fields may constrain overflows along the axis and around the equator forming jet and torus-like features respectively. In isolated PNe progenitors it has been shown that magnetic fields are not strong or long-lived enough to produce anything but weak deviations from spherical symmetry. The binary or substellar companion hypothesis has existed since the early 1970's and have become the preferred scenario for formation of aspherical PNe. AGB stars in a close binary system interact with their companion, overflowing its Roche lobe⁷ (see Jones & Boffin, 2017, and authors therein).

Soker (1996) argued that when a star is in the RGB or AGB phase, interaction with a substellar or stellar companion results in the spinning up of the stellar envelope, causing a wind to blow axisymmetrically, rather than spherically. Soker describes the interaction of substellar objects as engulfing any Jupiter-like planet residing closer than ~ 4 au. Later, Soker (1997) made an assumption, based entirely on observations, that non-spherical PNe cannot be formed by single star

⁷The Roche lobe (or Roche limit) is the region around a star in a binary system within which orbiting material is gravitationally bound to that star.

Table 1.4: Summarisation of PNe population synthesis models (Boyle, 2018)

N_{PN}	Planet-Fraction	Binary-Fraction	Single-Fraction
16,400	1.5%(240 PNe)	20%(3,300 PNe)	78.5% (12,900 PNe)

evolution and proposed that shaping of PNe was as a result of interactions between (i) stellar rotation, (ii) magnetic fields and (iii) binary stars during the AGB or post-AGB phase. An adaption of Soker (1997) classification scheme for binary progenitors of PNe, based on varying degrees of separation and possible likely shaping outcomes is documented in Table 1.3.

Recently, Boyle (2018) developed a population synthesis model consisting of $16,400 \pm 2,300$ visible PNe in the present-day galactic population to calculate the fraction of PN progenitors shaped by engulfed planets. The results of this study are summarised in Table 1.4 where N_{PN} is the number of PNe used in a specific model, planet-fraction is the number of PNe evolving from the engulfment of massive planets on the AGB, binary-fraction is the number of PNe evolving from binary interactions and single-fraction is the number of PNe evolving from single stars without planet engulfment on the AGB. In total, 48 population synthesis models were calculated with the planet-fraction for the present-day galaxy varying between 1%–2%. This result is relatively low as $\simeq 80\%$ ⁸ of the observed population of PNe are non-spherical, however Boyle (2018) states that if low-mass single stars are unable to form a visible PNe than the expected planet-fraction PNe in the present-day galaxy would be $\simeq 7\%$.

Nordhaus & Blackman (2006) studied the effect of low-mass ($< 0.3 M_{\odot}$) companions embedded in the envelope of a $\sim 3M_{\odot}$ star during three epochs of its evolution (RGB, AGB and thermal-pulsing AGB); companions included planets, brown dwarfs and low-mass MS stars. Findings from this study revealed that during the RGB phase envelope ejection was unlikely. Scenarios did exist during the AGB phase whereby massive brown dwarfs ejected the envelope equatorially, lower mass companions may spiral inwards far enough to induce a differential ro-

⁸See (Parker *et al.*, 2006a) for details of morphological classifications for all 903 new MASH PNe

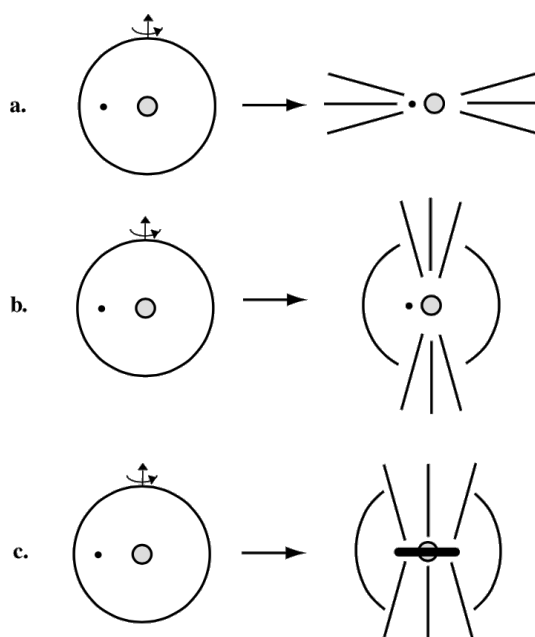


Figure 1.9: Binaries & common envelope evolution models (Nordhaus & Blackman, 2006). (a) the companion provides orbital energy unbinding the envelope (or portion of it) equatorially, (b) the companion spirals inwards inducing differential rotation unbinding the envelope or (c) the companion is shredded into a disc around the core, leading to disc driven overflow.

tation ejecting material along polar regions while also forming ansae, furthermore such companions may be shredded into a disc resulting in a disc-driven overflow. AGB stars in the thermal pulsing phase where envelopes have significantly expanded, showed an equatorial torus-like appearance. The amount of material contained within the outflow is determined by the mass and penetration depth of the companion. Figure 1.9 illustrated the schematic for the three scenarios presented by Nordhaus & Blackman.

The first PNe confirmed CS binary was Abell 63, discovered by Bond (1976). Miszalski *et al.* (2009a,b) discovered ~ 20 new binary systems based on data collected from the Optical Gravitational Lensing Experiment (OGLE) survey. These results revealed that PNe with detectable close binary stars tend to show bipolar morphologies with equatorial rings and extended jet-like features, as well as low-ionisation filamentary structures. PNe and binary stellar evolution are inextricably linked; the evolution and mass loss of low to intermediate mass stars can be accounted for in PNe evolution while binary evolution, and in particular close-binary evolution, impacts the mass loss rate, energetics and morphologies.

Close binaries may have a dramatic effect regarding mass loss through a common envelope episode (Boffin & Jones, 2019). Known PNe hosting binary central stars include: Abell 65, NGC 5187, NGC 6326, NGC 1514, The Necklace and MyCn 18, to name a few. Images depicting the varying array of PNe morphologies hosting binary CS can be seen in Jones & Boffin (2017).

There is strong evidence to suggest that binary interactions, in the form of gravitational energy from mass transfer and the spiralling-in process releasing gravitational orbital energy, shape non-spherical PNe. However, the period distribution of binary progenitor systems suggest that binary shaping does not account for the total population of non-spherical PNe, and that a small population must be as a direct result of planet engulfment by the AGB progenitors. This hypothesis is becoming more popular due to the discovery of hundreds of massive planets around PN progenitor stars, furthermore the origin of metal-rich components embedded within the nebula may also originate from the remnants of an exploded planet (see Akashi & Soker, 2017; Akashi *et al.*, 2018, and authors therein).

1.3 Symbiotic Stars

Understanding PNe can account for the evolutionary path and mass loss history of low to intermediate mass stars while binary evolution, can further our understanding of mass-loss rate, energetics and morphology. Boffin & Jones (2019) lists 50 known post-common-envelope PNe containing binary central stars with orbital periods ranging from 0.14 to 18.15 days, with another possible 14 candidates derived from simulations. Ongoing research regarding binary central stars as shaping mechanisms in PNe, symbiotic nebulae and novae is further helped with advances in technology, both hardware for detection and software for simulations. This section will describe other binary star systems i.e. symbiotic nebulae and novae.

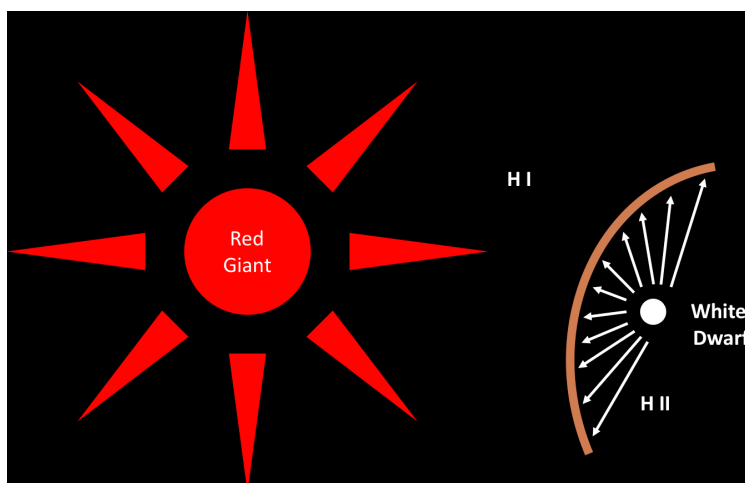


Figure 1.10: Schematic, of a SyNe: a hot white dwarf and cooler RG that is losing material in a wind. In this schematic a partially ionised nebula is represented with the bow-shaped curve showing the boundary between the portion of the nebula where hydrogen is ionised by radiation from the WD (H II), and the region nearer the RG that is primarily neutral hydrogen (H I). Boundary shapes will vary based on the systems. See [Figure 1.11](#) for example of known SyNe Hen2-104 “*The Southern Crab*”.

Symbiotic stars (SySts, SySt singular) are a wide binary system consisting of a mass accretor, typically a WD, but in some cases a neutron star is observed, the donor is a RG or Mira star with orbital periods in the order of years ([Ilkiewicz, K. & Mikolajewska, J., 2017](#)). In some instances these systems have resolved nebulae consisting of ringlike or bipolar shapes and are referred to as symbiotic nebula (SyNe). This type of system may resemble cataclysmic variables but are less understood with less violent eruptions. SyNe are distinguishable from PNe in that the nebula material originates from the cooler donor star which is then ionised by the hot WD, in comparison to a bona fide PNe whose material originates from the star during the AGB phase and is then ionised by the star when it becomes a WD (see [De Marco, 2009](#), and references therein). It is important to note therefore, that if the RG has not influenced or affected the evolution of the WD, then the object remains a genuine PN. Relying on observations alone is insufficient to determine and classify SySts, where PNe typically evolve by H or He burning shells after most of the H atmosphere is lost during the AGB, SySt evolve by gravitational or nuclear burning as a result of mass transfer and accretion ([Kwok, 2003](#)).

Identifying SyNe is often difficult as their spectra are often confused with PNe and dense H II regions. SySts optical spectra can contain absorption features from the cool companion star as well as high ionisation lines (He II), low to intermediate ionisation lines ([N II]), and bright Balmer lines ($H\alpha$, $H\beta$) due to the presence of a luminous hot WD (Akraś *et al.*, 2019a), see Figure 1.10. This problem is further compounded such that emission lines used to distinguish them from other objects are not present (Ilkiewicz, K. & Mikolajewska, J., 2017). An example of such a misidentification was reported by Munari *et al.* (2013), who at the time believed that they discovered a PN centred on the SySt DT Ser, a poorly studied variable reported by the General Catalog of Variable Stars. Frew *et al.* (2014) later presented an alternative interpretation of DT Ser by analysing the data acquired by Munari *et al.* in addition to multi wavelength and photometry data from 14 various virtual observatory databases. Frew *et al.* instead concluded that there was no association between DT Ser and the PN, but rather that DT Ser was not a SySr and was instead superposed on the newly discovered but unrelated background PN.

Belczyński *et al.* (2000) presented a catalogue of 188 confirmed SySts (17 of which were classified as extragalactic). and another 30 objects suspected of being symbiotic (2 of which were classified as extragalactic). This catalogue consisted of coordinates, V and K magnitudes, UV, IR, X-ray and radio observations. Since this, the number of confirmed SySts has doubled with many more potential candidates emerging (Merc *et al.*, 2019). This may be due to advances in hardware but also in software with many astronomers in recent years adding machine learning to their arsenal (Akraś *et al.*, 2019a,b).

Akraś *et al.* (2019a) presented the most recent census of SySts using data acquired from 2MASS, WISE, and Gaia surveys. Results generated an updated list containing 323 known and 87 candidate SySts, 257 of which are galactic and 66 extragalactic. This study focused mainly on spectral energy distributions profiles, temperatures and IR types of SySts obtained through various modelling and machine learning techniques. Akraś *et al.* (2019b) developed a new approach

for identifying SySts from other $H\alpha$ emitters in photometric surveys using numerous machine learning algorithms such as cascading classification trees, linear discriminate analysis, and K-nearest neighbour. Applying their newly developed classification tree identified 72 new candidate sources of SySts successfully passed the criteria from data acquired by [Akraš et al. \(2019a\)](#). A new online catalogue⁹ of all known symbiotic systems and candidates, categorised according to their location in 14 galaxies has been made available by [Merc et al. \(2019\)](#). This dataset contains information relating to the position, brightness in various special regions and any observational properties such as the presence of outbursts, flickering, symbiotic type, emissions, etc. An advantage of studying SySts in other galaxies is that their distances are generally well resolved as they correspond to the distances of their parent galaxy.

A popular and well known example of a SyNe is Hen 2–104, also known as “*The Southern Crab*”. Located in the southern constellation of Centaurus (14h 11m 52.06s right ascension, $-51^{\circ} 26' 24.1''$ declination) at a distance of 3.3 ± 0.9 kps ([Santander-García et al., 2008](#)). This SyNe was originally being classified as a PN until [Whitelock \(1987\)](#) discovered its symbiotic nature with the presence of a long period (400 day) Mira and WD pair by means of near-IT photometric monitoring. Material ejected from the Mira is captured by the gravity of its companion, the WD erupts when enough material is pulled onto its surface creating bipolar structure (see [Figure 1.11](#)). As this SyNe spans a number of light years, its nebulosity on the extremity is extremely thin, and as such the full extent and shape of the outer hourglass is not resolved, its three ionised structures; an inner hourglass, open-ended outer hourglass and a pair of axisymmetric polar jets are clearly visible. Both stars are embedded inside the the more recently ejected inner hourglass which is enlarged and shown at the bottom right of [Figure 1.11](#).

[Santander-García et al. \(2008\)](#) researched Hen 2–104 to determine its kinematics, morphology, expansion distance, density distribution and ionised mass and

⁹New Online Database of Symbiotic Variables – Updated regularly and available via the following web-portal: <http://astronomy.science.upjs.sk/symbiotics/>

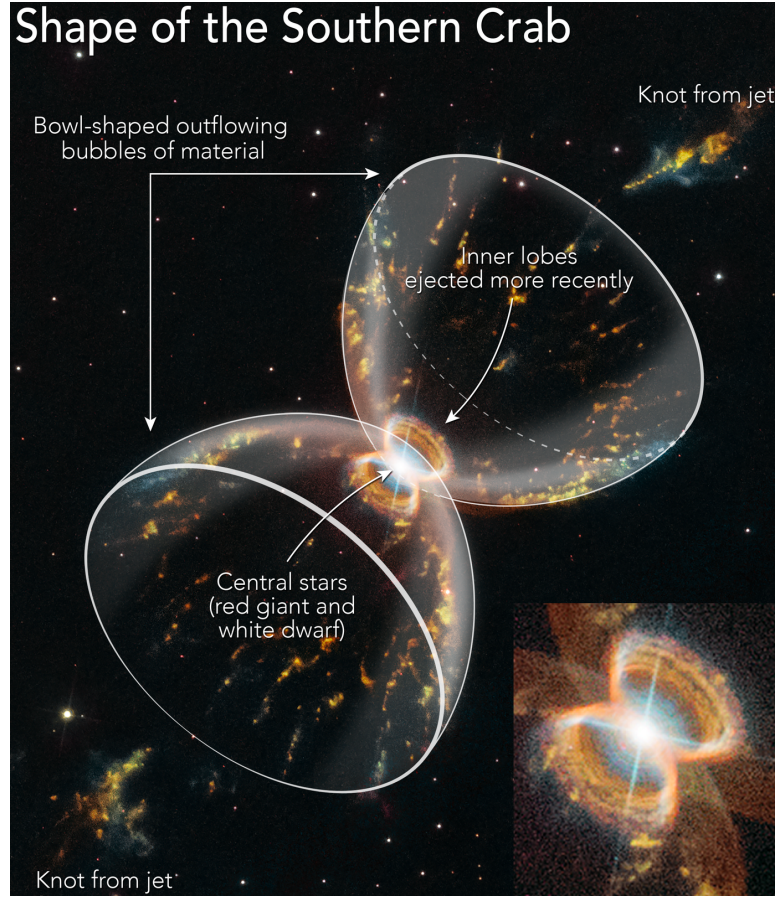


Figure 1.11: SyNe Hen2–104, also known as *The Southern Crab* is a SyNe located in the constellation Centaurus. This SyNe has two distinct nested hourglass shaped structures, a result of the interactions between the RG and WD at its centre. The more recent inner hourglass is enlarged and shown at the bottom right corner of the image. © Credits: NASA, ESA, and A. Feild (STScI)

determined a $T_e = 10000\text{K}$ for the inner hourglass and base of the outer hourglass, with densities ranging from $n_e = 500\text{ cm}^{-3} - 1000\text{ cm}^{-3}$ and $n_e \sim 300\text{ cm}^{-3} - 500\text{ cm}^{-3}$ respectively. The ionisation mass of the extended nebula was determined to be approximately $\frac{1}{10} M_\odot$ and attributes this to the Mira being the main mass contributor with the WD shaping the nebula. Their spatio-kinematic model showed that overflow speeds were slowest at low latitudes and highest along the polar direction. [Santander-García *et al.*](#) concludes by stating that the distinctive characteristics of SyNe being one or two orders of magnitude less massive than PNe do not apply to Hen 2–104 and it showed the characteristics its symbiotic nature, consisting of a high density core, NIR colours unusual for a PN, and an articulated high-excitation spectrum indicating the presence of a cool giant.

(Clyne *et al.*, 2015) also carried out a detailed investigation into the physical properties, structure and dynamics of Hen 2-104 using archival data was obtained from Corradi *et al.* (2001). Results indicated a kinematic age of the outer hourglass to be approximately 2.4 times older than the inner hourglass, and is consistent with the ratio of width between the structures. A 3D SHAPE model of the SyNe showed discontinuity in the opening angle of the lobes of roughly 10° indicating a change in thermal and velocity structure in the outer hourglass which may be due to a unstable shock transition between regions.

SySt offer excellent opportunities to research binary interaction and stellar evolution as they show instances of jets, accretion/excretion discs, nova outbursts, ionised nebulae and interacting winds, they are also promising candidates for progenitors of type Ia supernovae (Ilkiewicz, K. & Mikolajewska, J., 2017) which will be discussed in the next section.

1.4 Novae

In binary systems, and depending on the orbital period, the companion can have an effect in shaping PNe (see Figure 1.1) and nebulae surrounding SySts. In this section the explosive nature of interacting binaries resulting in novae will be discussed. Novae, an abbreviation from latin *stella nova* meaning *new star*, is defined by the Oxford dictionary as “*a star showing a sudden large increase in brightness and then slowly returning to its original state over a few months.*”, which is what ancient astronomers believed they witnessed before the brightness faded and eventually disappeared.

Since then, our research and understanding of novae has evolved such that there are now many categories and definitions when describing novae and their eruptions. The remainder of this section will focus on distinguishing between classical, recurrent, dwarf and supernovae, their characteristics, formation and morphologies. Refer to Bode & Evans (2008) for a comprehensive overview of classical nova evolution.

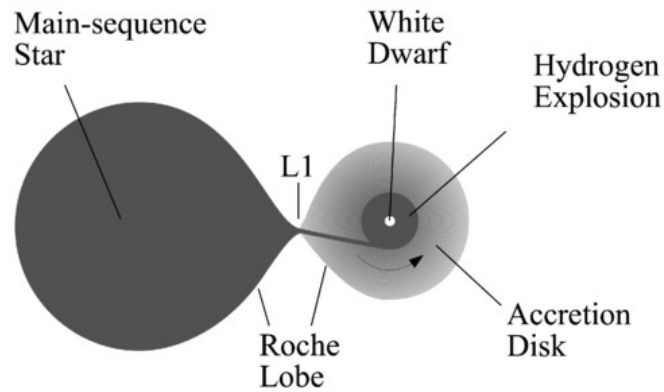


Figure 1.12: A classical nova is a thermonuclear explosion that occurs on the surface of a white dwarf star that is in a close orbit with a main-sequence star. The strong gravitational attraction of the white dwarf pulls its nearby companion into an elongated shape, whose outer edge is designated the Roche lobe. Some of the hydrogen in the outer atmosphere of the main-sequence star spills over at the inner Lagrangian point, denoted L1, where the gravitational pull of the two stars is equal. This hydrogen spirals into a rotating accretion disk and down to the white dwarf, igniting a thermonuclear explosion. Image: © https://ase.tufts.edu/cosmos/print_images.asp?id=52.

1.4.1 Types of novae

A cataclysmic variable (CV) is an interacting binary system culminating in sudden bursts in luminosity from an eruption. They are distinguishable from SySts in that SySts have wider orbital periods such that a) the primary does not fill its Roche lobe prior to becoming a WD, b) the primary becomes a thermal pulsing AGB star with a dusty wind and avoids a common envelope or c) the initial components are of a comparable mass and no orbital shrinkage is observed as their Roche lobes are not filled. Components of CVs consist of a WD and companion that is a near, or Roche lobe filling star. CVs encompass classical, recurrent and dwarf novae, i.e. systems containing a WD and a companion (Bode & Evans, 2008).

Classical novae

A CV which has only been observed to have erupted once is known as classical nova. The eruption is the result of accretion of hydrogen-rich material onto the WD from its companion, typically a giant or low-mass star (see Figure 1.13). As the layer of H-rich material forms, it is both compressed and heated by strong sur-

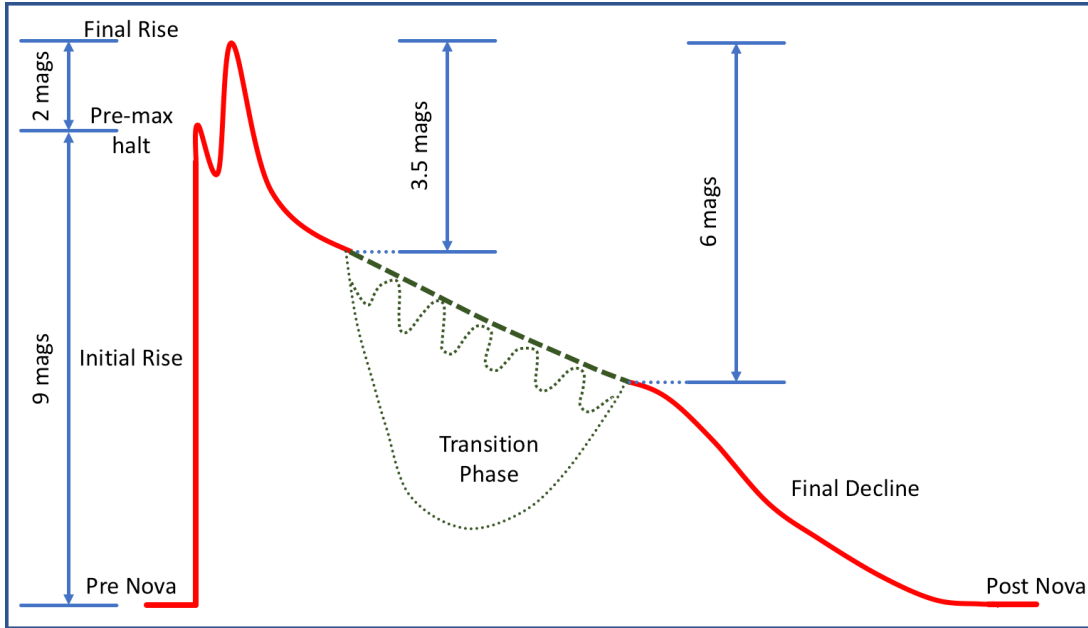


Figure 1.13: An example of the morphology of a nova light curve . Once eruption occurs, novae go through a period they brighten quickly, shortly after maximum luminosity is reached, they gradually decline. As can be seen from the diagram, there are some novae whose decline goes uninterrupted, others go through phases of oscillations or experience a strong prolonged dip in luminosity. Figure reproduced from (Bode & Evans, 2008)

face gravity, once this material reaches a critical mass a thermonuclear runaway (TNR) explosion occurs. Eruptions can reach temperatures $\sim 1-4 \times 10^8$ K within seconds (Starrfield *et al.*, 2016), expelling a mean mass of material $\sim 2 \times 10^{-4} M_{\odot}$ (Gehrz *et al.*, 1998) at velocities $\sim 1000 \text{ km s}^{-1}$, leading to a rise and fall in brightness (6 – 20 magnitudes) spanning anything from days to months (Bode, 2010). As each event is unique, so is their expansion and morphology which are also affected by the companion star and any pre-existing circumstellar material that might exist in the form of a accretion disc and common envelope (Santamaría *et al.*, 2020). McLaughlin (1939) discovered that the compressed timescales of multiple optical light curves resembled each other, an example of this idealised light curve is illustrated in Figure 1.13.

Recurrent novae

After the eruption of a classical nova, the white dwarf will survive the TNR event, and over time the process may occur again, this phenomenon is known

as a recurrent nova. It is believed that all classical novae are recurrent as the intervals between eruptions are in general greater than our observational baseline ($\geq 10^4 - 10^5$ years [Hernanz & José, 2008](#)). Such systems contain large mass WD ($\sim 1.4 M_{\odot}$) with a high mass-accretion ($\sim 10^{-7} M_{\odot}$) and steady burning rate ([Darnley *et al.*, 2019](#), and authors therein). Outbursts from recurrent novae typically are observed with apparent magnitudes ranging from 4 – 9 with multiple occurrences at intervals of approximately 1 – 120 years ([Warner, 1995](#)). The mass of the WD is suggested to increase after each outburst making recurrent novae possible supernova type Ia progenitors ([Hernanz & José, 2008](#); [Wang & Han, 2012](#); [Wang, 2018](#)). Recurrent novae are rare with approximately 10 known systems in the Milky Way and several others identified in M31 and the large Magellanic cloud. The most frequently recurring nova is M13N 2008-12a, which erupts annually and is located in the Andromeda galaxy consists of a WD with $1.38 M_{\odot}$ and accretion rate of $\sim 1.6 \times 10^{-7} M_{\odot} \text{ yr}^{-1}$ ([Darnley *et al.*, 2016](#)).

Dwarf novae

Another type of CV where outbursts occur regularly is a dwarf novae. In this scenario, the outburst occurs as a result of thermal instability due to a disturbance in the magnetic field of the WD, change in viscosity of the accretion disk, or clumpy accretion, leading to a increase of luminosity in the accretion disk. Recurring eruptions for dwarf novae range from days to decades ([Warner, 1995](#)), where an eruption results in an increase in brightness of 2 – 6 magnitudes ([Osaki, 1996](#)) and can accelerate winds to the order of $1 - 6 \times 10^3 \text{ km s}^{-1}$ ([Kafka & Honeycutt, 2004](#)).

Type I Supernovae

There are more powerful classifications of novae which shine brighter than entire galaxies for a short period of time, these are known as supernova. Eruptions from these types of novae are so powerful that approximately half of the star's mass is ejected with velocities one hundredth the speed of light, and the sudden

increase in brightness of supernova eruptions in other galaxies is distinguishable against its normal unresolvable stellar background (Dyson & Williams, 1997). Tsebrenko & Soker (2013), and authors therein describe how SNe Ia remnants may be formed from the following scenarios:

- Single degenerate: WD accretes mass from a non-degenerate stellar companion
- Double degenerate: Merger of two WDs takes place
- Core-degenerate: WD merges with a hot core of a massive AGB star
- Double-detonation: A sub-Chandrasekhar mass WD accumulates on its surface a layer of helium-rich material, which can detonate and lead to a second detonation near the center of the CO WD

Supernova are categorised by two types, Type I and Type II where Type I is further subdivided into *Ia*, *Ib*, *Ic* and *Id*. Supernovae Type Ia (SNe Ia) are generally believed to be the result of thermonuclear destruction of a carbon-oxygen WD exceeding the Chandrasekhar limit by accreting material from a non-degenerate companion star. Type II supernovae progenitors are massive stars with $\gtrsim 8 M_{\odot}$ whose central core collapses under its own gravity and explodes, and are characterised by H emission spectra. Out of these two types, SNe Ia ejects the lower mass, $\sim 1 M_{\odot}$ while a Type II ejects $\sim 10 M_{\odot}$. SNe Ia do not show hydrogen emission lines suggesting that their source are hydrogen-deficient stars whose subcategories are identifiable by their emission spectrum; *Ia* display Si lines, *Ib* display He but no Si lines, and *Ic* display no He lines (Osterbrock & Ferland, 2006).

1.4.2 Nova shells

There are several theories regarding nova shell shaping mechanisms based on nova type and of stars involved. Two common categories include; shaping due to ejection of a fast-rotating WD or common envelope evolution where the

expelled material is shaped by the companion star (see [Nordhaus & Blackman, 2006](#); [Scott, 2000](#), and authors therein). The nebular remnants produced from nova outbursts are event dependant, producing varying morphologies and offer important information regarding morphology, evolution, distance indicators and interactions with both circumstellar and interstellar media. Typical classical novae outbursts start with slower wind velocities ($500 - 2000 \text{ km s}^{-1}$) followed by a longer phase of faster wind velocities ($1000 - 4000 \text{ km s}^{-1}$). The mass ejected interacts with these winds to form a double shock structure; the secondary faster wind catching up and subsequently passing through the primary ejected slower wind, eventually dissipating and cooling as it expands. Structure of the remnant may be further influenced by angular momentum from the rotation of the WD and binary companion influenced ([O'Brien & Lloyd, 1994](#); [Bode & Evans, 2008](#); [Santamaría *et al.*, 2020](#)).

The extreme and dynamic nature of novae outbursts are in contrast to the slower evolution of PNe. Where nebulosity remains for PNe for thousands of years with little if any visible change in structure, novae remnants occur on timescales comparable to that of human life. Timescales for shell dispersal is important to assess durations for the different stages of hibernation between a classic nova eruption and their parent cataclysmic variables ([Santamaría *et al.*, 2020](#)).

Examples of the visible change in nova remnants is illustrated in [Figure 1.14](#) where [Santamaría *et al.* \(2020\)](#) obtained narrowband images of 5 nova shells; T Aur, V476 Cyg, DQ Her, V533 Her and FH Ser, over two epochs. Images from 2016–2019 were acquired using the Alhambra Faint Object Spectrograph and Camera (ALFOSC) at the 2.5 m Nordic Optical Telescope (NOT) of the Roque de los Muchachos Observatory in La Palma, Spain. Archival images of each nova were downloaded from multiple sources; European Space Observatory (ESO) Science Archive Facility Isaac Newton Group (ING), Mikulski Archive for Space Telescopes and Hubble Legacy Archive at the Space Telescope Science Institute.

The collection of novae in [Figure 1.14](#) all have varying elliptical morphologies

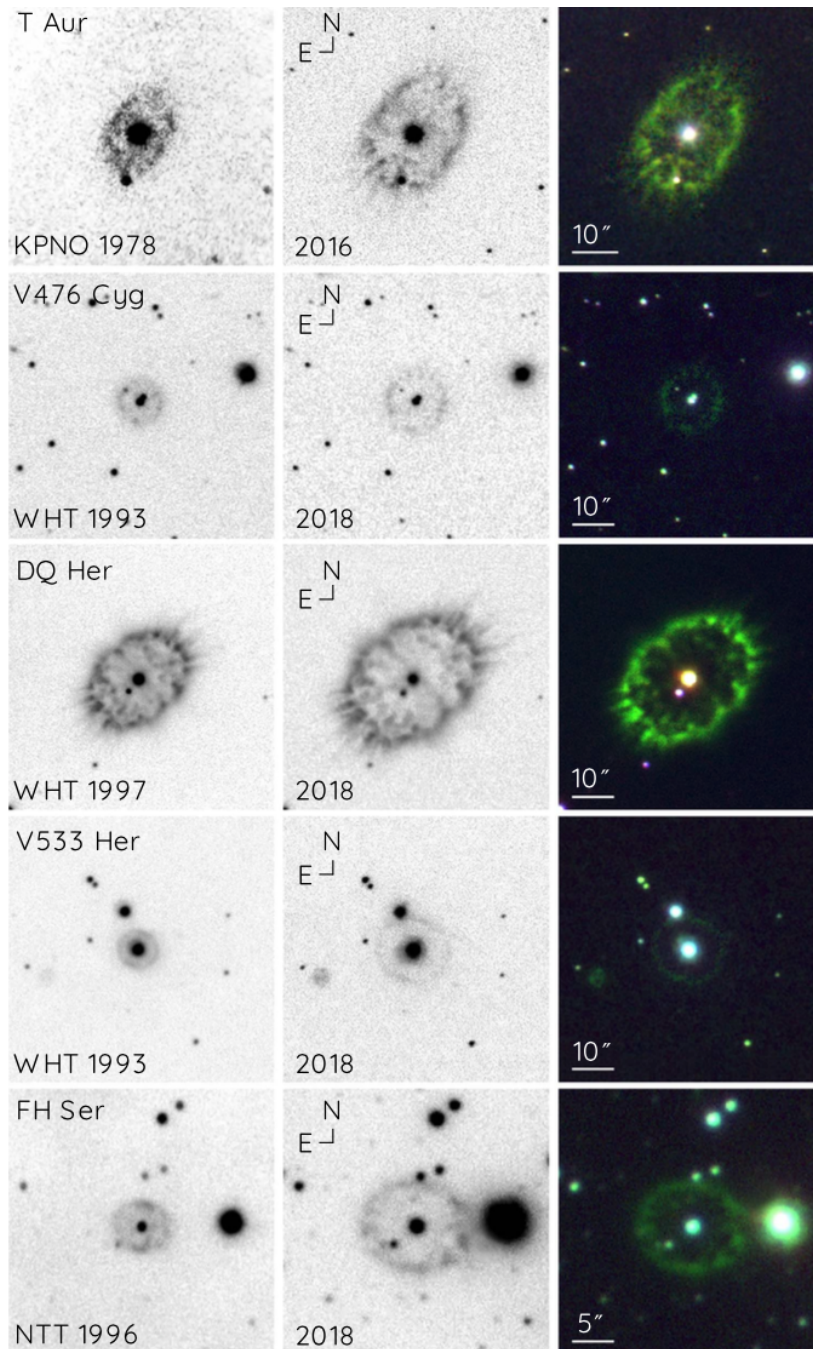


Figure 1.14: Multi-epoch images of nova shells surrounding T Aur, V476 Ctg DQ Her, V533 Her and FH Ser. $H\alpha$ images are aligned along the left most and centre column, images in the right column are RGB composite colour of SDSS 4800Å (blue), $H\alpha$ 6563Å (green) and [N II] 6583Å (red) filters, apart from V476 Cyg whose colour images was obtained using an DSDD 6180Å filter for the red. Image ownership and origin (Santamaría *et al.*, 2020).

with both smooth and knotty structures visible. Column 1 and 2 clearly show the expansion of the nebulae between the epochs, more careful examinations of the multi-epoch images like these can reveal small scale variations regarding change

in size and distribution of clumps. [Santamaría *et al.* \(2020\)](#) investigation focused on the angular expansion of this sample of nebulae, and determined that the initial expansion velocity remains and based on the linear increase of size with time, this speed will continue. Discrepancies were noted with some novae i.e. T Aur and V476 due to poor quality of data from the earlier epoch.

1.5 Thesis Overview

The aim of the work presented in this thesis is to develop a novel technique and application for generating photoionisation models of PNe and novae generated by CLOUDY¹⁰ ([Ferland *et al.*, 1998](#); [van Hoof *et al.*, 2000](#); [Ferland *et al.*, 2013, 2017](#)) and PYCLOUDY¹¹ ([Morisset, 2013](#)), using 3D models generated using SHAPE¹² modelling software ([Steffen & Koning, 2011](#)). CLOUDY is a large-scale spectral synthesis code designed to simulate physical conditions within an astronomical plasma and then predict the emitted spectrum. PYCLOUDY is a Python library that handles CLOUDY input and output files while also generating pseudo 3D renderings from various runs of the 1D CLOUDY code. Users can generate emission line ratio maps, position-velocity (PV) diagrams, line profiles, and channel maps, once an expansion velocity field is given (See e.g. [Gesicki *et al.*, 2016](#)). It is significantly faster than full 3D photoionisation codes (e.g. MOCASSIN [Ercolano *et al.*, 2003](#)), allowing users to explore a wide space of parameters quickly.

SHAPE is a morpho-kinematic modelling and reconstruction tool for astrophysical objects. Users bring any knowledge of the structure and physical characteristics of the source (e.g. symmetries, overall appearance, brightness variations) to construct an initial model which can be visualised. The model can be compared to observational data allowing for interactive and iterative refinement of the model. Once all necessary physical information are reflected in the model, its parameters can be automatically optimised, minimising the difference

¹⁰Available under general use (open source licence): <http://www.nublado.org>

¹¹Available online: <https://sites.google.com/site/pycloudy/>

¹²<https://wsteffen75.wixsite.com/website> for the new release of SHAPE

between the model and the observational data. The final model can then be used to generate various types of graphical output.

Separately, these codes and application have had a huge impact in astronomy and astrophysics research since their earliest release, but have never been combined in such a way as is presented in this research. The resulting code presented here is PYCROSS, an acronym for “PYCLOUDY *Rendering of SHAPE Software*”, that allows users to generate sophisticated photoionisation models of PNe and novae without the need for any prior coding experience, nor the need to derive complex mathematical models. The following is an overview of the content contained within each chapter and its context to the thesis as a whole.

Chapter 2 discusses current photoionisation software modelling codes and techniques and the need for a formal software development lifecycle being employed in the development of astronomy/astrophysics applications. The complexity and steep learning curve needed for astronomers to use new codes is reinforced with current advances in hardware, software and volume of data being generated and stored. A new novel application for generating pseudo-3D photoionisation models of PNe and novae is described. Developing PYCROSS, from conception to coding, testing and deployment is discussed. Detailed accounts of the installation, functionality, user interface and operational overview of PYCROSS is given using a theoretical model generated in SHAPE as an example. Results from this chapter has been published in [Fitzgerald *et al.* \(2019, 2020\)](#).

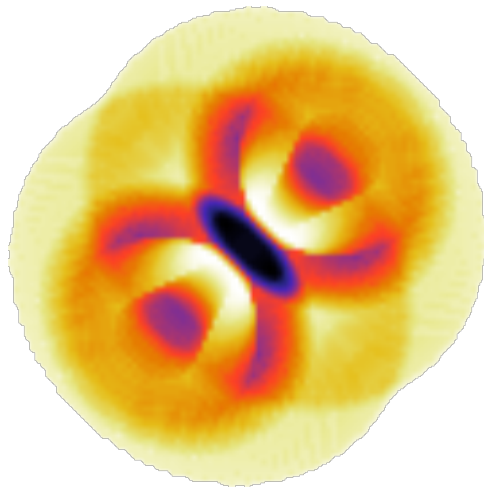
Chapter 3 will discuss an operational overview and a scientific pipeline with scenarios where PYCROSS has been adopted for novae (V5668 Sagittarii (2015) & V4362 Sagittarii (1994)) and a PN (LoTr1). Parameter sweeps from published literature, shape models and three scientific pipelines are described for each target, outlining the various methods of creating models. In this chapter, PYCROSS was used for the first time to generate photoionisation models on PN. Findings from this chapter have been published in [Harvey *et al.* \(2018\)](#); [Fitzgerald *et al.* \(2020\)](#); [Harvey *et al.* \(2020\)](#).

Chapter 4 The first release of PYCROSS (Fitzgerald *et al.*, 2020) and models therein, was developed using Python 2.7 for CLOUDY 13 (C13) and was only available for MAC OS. Since then, and based on requests from the greater astronomy community, it has been updated to Python 3.7 to work with CLOUDY 17 (C17, Ferland *et al.*, 2017) on both MAC and Windows platforms. This chapter outlines the updated version of PYCROSS. It also describes the structure and kinematics of “*The Etched Hourglass Nebula*”. PYCROSS models were created from data acquired from previous research where authors investigated certain aspects concerning evolution, continuum, shaping and kinematics. Extrapolating necessary information from the literature allowed for the creation of a SHAPE model and refining the parameter space as inputs into PYCROSS to create the models. The method outlined in this chapter differs slightly from that described in Chapter 3 (Fitzgerald *et al.*, 2020), highlighting its ability to create models in different ways based on observations and information available. Finally, new nebular diagnostic functionality is demonstrated to show how regions within the nebula can be analysed to determine densities and temperatures of different ionised states of O, N, H and He. Results from this chapter have been submitted for publication to the journal *Astronomy & Computing*.

Chapter 5: Finally, this chapter marks the conclusion of this thesis, presenting a summary, conclusions and suggestions for future work and possible paths for the PYCROSS code.

Chapter 2

Software development in astronomy



2.1 Introduction

Some of the most iconic images of modern astronomy are of nebulae, made visible through emission lines in photoionized gas. The study of such photoionised gas has played a major role in understanding a number of physical processes ranging from atomic physics to stellar evolution theories. Visible light from nebulae originates directly from photoionised gas at an equilibrium temperature of approximately 10^3 – 10^4 K (Osterbrock & Ferland, 2006). As PN central stars have very high temperatures, the gas is excited by ultraviolet radiation from a central star with a very high surface temperature. For nova and supernova remnants, shockwaves in the initial explosion flash ionises the gas. In both cases, recombinations into any state other than the ground state (which produce UV photons that are promptly reabsorbed) lead to escape of photons from the nebula rendering them visible particularly at optical wavelengths. Nebulae whose exterior boundary occurs at the outer edge of the gas are referred to as “*matter-bound*”. In contrast, “*radiation-bound*” nebulae occur when the hydrogen ionisation front defines the outer boundary, as seen in visible light, since ionisation fronts can also be imaged in the UV and IR. In the latter case, more gas will be present beyond the visible boundary, and may emit in longer wavelengths in a ‘photon dominated region’. Finally, reflection nebulae are caused by scattered starlight (e.g. around the Pleiades star cluster) rather than photoionisation.

This chapter will focus on the software development in astronomy. Various modelling techniques, codes, programming paradigms and the advantages for employing a software development lifecycle will be discussed. A detailed description of the development, functionality and an operational overview of the code created during this research will be given where the focus is restricted to optical emission from inside photoionised nebulae.

2.2 Modelling software

Nebulae spectra consist predominately of emission lines, a result of ionisation from UV radiation emitted from a post asymptotic giant branch (AGB) star and interaction of electrons within the nebula. These lines are categorised as either recombination lines: formed when an ion and an electron combine, leading to a cascade of the electron down to the ground state, or collisionally excited lines: formed when electrons collide with atoms or ions within the gas, and excite them. When these excited atoms or ions revert to a lower level, they will emit a photon. Lines known as ‘*forbidden lines*’ do not occur under terrestrial conditions, and are denoted by square brackets, (e.g [N II], [O III] etc.). Abundances of elements within a nebula are generally expressed as a ratio in comparison to the intensity of the hydrogen beta line (i.e. $H\beta$ 4861Å). Spectroscopic analysis can determine chemical composition, density, velocities and temperatures of regions within a nebula.

Research into the processes of photoionised gas plays a huge part in our understanding of stellar evolution, which is why so much effort has been put into creating tools to help visualise it. Through the analysis of such lines, accompanied by photoionisation models, the physical condition and chemical abundances of PNe and novae can be further understood. In order to create a visual representation of an ionised nebula, a modelling code to derive temperature, density, chemical composition, and other physical quantities is required. To aid in defining the initial values for 3D photoionisation models interactive databases, such as PyNeb (Luridiana, V. *et al.*, 2015), are available that aid the user in deriving physical conditions of a nebula based on observed spectral line ratios.

Modelling non-stellar objects beyond our solar system is difficult as 3D volumetric objects are observed as 2D projections. Currently there are a number of codes available that use various analytical or statistical techniques for the transfer of continuum radiation, mainly under the assumption of spherical symmetry. Increased computing power has further enhanced the development of photoionisation codes, allowing for the construction of more complex models reconstructed

into 3D. However in some cases, the assumption of spherical symmetry has been retained (Ercolano, 2005). Two leading contributions to this area include MOCASSIN and CLOUDY.

MOCASSIN (MONte CARlo SimulationS of Ionised Nebulae), described in Ercolano *et al.* (2003), is a code designed to build realistic models of photoionised nebulae having arbitrary geometry and density distributions, with both the stellar and diffuse radiation fields treated self-consistently. This Monte Carlo approach was developed to provide a fully 3D modelling tool capable of dealing with asymmetric and/or inhomogeneous nebulae, as well as, if required, multiple, non-centrally located exciting stars. The time taken to run/converge simulations and renderings on a standard desktop ranges from a number of hours to days. An alternative to this is the pseudo 3D technique of CLOUDY (Ferland *et al.*, 1998; van Hoof *et al.*, 2000; Ferland *et al.*, 2013, 2017). CLOUDY is a large-scale spectral synthesis code designed to simulate physical conditions within an astrophysical plasma and then predict the emitted spectrum. CLOUDY 3D¹³ is an IDL library to compute pseudo 3D photoionisation models by interpolating radial profiles between several 1D CLOUDY models. Users can generate emission line ratio maps, position-velocity (PV) diagrams, and channel maps, once an expansion velocity field is given. It is significantly faster than full 3D photoionisation codes, allowing users to explore a wide space of parameters quickly. Morisset (2013) developed PYCLOUDY, a Python library that handles input and output files of the CLOUDY photoionisation code. PYCLOUDY can also generate pseudo 3D renderings from various runs of the 1D CLOUDY code. Refer to Mehdipour *et al.* (2016) for a detailed comparison of photoionisation plasma codes with application to spectroscopic studies.

Typically only 1D velocity information is available from the Doppler shifting of lines along the lines of sight. In special cases, if velocities are high enough and the sources are close enough, then *proper motions* can be observed, where, over time, the nebula features can be observed to advance on the plane of the sky.

¹³Cloudy3D is available online <https://sites.google.com/site/cloudy3d/>

Regarding novae and nebulae, photographic images provide a 2D integration of the emission and absorption along the line-of-sight, but the depth information is flattened. Additional information may be assumed based on the symmetry and orientation of the object being observed. Depth information may also be extrapolated from velocity fields, e.g. mapping between velocity and position in radially expanding nova shells. This requires prior knowledge of the properties of the object being modelled. Alternative methods of modelling are required when theoretical or observational constraints are insufficient, one such example of this is SHAPE¹⁴ (Steffen *et al.*, 2011).

SHAPE is a morpho-kinematic modelling and reconstruction tool for astrophysical objects. Users bring any knowledge of the structure and physical characteristics of the source (e.g. symmetries, overall appearance, brightness variations) to construct an initial model which can be visualised. The model can be compared to observational data allowing for interactive and iterative refinement of the model. Once all necessary physical information are reflected in the model, its parameters can be automatically optimised, minimising the difference between the model and the observational data. The final model can then be used to generate various types of graphical output, Figure 2.1 shows a SHAPE model of PN M2-9 under an image of M2-9 acquired by NASA (refer to Figure 2.1). Recent examples where SHAPE has been employed to model PNe and novae include: Clyne *et al.* (2014) created a kinematical model of PN MyCn 18, utilising expansion velocities of its nebular components by means of position velocity (PV) arrays, to ascertain the kinematical age of the nebula and its components. Harvey *et al.* (2016) modelled the Firework nebula and discovered that the shell was cylindrical and not spherical as previously believed. The lower velocity polar structure in this model gave the best fit to the spectroscopy and imaging available. Derlopa *et al.* (2019) presented a morpho-kinematical model of PN HB4 using new Echelle spectroscopic data and high-resolution HST images. Derlopa *et al.* concluded that HB4 had an absolute mean expansion velocity of 14 km s^{-1} along

¹⁴SHAPE is available online: <http://www.astrosen.unam.mx/shape/index.html>

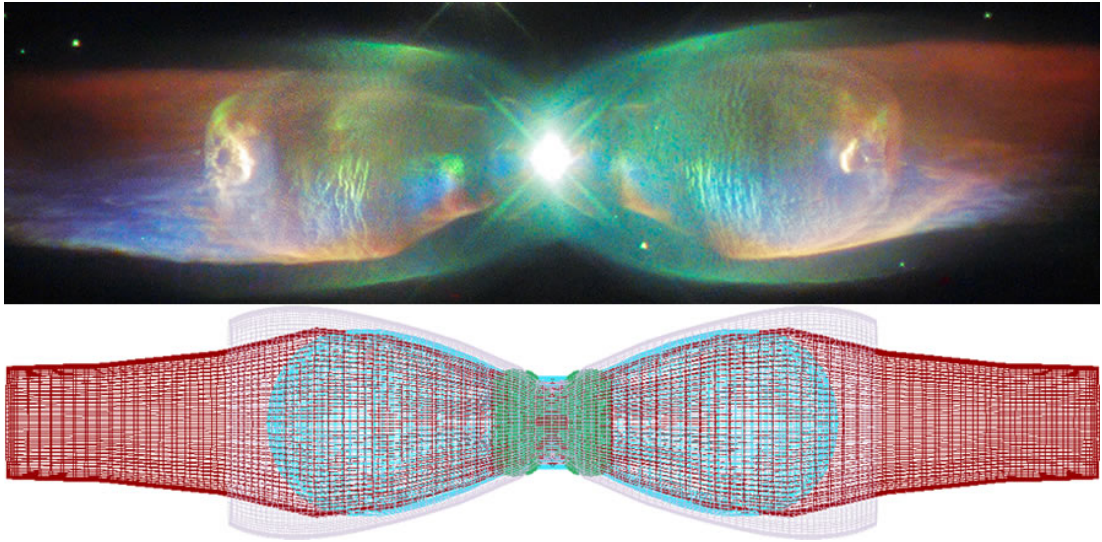


Figure 2.1: PNe M2-9: top image captured from NASA Hubble telescope and processed by Judy Schmidt, filters used: [S II], [O III] and $H\alpha$. Bottom image SHAPE 3D model. *Top image reproduced from <https://www.nasa.gov/feature/goddard/hubble-sees-the-wings-of-a-butterfly-the-twin-jet-nebula>* . Refer to Doyle *et al.* (2000) for more information regarding the morphology of M2-9.

the line of sight and proposed that the central part of the nebula consists of a binary system that has a Wolf–Rayet (WR) type companion evolved through the common-envelope channel. Refer to the following for more examples of SHAPE software used to model PNe and nova: Akras *et al.* (2016); Sabin *et al.* (2017); Santander-Garcia *et al.* (2017); Fang *et al.* (2018).

The steep learning curves encountered when installing, understanding and utilising specialist software are further compounded when astronomers are often required to develop/code software for specific tasks. A survey carried out by Momcheva & Tollerud (2015) focused on the use of software and the software skills of the participants in the worldwide astronomy community, between December 2014 and February 2015. Participants consisted of 1142 astronomers: 380 graduate students, 340 postdocs, 385 research scientists and faculty, and the remaining 37 consisted of undergraduate students, observatory scientists, etc. All survey participants responded “yes” when asked if they used software as part of their research; $11\pm 1\%$ of responders said they used software developed by others; $57\pm 2\%$ used software developed by themselves and others; while $33\pm 2\%$ said that they used software they developed themselves for specific purposes, as there

was no software readily available. This research also revealed the open source language, Python, to be the programming language of choice. However, there was no reference in this research to the software development lifecycle (SDLC) employed by developers in the astronomy domain.

The findings of [Momcheva & Tollerud \(2015\)](#) suggests that the astronomical software community is disconnected and scarce. Those that do develop their own codes in the community are protective of their work and slow to share. If and when collaborations do occur they are often committee and consensus-driven, and lead to very feature-rich goals, and often fail to achieve them ([Greenfield, 2011](#)). While it is difficult to ascertain if this situation and coding culture is unique to astronomy and astrophysics it has in recent years become a concern with efforts to identify key software development skills and how they can be incorporated into core graduate curriculums [Bauer *et al.* \(2019\)](#).

With advances in techniques, hardware and software it is of no surprise the number of astronomy software applications made available has increased considerably over the last decade which stem from the need to fulfil a specific purpose. A recent example can be seen where [Fitzgerald *et al.* \(2019\)](#) developed a standalone application (written in Python) for plotting photometric Colour Magnitude Diagrams (CMDs) using object orientated programming (OOP), a formal Software Design Lifecycle (SDLC) and Test Driven Development (TDD). This stand alone application worked “*out of the box*” required no installation of any additional software to function and emphasised the importance of quality and standards when developing software for astronomy.

2.3 Software development

High resolution imaging may detect shapes, however, better understanding of three dimensional structure is achieved when this data is coupled with spatially resolved, high resolution spectra to determine the kinematics of the gas within the nebula. To this end, a new application and pipeline that uses SHAPE soft-

ware to create 3D models with density, velocity and temperature properties is presented. The output of this is a data-cube which is processed by PYCROSS to generate CLOUDY photoionisation models of nebulae. This is achieved using an intuitive interactive graphical user interface (GUI) that does not require programming experience, execution scripts or the need to install additional compilers or libraries.

Prior to developing the software for this study, an investigation into which (if any) SDLCs utilised in the development of astronomy-specific software was carried out. Examples of promising software publications checked include [Collins *et al.* \(2017\)](#), [Konstantopoulos \(2015\)](#), [Sybilski *et al.* \(2014\)](#), [VanderPlas *et al.* \(2012\)](#), [Economou *et al.* \(2014\)](#), [Allen & Schmidt \(2015\)](#), [Bray \(2014\)](#), [Davies *et al.* \(2013\)](#), [Kent \(2013\)](#), [Goodman \(2012\)](#), and [McMullin *et al.* \(2007\)](#). With the exception of [Fitzgerald *et al.* \(2019\)](#), no information was found regarding the process (programming paradigms) by which the published astronomy-specific software was written, i.e. the developers do not state whether they employed any particular SDLC or test driven development (TDD: [Beck \(2002\)](#); [Astels \(2003\)](#)) approach. In order to preclude any selection bias, *every* paper was checked in the most recent year's volume of freely available Astronomical Data Analysis Software and Systems (ADASS) conference e-proceedings ([Taylor & Rosolowsky, 2015](#)) - choosing ADASS because of its pre-eminence as a forum for communicating best practice in this field. Not all of these 128 ADASS papers involve writing code - in fact, over half are concerned with other topics (databases, data standards and models, metadata and archive management, VO interfacing, creative use of archival data, collaborative workspaces, cloud computing, source code libraries). However, this investigation revealed that in nearly all cases where a code or pipeline was developed (typically using Python, Java, C or C++; sometimes in conjunction with MPI or Perl), it is described in terms of its algorithms and functionality, layers and internal architecture, external connectivity, inputs and outputs; but not in terms of its development approach. The few exceptions to this rule were [Ballester *et al.* \(2015\)](#), [Vallejo *et al.* \(2015\)](#), [Surace *et al.* \(2015\)](#) and

Mulumba *et al.* (2015). The first of these papers outlines a process of iterating with users on their requirements, but does not explicitly identify this approach by its name. The other three, in contrast, give comprehensive treatment to their Agile and User-Centred design methodologies. This investigation indicates that only the order of 5% of astronomical coding papers provide such information, and presumably this reflects the proportion of projects which take a SDLC approach.

The advantages of employing and adhering to a SDLC include: clarity in project objectives, requirements and estimates; more stable systems where missing functionality can be easily identified; developing a valuable relationship between users and developers. A lack of awareness of these benefits is an unfortunate aspect of the astronomical software development culture, and if unchecked can potentially lead to software/systems being over budget, delivered late, or missing functionality; and in worst cases, to complete project failure. So in an attempt to steer this culture, programming paradigms and the SDLC approach, including the advantages and disadvantages of various SDLCs will be described.

2.3.1 Programming paradigms

A SDLC defines a structured sequence of stages in software engineering to develop the intended software product. A TDD approach relies on a shorter development cycle, where requirements become specific test cases that the software must pass. Another factor to consider is determining which programming paradigm to use. In developing PYCROSS, emphasis was put on determining an appropriate SDLC approach and programming paradigm, while also setting out a strict set of requirements beforehand. This section will discuss the options available and justify the choices made.

Different paradigms allow for alternative approaches when developing software applications. However, it is important to note that while programming languages are usually classified by one paradigm, there are some languages - such as Python - that can handle multiple paradigms. The two most common programming paradigms are the *procedural paradigm* and the *object-oriented paradigm*.

Procedural programming relies on the premise that the coder utilises procedures (routines or subroutines) to operate and manipulate data. This type of programming is sequential in nature, and so not particularly complicated. Object-orientated programming (OOP) amalgamates procedures and data into *objects*, allowing for more complicated functionality, while minimising the amount of code required. Objects can either be independent or associated with other objects, and they interact by passing information to each other. In the instance where an object interacts with another object, regardless of their similarity or differences, then the object contains information about itself (*encapsulation*) and the objects it can interact with (*inheritance*). Inheritance enables new objects to inherit the properties and methods of existing objects. OOP also utilises *classes*, which are user-defined prototypes for an object. They define a set of attributes that characterise any object of the class. Classes allow for the generation of multiple objects of the same type that can be used anywhere in the code, allowing for a significant reduction in coding but also more flexibility and functionality when dealing with multiple objects of the same type. Inheritance may be exploited for further coding efficiencies: rather than creating a new object from scratch, developers can reference a pre-existing object or superclass and create a subclass based on the previous one, allowing them to reuse code and functionality more effectively.

Using OOP, developers can manage and break software projects down into smaller, more manageable modular problems, one object at a time. The modularity of objects makes trouble-shooting easier; encapsulation ensures that objects are self-contained and functionality contained within methods/functions specific to that class. When errors do occur, developers know where to look without having to navigate through large amounts of code. Another advantage of OOP is in software maintenance; applications may evolve by additional functionality or improvements to the user experience, and upgrades might be required to allow software to work on newer computer systems. While an OOP-based application requires a great deal of planning pre-release, less work is needed to maintain it

over time.

2.3.2 Agile software development

The Agile Software Development Lifecycle (ASDL) is a set of methodologies (four values and twelve principles) defined by the Agile Manifesto (Beck *et al.*, 2001). It values:

1. **Individuals and interactions** over processes and tools
2. **Working software** over comprehensive documentation
3. **Customer collaboration** over contract negotiation
4. **Responding to change** over following a plan

The twelve principles expand on these values in more detail, giving more emphasis to the items highlighted in bold. The ASDL is illustrated in Figure 2.2. It combines iterative and incremental process models, and focuses on adaptability and satisfaction by rapid delivery of working software products before the product is reviewed. During each development lifecycle, additional functionality is incorporated and tested. If the product meets the specification and satisfaction of the project owner, then the product is released to the market or end users; if not, then another iteration of the development phase begins after all incremental changes have been noted. Each development phase focuses on particular functionality.

A comparison of the ASDL and traditional software development lifecycles is presented in Table 2.1 (Leau *et al.*, 2012). This explains the main reasoning for choosing the ASDL over traditional SDL: the project (1) was relatively low scale, (2) had high customer involvement, and (3) was characterised by a changeable development direction and evolving user requirements. Table 2.2 (Sami, 2012) outlines the rubric used in deciding on the ASDL over the alternatives for this project; ASDL again scores highest or joint-highest in factors such as

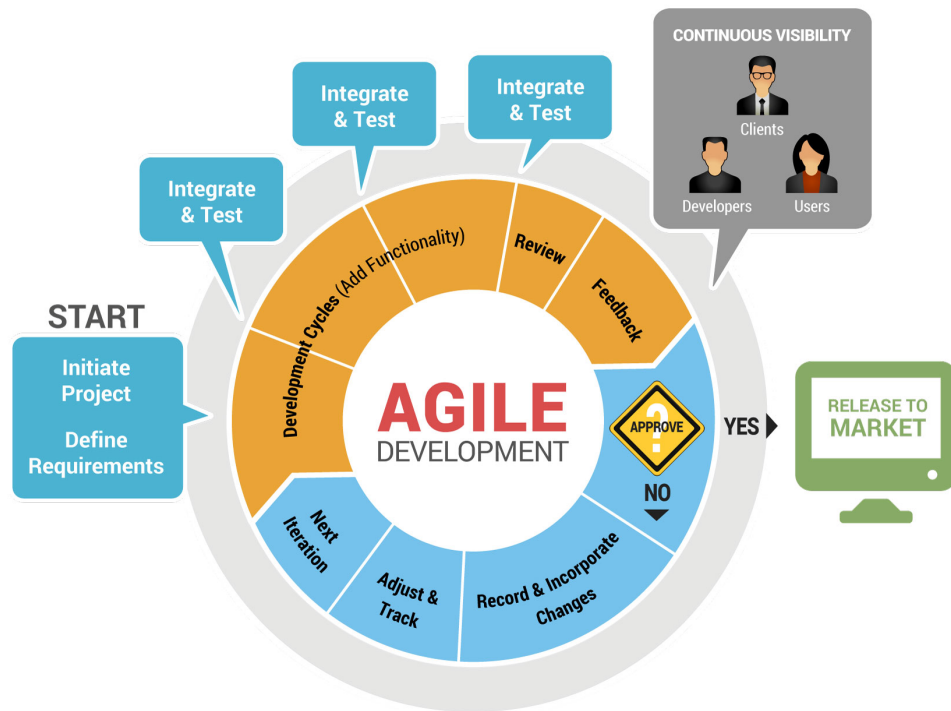


Figure 2.2: The agile software development lifecycle. Image reproduced from <https://i.pinimg.com/originals/ef/8e/b5/ef8eb517106cfc8574a34d05af000745.jpg>.

user requirement and “visibility of stakeholders” (another name for customer involvement), but low cost and short time schedule were also important in a busy, non-commercial, academic development team. It is important to note that the “customer” in this case is the end astronomer user and the software application and source code are open source.

The utilisation of the ASDL to develop the software proved extremely beneficial. *User stories* - concise, written descriptions of specific functionality that is valued to the user or owner of the software - were generated prior to the commencement of coding. A description of a user story follows the following template (Rehkopf, 2017):

As a [user role], I want to [goal], so i can [reason]

For example: *As an astronomer, I want to be able to take a 3D model generated in SHAPE and create numerous photoionisation models of different emissions, at different orientations and scales; and add annotation; so I can generate plots that can be used to demonstrate theoretical work or for publication.*

User stories must be detailed enough to start work; however, further details can be established and clarified as the project progresses. The scale of this project benefited the author as the overall goal and functionality of the software prior to and during development was well known. Regular communication and continuous inputs from customers (end users) left little room for guesswork regarding functionality. Requirements specified by the customers were developed into 17 user stories (often with some elements in common).

These user stories focused the development cycle for each iteration of the software and saved time: by allowing the developer to concentrate on breaking requirements down into functionality, this breaks a large project into smaller, more manageable tasks (in total 27 iterations were required, with 2-4 weeks allocated for each depending on the complexity of the functionality). For example, the above user story is accomplished by the following tasks:

1. Read in a data cube (.txt file) created in SHAPE
2. Set user defined radii
3. Perform necessary post processing on the data cube to make it acceptable for model generation
4. Creation of the necessary file and directory structure if it does not already exist
5. Retrieve user specified parameters regarding black body, luminosity, temperature, emissions line selection, abundances, additional CLOUDY options and angles options from the GUI.
6. Automatically save models regardless, this also takes into account if the name for each model does not change
7. Automatically access archived models
8. Access, extract and plot archived models
9. Generate data for models

10. Retrieve user specified parameters regarding annotation, emission lines or cuts selection, orientation and angles used for plot generation.
11. Display models
12. Delete temporary files.

Another benefit of having well defined user stories is the ability to anticipate the functionality of each software class and how they interact with each other. Upon completion, the project consisted of 15 classes, illustrated in the Unified Modelling Language (UML) diagram of [Figure 2.3](#); a description of each class is given in [Table 2.3](#).

	Agile	Traditional
User requirement	Iterative acquisition	Detailed user requirements are well defined before coding
Development direction	Readily changeable	Fixed
Testing	On every iteration	After coding phase completed
Customer involvement	High	Low
Extra quality required for developers	Interpersonal skills & basic business knowledge	Nothing in particular
Suitable project scale	Low to medium scaled	Large-scaled

Table 2.1: Agile SDLC versus Traditional SDLC models ([Leau et al., 2012](#))

Factors	Waterfall	V-Shaped	Evolutionary Prototyping	Spiral	Iterative & Incremental	Agile
Unclear User Requirement	Poor	Poor	Good	Excellent	Good	Excellent
Unfamiliar Technology	Poor	Poor	Excellent	Excellent	Good	Poor
Complex System	Good	Good	Excellent	Excellent	Good	Poor
Reliable system	Good	Good	Poor	Excellent	Good	Good
Short Time Schedule	Poor	Poor	Good	Poor	Excellent	Excellent
Strong Project Management	Excellent	Excellent	Excellent	Excellent	Excellent	Excellent
Cost limitation	Poor	Poor	Poor	Poor	Excellent	Excellent
Visibility of Stakeholders	Good	Good	Excellent	Excellent	Good	Excellent
Skills limitation	Good	Good	Poor	Poor	Good	Poor
Documentation	Excellent	Excellent	Good	Good	Excellent	Poor
Component reusability	Excellent	Excellent	Poor	Poor	Excellent	Poor

Table 2.2: Rubric used in deciding on the SDL for this project ([Sami, 2012](#))

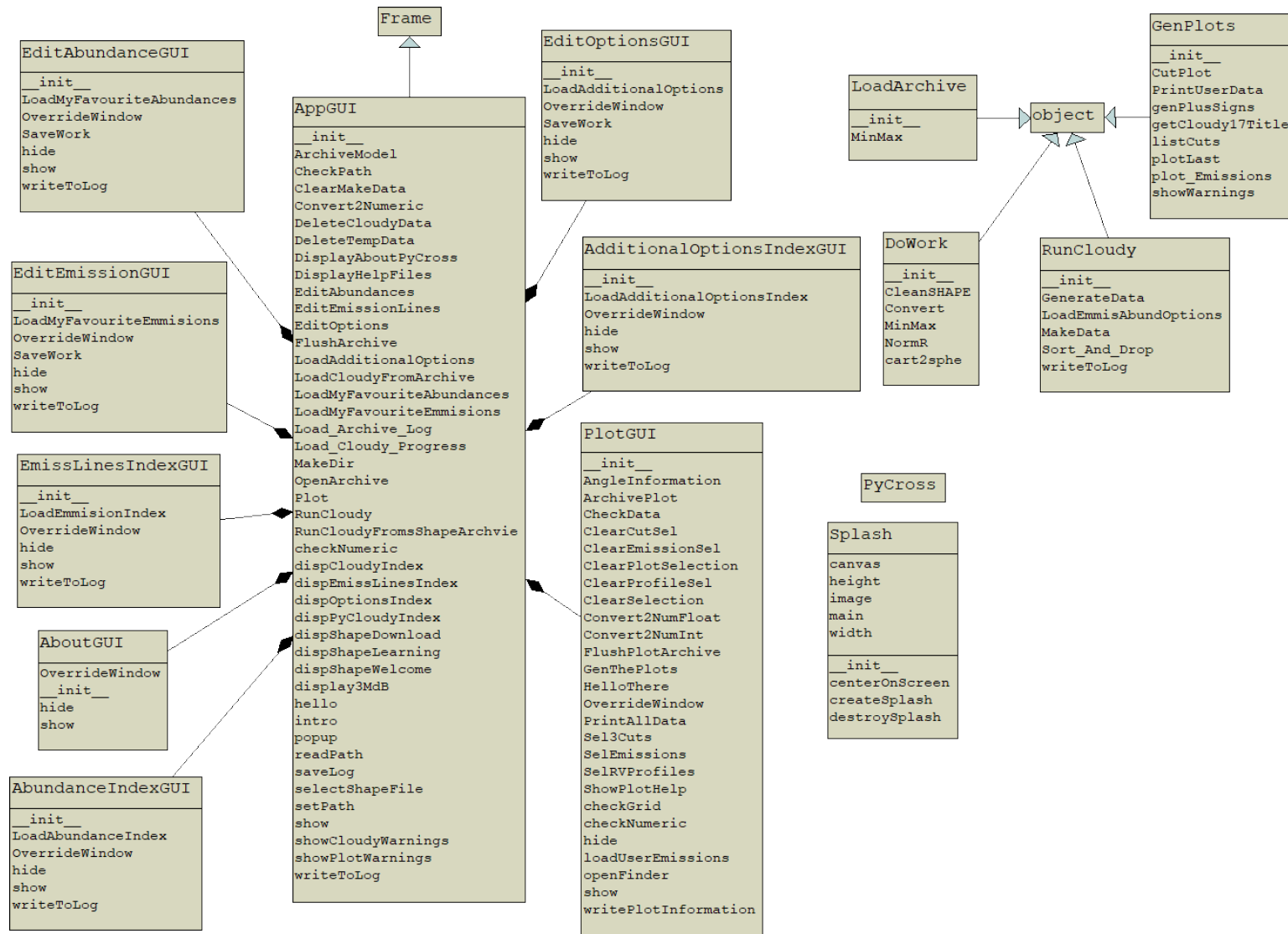


Figure 2.3: UML diagram representing relationships between the classes in the PYCROSS package. UML, short for Unified Modelling Language, is a standardised modelling language consisting of an integrated set of diagrams, developed to help system and software developers for specifying, visualising and constructing software. This diagram shows the classes and functions but not the variables within each class, this is due to size and resolution constraints.

2.3.3 Software testing

Software testing is essential in evaluating the quality, performance and accuracy of code by detecting differences between actual and expected outputs, for given inputs. The ASDL (Figure 2.2) recommends that this process be carried out during each development phase, to ensure *verification* and *validation* of the product. Verification ensures that the product satisfies the conditions imposed at the start of the development phase, to confirm that the application behaves as it should. Validation ensures the application satisfies the requirements at the end of the development phase to certify that it is built as per the customer requirements.

There are numerous types of software testing, which can be categorised as being either functional, non-functional or maintenance, with each containing many subcategories for specific purposes. An example of this is black and white box testing, both of which are a subcategory of functional testing, a testing methodology that validates the system against the user stories. Black box testing, named to signify that the application is like a black box and the tester is unable to see code inside, involves testing from a customer perspective. White box testing, assumes that the box is transparent and that the code is visible to the tester, asserts the quality of the code via statement coverage, branch coverage and path coverage by checking that each is executed at least once. The manual/non-automated testing methodologies used in the development of PYCROSS include:

Unit testing: Unit testing was done during and after the addition of new functionality by isolating that section of new code and testing it to verify its accuracy. A unit may refer to a individual function, module or object/class. This helps identify bugs early in the development lifecycle. Examples of unit tests carried out involved testing the function that normalises the SHAPE data cube to a specific range, another tests that the output from the previous test is passed to another function that converts the data to the correct coordinates system.

<i>Class Name (.py)</i>	<i>Description</i>
AboutPyCross	Window informing users of the application version, its creators and institution.
AbundancesIndex	Window to present users with online references and information for CLOUDY abundances. A web browser will automatically open and direct users to online resources when this window is opened.
AdditionalOptionsIndex	Windows that gives examples of CLOUDY options that users can use. Users are also presented with online resources and examples.
EditAbundances	Interactive window that allows users to add, remove and update any abundances set by the user.
EditEmissionLinesIndex	Interactive window that allows users to add, remove and update emission lines set by the user.
EditOptions	Interactive window that allows users to add, remove and update additional CLOUDY options.
EmissionLineIndex	Window presenting users with a full list of all emission lines that can be used with PYCROSS. Users can copy and paste lines from this window directly into <i>EditEmissionLineIndex</i> window. A web browser will automatically open and direct users to online resources with the most up-to-date list of emission lines.
DoWork	Class that takes the output generated from the <i>ShapeCloudy</i> class and generates models based on user requirements inputted from <i>TheGUI</i> , <i>EditAbundances</i> , <i>EditEmissionLinesIndex</i> and <i>EditOptions</i> classes. This class works with PYCLOUDY and CLOUDY to generate all necessary data for generating the plots.
LoadWorkArchive	Class which manages the loading and preprocessing of the the data contained within the data cube before it is passed to the <i>ShapeCloudy</i> class
Plot	Class performing all the plotting functionality for rotating and generating emissions and cut plots
PlotFrame	Interactive window allowing users to select emission lines and cuts they wish to plot. Additional options users can select are rotations, colour maps, zoom window and axis titles. All parameters set by the user are then passed to the Plot class.
PyCROSS	A class that starts the application, displays the splash screen and creates directories in the correct location if they don't already exist.
ShapeCloudy	This class handles the data cube, transforming the data so that it can be processed by PYCLOUDY and CLOUDY
SplashScreen	Creates and positions a splash screen with a logo in the centre of the monitor when the application starts.
TheGUI	This is the main interactive window allowing users to select a data cube, set emission lines, abundances, additional CLOUDY options, black body, luminosity and angles. Users can also select and plot previously created and archived models.

Table 2.3: Characteristics of each class within PYCROSS. The UML diagram for these classes can be seen in [Figure 2.3](#), examples of GUI's described can be seen in [Figure 2.5](#).

GUI & usability testing: GUI testing also checks to ensure that the layout of the interface is correct i.e. buttons, textfields, input fields and images are aligned and positioned correctly. This was done by the developer after new functionality is added to the GUI. Another type of GUI testing is to ensure that the application functions correctly based on user actions via mouse clicks, buttons, keyboard entries. These tests are done by both the developer and end users/customers of the application as part of their evaluation to provide feedback on its usability. Customers were asked to provide feedback on consistency, spelling, typography, behaviour, highlighting bugs or components that was not functioning correctly.

The software was developed and tested using the PyCharm IDE (integrated development environment) 2018 Community Edition, Python 2.7 with later iterations using Python 3.7 (see Chapter 4). The free community edition of PyCharm offers usage of both testing frameworks¹⁵ and code analysis tools. Code inspections detect - and suggest corrections for - compiling errors, code inefficiencies including unreachable code, unused code, non-localised string, unresolved method, memory leaks and even spelling mistakes. This code inspection feature is extremely useful in identifying and eliminating potential errors prior to running any unit testing.

2.3.4 Code freezing

Installation of astronomical software packages can be non-trivial, and a source of frustration. It is often the case that the end-user installs programming interpreters to execute code, only then to be informed that the software package requires the presence of another to work correctly, and that system paths must be set for referencing additional libraries. Other issues can arise when there are multiple versions of a particular programming language on a system (e.g. *Python 2* and *Python 3*).

Freezing of code allows for the creation of a single executable file that can

¹⁵PyCharm Testing Frameworks: <https://www.jetbrains.com/help/pycharm/testing-frameworks.html>

Tool	Apple OSX	Linux	Microsoft Windows
py2app	Yes	No	No
py2exe	No	No	Yes
pyInstaller	Yes	Yes	Yes
cx_Freeze	Yes	Yes	Yes

Table 2.4: Python freezing tools and the platforms they support. As this software was initially developed on OSX, *py2app* was used to freeze the code into a single file. Further single-file applications/executables were recently created ([section 4.1](#)) for Windows OS using *pyInstaller*.

be distributed to users. This application/executable contains all the code and any additional resources required to run the application, and includes the Python interpreter that it was developed on. The major advantage for distributing applications in this manner is that it will work immediately, without the need for the user to have the required version of Python (or any additional necessary libraries) installed on their system. A disadvantage of generating a single file is that it will be larger (approximately 183 MB), as all necessary libraries are incorporated. The increase in file size is acceptable when considering other issues, for example ease of installation, running, and portability to other platforms. Python freezing tools and platforms supported are listed in [Table 2.4](#).

2.4 PYCLOUDY Rendering of SHAPE Software

Over the course of this research, and for the first time, a new software tool has been developed called PYCROSS: PYCLOUDY Rendering of SHAPE Software (see [Figure 2.4](#)). This functional software package allows users to model 3D PNe and novae from interpreted spectra and imaging (using SHAPE), and will accurately predict and reproduce spectra for shells of different ages and types using functionality from PYCLOUDY.

Photoionisation models are generated by creating a 3D SHAPE model with appropriate structure, densities and velocities, a quadrant of the overall model is then sliced to produce a data cube, in the format of a text file ([subsection 2.4.2](#)), This is then inputted into PYCROSS which handles CLOUDY options/parameters

PYCLOUDY Rendering of SHAPE Software

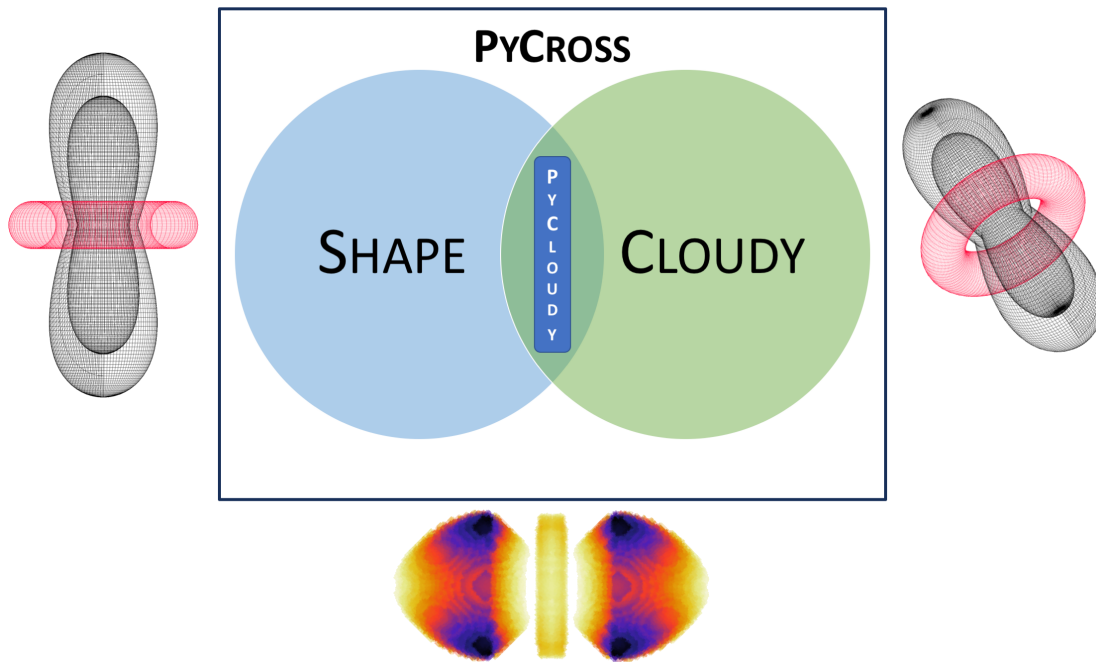


Figure 2.4: PYCROSS allows for the generation of 3D axisymmetric photoionisation emission maps generated using models generated in SHAPE. This is done via a novel code that utilises SHAPE CLOUDY and PYCLOUDY. 3D model are first created in SHAPE. The output from SHAPE is a data cube text file which is passed to PYCROSS. A detailed graphical overview of this process is illustrated in [Figure 2.5](#), an operational flowchart is illustrated in [Figure 2.6](#).

specified by the user. A high level operational overview following the path for creating a new model outlined in [Figure 2.5](#) and an operational flowchart is outlined in [Figure 2.6](#).

PYCROSS was developed and tested on OSX using the PyCharm IDE (integrated development environment) 2018 Community Edition, Python 2.7 with later iterations using Python 3.7 (Chapter 4). The free community edition of PyCharm offers usage of both testing frameworks and code analysis tools. There were 27 iterations of this application before the code was frozen, for release, allowing for the creation of a single executable file that can be distributed to users. The Agile SDLC approach employed in [Fitzgerald *et al.* \(2019\)](#) was adapted in the development of this software. The remainder of this section will outline installation, features and operational overview of the functionality when using PYCROSS.

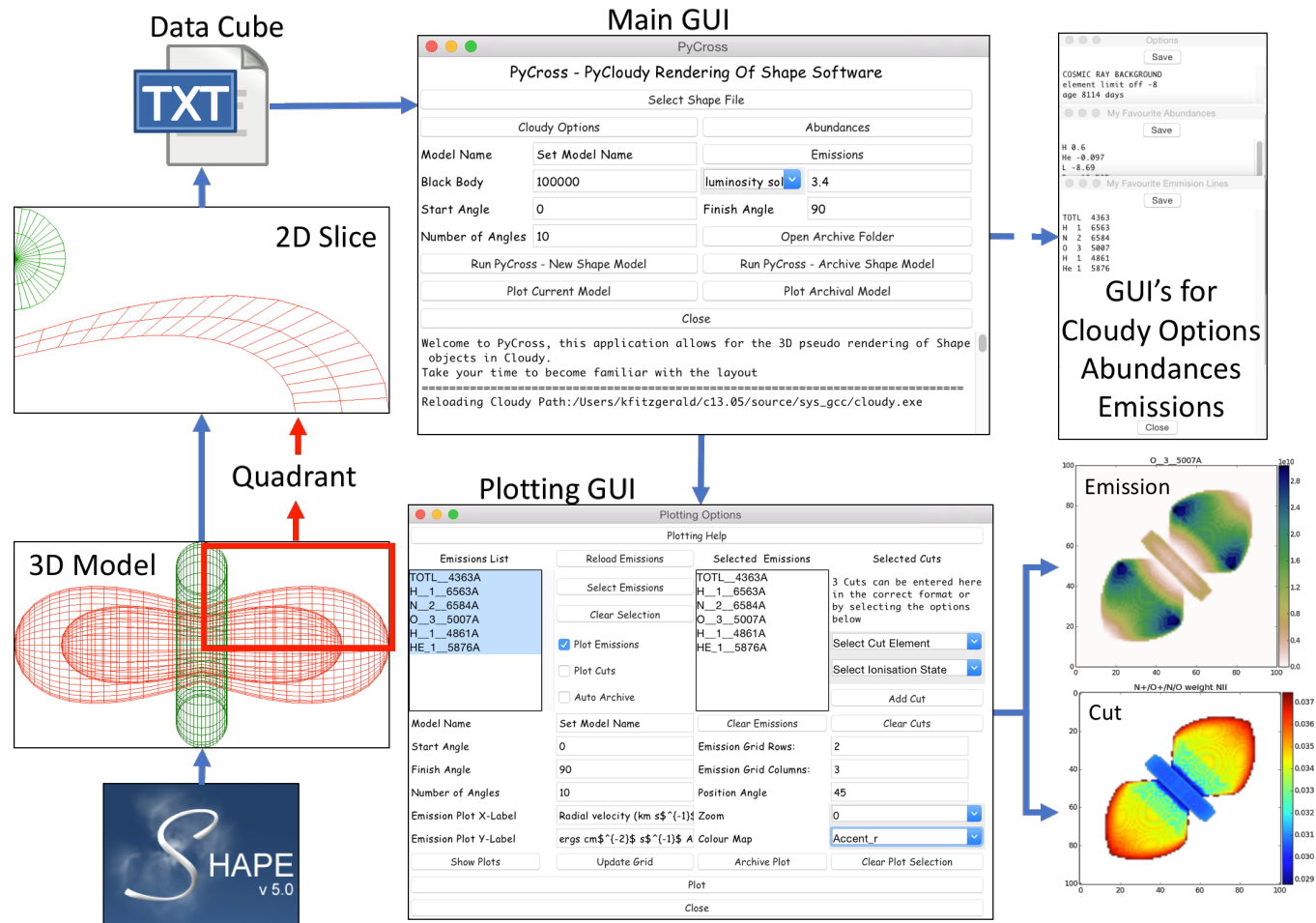


Figure 2.5: An operational flowchart outlining PYCROSS functionality is outlined in Figure 2.6. A new 3D SHAPE model is created with appropriate structure, densities and velocities. A quadrant of the overall model is then sliced to produce a data cube, in the format of a text file (subsection 2.4.2), which is inputted into PYCROSS. CLOUDY options/parameters are then specified and the model is run. PYCROSS's console will update informing the user of the progress. Once completed the user opens the plotting interface to plot the photoionisation and cut models (see bottom right of diagram) at different angles and inclinations. Colour map used for emission is `gist_earth_r`, one of 71 available to users. The model used here was designed as a theoretical nova with cosmic ray background and an approximate age of 8114 days, blackbody effective temperature of 50×10^3 K, luminosity of $3.6L_{\odot}$ and equatorial expansion velocity of 500 km s^{-1} and position angle of 45° . A scientific approach for determining optimum CLOUDY parameters is outlined in Figure 3.3

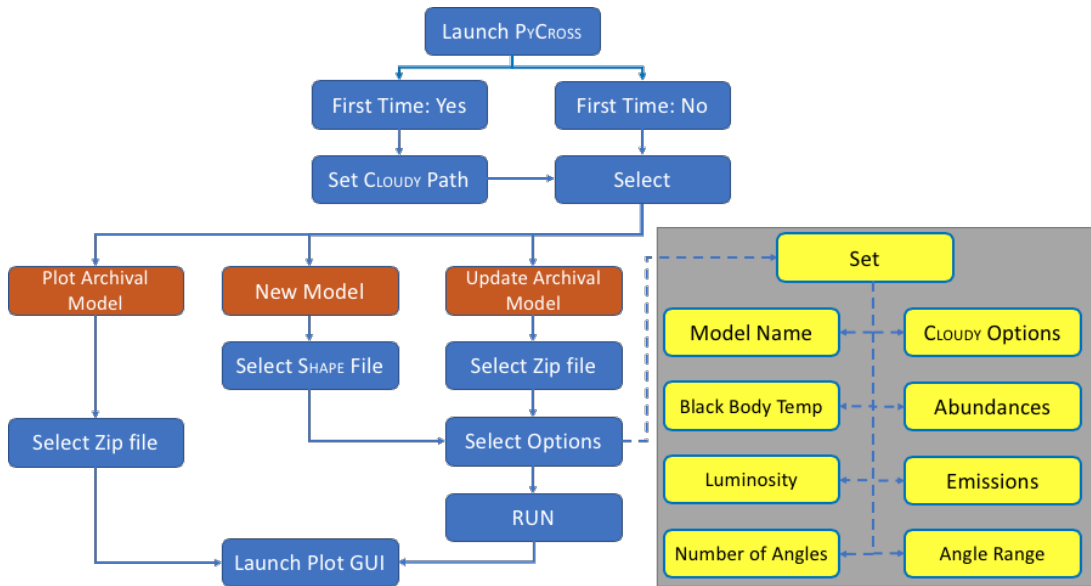


Figure 2.6: PYCROSS operational flowchart. Steps for generating new models, updating archived models by modifying CLOUDY parameters and visualising current and archived models. A high-level overview of the path to generate a new model is illustrated in Figure 2.5.

2.4.1 PYCROSS functionality

Functionality was identified during the gathering of user stories, however it is important to note that not all user stories were implemented. While the expertise of those providing user stories was of tremendous benefit, it was not possible to cater for each individual request for specific functionality, as some were deemed unnecessary or beyond the scope of the project for that iteration of development, and as such were discarded. Example of discarded user stories include:

- *”As a user I want to be able to plot line profiles for emissions within PYCROSS.”*
- *”As a user I want to be able to use PYCROSS as a nebular modeller in order to explore parameter space, such as a range of stellar T_e , radial density laws, distances or abundances.”*

The first user story was rejected during the session as it became clear that this functionality is already part of SHAPE, and recreating it within PYCROSS would be of no benefit. The second user story was suggested by a member of the

group with a specific desire to realise this functionality for their own purposes. After some discussion this user story was removed from the list to be discussed at a later date. All participants of the group agreed that priority be given to the following:

- *As an astronomer, I want to be able to take a 3D model generated in Shape and create numerous photoionisation models of different emissions, at different orientations and scales; and add annotation; so I can generate plots that can be used to demonstrate theoretical work or for publication.*
- *As a user of PYCROSS, I want to be able to have an efficient way of managing models generated.*
- *As a user I want be able to use PYCROSS via a user interface and not by command/terminal*
- *As a user I want be able to magnify the plot to look at the inner regions of nebulae*
- *As a user I don't want to have to installing any new versions of python or additional coding liberties*

These user stories provided the foundation that PYCROSS was built upon, resulting in a comprehensively designed code to allow for intuitive usability while also providing automated features allowing the user to be more productive. [Figure 2.5](#) follows the path for generating PYCROSS photoionisation rendering of a 3D SHAPE model utilising the application's two main GUIs, for creating and plotting models. Smaller windows are used to manage any CLOUDY preferences. A high-level operational overview of PYCROSS functionality is outlined in the operational flowchart in [Figure 2.6](#). As previously discussed, this application is “frozen” allowing for the creation of a single executable which contains all code and any additional python libraries to run. The only requirement is that CLOUDY is pre-installed on the user's system prior to running this programme.

A new directory structure is created in the root folder of the user computer when PYCROSS is loaded for the first time. This folder is named “*Py-CrossArchive*” and is the root/destination for all work generated by the application: the following folders and files are generated upon startup and modified during the execution of a model:

- ***Model-Name-Timestamp.zip***: PYCROSS models are automatically saved using the name assigned followed by a time-stamp of when they are created. The purpose of this is as follows: 1) To archive all models, this allows users the opportunity to review any change in parameters and resulting models generated. 2) A basic model can generate in excess of 100 files, each approximately 14.4 MB in size. While maintained within a well structured directory this can quickly consume disk space when generating a lot of models. Automatically zipping outputs to a single file significantly reduces file sizes (to approximately 3 MB zipped for a 14.4 MB un-zipped file) while also making it easier to process data at a later stage. For example, when handling these archived models, PYCROSS automatically extracts the contents of the selected zipped file into a temporary folder, and when finished the contents of the temporary folder are deleted. A time-stamp incorporated into the file name allows users to distinguish between models, if the model name does not change.
 - ***LogFile.txt***: A text file that records the parameters used by the user and information relating to the progress of a model as it is being run. This information is also displayed on the main GUI. This file can be used at a later stage to compare models based on their parameters but also to recreate models if needed.
 - ***MakeData***: This folder contains the output files generated by CLOUDY based on the SHAPE model.
 - ***TempData***: This folder contains data generated by PYCROSS that allows CLOUDY to run the selected SHAPE model. It is also used

to extract archive model data when modifying or plotting archived models.

- **Plots:** This folder contains the following sub-folders which store the generated plots of a model based on their type. Each time plots are generated the contents of this folder are deleted and replaced with new plots.
 - **Cuts:** This folder contains plots of the cuts generated. Cuts will be plotted based on their element and ionisation state. An additional $N^+/O^+/N/O$ weight NII cut, adapted from PYCLOUDY, is also plotted and saved here.
 - **Emissions:** Folder containing plots of the generated emission simulations.
 - **PlotArchiveInformation.txt:** This text file is updated automatically each time new plots are generated and contains information relating to the parameters entered by the user in the plotting options GUI, Plot GUI (see [Figure 2.5](#)), this feature is useful for tracking differences in plots based on their parameters.
- **PlotArchive:** All data generated and stored in the **Plots** folder can be exported here and automatically saved as zip files. This reduces time recreating plots at a later stage while also keeping track of parameters changed and carried out on Plot GUI:
 - **Auto Archive:** If this option is selected in the Plotting Options GUI then all current & subsequent data generated will automatically be exported to the PlotArchive folder as a zip file. If the user does not change the model name then the naming convention is updated to include the time generated, this ensures that no work is overwritten or lost.
 - **Archive Plot:** There is an archive current data option that can be accessed by clicking this button in the Plotting Options GUI.

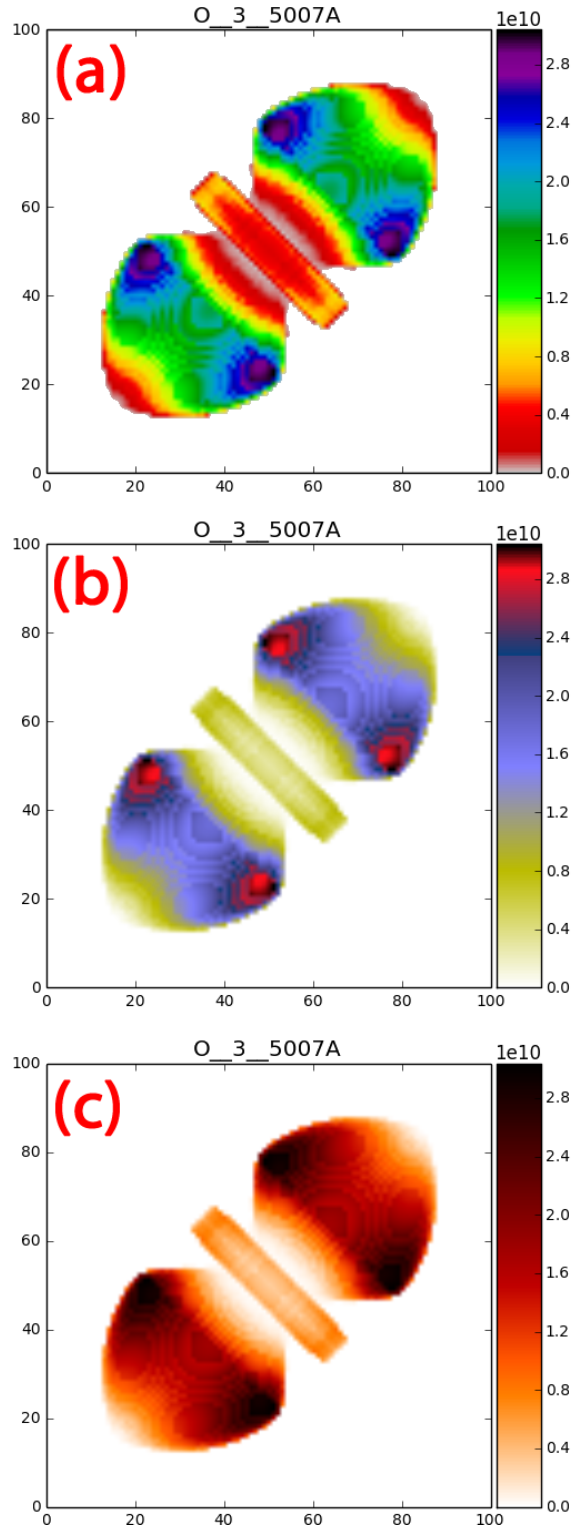


Figure 2.7: Three colour map examples from a choice of 71. The emission model of [OIII] 5007Å is derived from an example model (see Figure 2.5) with a position angle of 45°. Colour-bars correspond to the effective temperature of the ionising source, flux units in ergs s^{-1} . Scaled units of physical size are on x and y axes.

2.4.2 SHAPE data cube text file

The creation of the SHAPE file is essential to the generation of photoionisation models and as such is the first step in the pipeline (refer to [Figure 2.5](#)). A SHAPE model is based on observational data and can be informed by a combination of narrow-band imaging, medium-high resolution spectroscopy and polarimetry. If these data types are not all at hand, then they can be used individually with the application of some theory or in certain combinations, given data of good quality. Integral field unit spectroscopy can be a particularly powerful observational tool to aid in the derivation of nebular morpho-kinematics¹⁶. In this section the process on how to construct the output data cube from SHAPE for input into PYCROSS which is used in the *MakeData* and *TempData* files will be explained.

First users must derived the morphology of the nebular structure under study and assign a fixed or variable density structure. Next users must create a ‘cut’ of the nebula so it can be represented by a 2D array. To do this the user must place the nebula with its long axis pointing along the x-axis. Then a slice of a quarter of the major-axis of axisymmetric shape is taken, see [Figure 2.5](#) (2D Slice), Chapter 3, [Figure 3.3](#) panel 2(a) and [Figure 3.4](#) (c). This is done in the SHAPE 3D module. Users must first go to the object primitive, then take a slice of the nebula by setting $\phi_{min} = 90^\circ$, $\phi_{max} = 180^\circ$, $\theta_{min} = -91^\circ$ and $\theta_{max} = -89^\circ$.

Once users have made an appropriate 2D slice of their nebula they move to the SHAPE render tab. In this tab the renderer must be set to be *Physical*. The slit and image geometries are set to be square such that they overlap and cover the entirety of the 2D slice, again refer to [Figure 2.5](#) (2D Slice), [Figure 3.3](#), panel 2(a) and [Figure 3.4](#) (c) for how the structure should appear in the image render window. Finally users set up a text file to output the position and velocities along the x, y and z axes (Px, Py, Pz, Vx, Vy Vz) along with the corresponding density and temperature. This is done under “*Render*” in the Parameters section of SHAPE. When users click the Render button a text file will be generated

¹⁶To download and for a full description of the SHAPE software please visit: <http://bufadora.astrosen.unam.mx/shape/>

in a folder designated by the user. This text file is then imported directly into PYCROSS via its GUI. Currently only Px, Py, Pz and density arguments are used as input to the PYCROSS simulations. Temperature and velocity information will be utilised in the next iteration of PYCROSS.

2.4.3 User interface & operational overview

The Graphical user interface (GUI) is designed to be as intuitive as possible and consists of two main GUI windows. The first allows the user to set parameters and run models while the second controls the plotting, these interfaces pass information to each other to enhance efficiency. Other GUIs allow users to set additional CLOUDY options, emission lines and abundances. The operational flowchart of this application is illustrated in [Figure 2.6](#) and a high level overview of the GUIs taking the path of a new model is illustrated in [Figure 2.5](#). A scientific approach to determine optimum CLOUDY parameters is discussed in [Chapter 3](#) (see [Figure 3.3](#)). Once a SHAPE model, with a suitable morphology, density and velocity has been created it is then placed at an inclination of 90° . This 3D model must be represented two dimensionally, by taking a 2D slice of one quarter of the model. A data cube is created that describes the velocity and density at each position in the shell, this is processed by PYCROSS. A series of 1D CLOUDY simulations are computed along the 2D SHAPE model slice. Lastly, the 2D photoionisation map is wrapped and flipped in order to create the full pseudo 3D photoionisation model. Currently this technique is constrained to axisymmetric nebulae, but as discussed later this allows for the modelling of a large majority of PNe and novae.

The main GUI allows users to set the name of the current model, blackbody temperature, total luminosity, angle range (start-finish) and the number of angles in the range. CLOUDY preferences for the model general input, i.e. options, abundances and emissions are entered into smaller windows and when saved, will remain when the programme is started again. There is no limit to the number of parameters entered into these windows provided that they conform to valid

CLOUDY commands. This removes any learning curve, complex commands and the need to run shell scripts, thus increasing productivity. Once a model is successfully created the emissions list, set in the main GUI will be available and visible for selection in the plotting option GUI. Button functionality on the main GUI is as follows:

- **Select Shape File:** Allows the user to select the .txt data cube output from SHAPE (see [subsection 2.4.2](#)).
- **Cloudy Options:** Opens up a new window allowing the user to type/paste CLOUDY options, visible at the top left of [Figure 2.5](#). For example when creating a model for a nova, options might include:

*“cosmic ray background
element limit off -8
age 8114 days”*

- **Abundances:** Opens a new window allowing the user to type/paste abundances to be used as input to the model. Examples of abundances can be found by clicking **Reference | Abundance Examples** in the menu bar.
- **Emissions:** Opens a new window allowing the user to type/paste emissions to be used as input to the model. Emissions must be added in a particular format of no more than 10 characters. To ensure that emissions are entered correctly, PYCROSS has an extensive library of emission lines that is available by clicking **Reference | Emission Line Index** on the menu bar.
- **Open Archive Folder:** Opens a new Finder/Explorer window where all PYCROSS data is stored.
- **Run PYCROSS - New SHAPE Model:** This button is clicked to run a new model; the user must first have selected a SHAPE data cube and entered

all necessary CLOUDY options.

- **Run PYCROSS - Archive SHAPE Model:** If users create a model and are not satisfied with the outcome or feel that certain parameters need to be changed then they can modify specific CLOUDY options outlined above. By clicking this button and selecting an archived model, users can run the model again with updated parameters. This feature saves a lot of time as it does not require the user to start anew.
- **Plot Current Model:** Open the plotting GUI to plot the current PYCROSS model. Any emissions entered will automatically be loaded into the plotting options window.
- **Plot Archive Model:** Select a zipped archived model then open the plotting GUI and proceed to plot. This again saves time not having to create a model from the start, while also offering the user the choice of building a database of models to plot from.

An ‘emission’ as discussed here is a simulated narrow-band image at the wavelength of a specific spectral emission line. Users can plot from one to a maximum of six emissions (plotted in flux units ergs s^{-1}) in a single plot at a time, by highlighting desired emission, and adding them to the “*Selected Emissions*” list. This is to ensure that the quality of models are not diminished and structures within the models are resolvable. Once selected, a plotting grid can be adapted to fit the required number of emissions. The number of angles, inclination and labels for x-axis and y-axis are set prior to plotting. Corresponding emission lines will also be displayed at the top of each plot regardless of the number of plots/subplots, the effective temperature of the ionising source is located in the colour-bar to the right of each model. Users can view a plot ‘cut’ of $\text{N}^+/\text{O}^+/\text{N}/\text{O}$, which is automatically generated. These weighted plots are adapted from the tutorial for PYCLOUDY (Morisset, 2013), and show the ionised fraction versus neutral fraction for the two most commonly studied astrophysical metals, i.e. O and N. Selection of the cuts is performed by first selecting an element, then its ionising

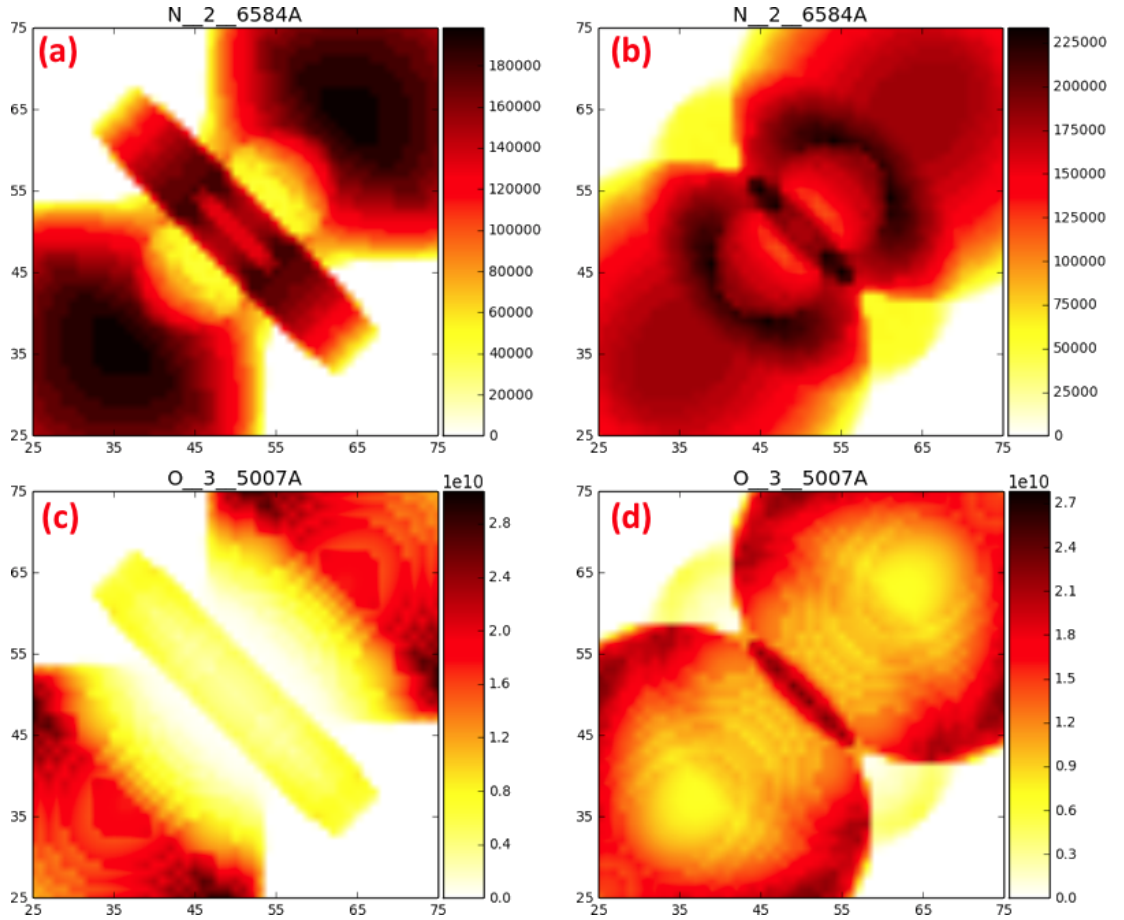


Figure 2.8: Photoionisation models of [N II] 6584Å (a, b) and [O III] 5007Å (c, d) derived from the theoretical model in Figure 2.5. Each emission plot initially plotted at an inclination angle of 90° (a, c) then at 50° (b, d). Colour-bars correspond to the effective temperature of the ionising source, flux units in ergs s⁻¹. Plots are zoomed to better visualise features like the torus across different emissions and angles. The colour map used was hot_r.

state; a maximum of three cuts is allowed per plot. Users may open the plotting folder directly from this GUI and automatically archive all plots generated in that session. This is achieved by selecting the *Auto Archive* checkbox; archive plots are saved using the name and time-stamp of creation similar to saving of newly generated models discussed earlier.

The latest version of PYCROSS includes the functionality that gives users the ability to plot in 71 different colour maps and magnify the centre regions of nebulae, allowing to better visualise regions and/or possible hidden features, see Figure 2.7 and Figure 2.8. On analysis of Figure 2.7, the outer regions of the lobes are more clearly defined in (a) than (b) or (c) where the following colour maps

were applied: (a) `nipy_spectral_r`, (b) `gist_stern_r` and (c) `gist_heat_r`¹⁷. Colour maps may be misleading, for example differences of regions within the outer lobes of (a) and (b) in [Figure 2.7](#) are greatly exaggerated as compared to that in (c) which is more realistic. Offering this feature allows users to find a trade off for investigating features of nebulae.

The axes on all plots are normalised distance units (0–100), the colour-bar corresponds to the effective temperature of the ionising source, flux units in ergs s^{-1} . Users can add additional text to the axis labels via the Plotting Options GUI, see [Figure 2.5](#). Mathematical notation can also be written for the plot axis labels when using a subset TeX¹⁸ markup by placing text inside a pair of dollar signs (\$).

2.5 Summary and conclusion

In this chapter various modelling techniques, codes and steep learning curves encountered when installing, understanding and utilising specialist photoionisation codes and modelling software were discussed. The need for astronomers to develop/code software for specific tasks is becoming a necessity especially with current advances in hardware, software and volume of data acquisition. As such it is important to employ and adhere to a SDLC when developing software applications for astronomy to help guarantee milestones, have greater control over complex projects and most importantly to ensure reliability and quality in use. Advantages of identifying a suitable SDLC approach has been discussed and employed in the development of PYCROSS ([Fitzgerald *et al.*, 2019, 2020](#)).

The Agile SDLC approach used to develop and test PYCROSS is described in detail. User stories are used to break more complicated coding tasks into smaller more manageable ones; the complexity of the code is also represented with descriptions of functionality within each class ([Table 2.3](#)) and their relationships to

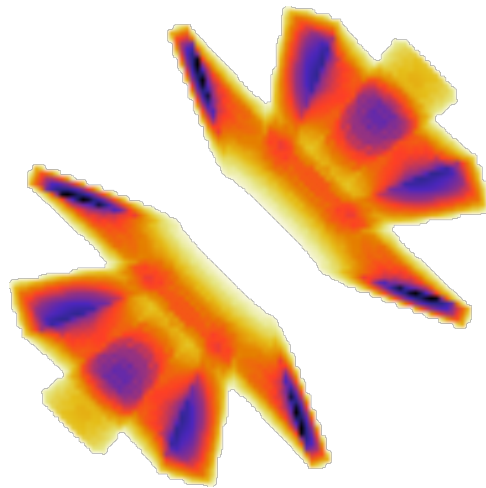
¹⁷The `r` signifies that this particular colour map has been revised in matplotlib: https://matplotlib.org/3.1.1/gallery/color/colormap_reference.html

¹⁸Refer to: <https://matplotlib.org/3.1.1/tutorials/text/mathtext.html>

each other (Figure 2.3). A detailed account of PYCROSS installation, functionality, user interface and operational overview is given using a theoretical model generated in SHAPE. The directory structure and layout of PYCROSS has been designed to allow for intuitive usability while also providing automated features allowing the user to be more productive and reduce the steep learning curves traditionally associated with new astronomical/astrophysics software. A scientific overview and demonstrations of numerous PYCROSS models generated from various targets will be discussed in the next chapter.

Chapter 3

PYCross pipeline for novae & planetary nebulae



3.1 Introduction

In the last chapter various astronomy modelling software packages were discussed, programming paradigms, SDLC and their importance in developing software was outlined. The development, installation, functionality and operational overview of PYCROSS were discussed in detail. This chapter demonstrates various scientific methods/pipelines that can be used with PYCROSS to generate photoionisation models of novae V5668 Sagittarii (2015), V4362 Sagittarii (PTB 42) and PN LoTr 1.

As the development of PYCROSS is iterative, feedback from testers, users and reviewers during the preparation and publication of these pieces of research were noted and where possible incorporated into the next iteration of the code which will be discussed in the next chapter. Feedback consisted of comments and recommendations regarding the application’s usability, functionality and errors encountered. Results from this chapter have been published in [Harvey *et al.* \(2018\)](#); [Harvey *et al.* \(2020\)](#); [Fitzgerald *et al.* \(2020\)](#), refer to [Table 3.1](#) for a summary of each case study.

<i>Target (Model published in)</i>	<i>Software development & findings</i>
Nova V5668 Sagittarii (Harvey <i>et al.</i>, 2018)	Model developed by Dr Eamonn Harvey who utilised a command line prototype version of the code. Using acquired spectroscopy a SHAPE model was constructed to realise multiple emission models even though the target itself was not full resolvable.
PN LoTr 1 (Fitzgerald <i>et al.</i>, 2020)	Model developed by postgraduate student Nicola Keaveney. Miss Keaveney also assessed the interface for usability, providing feedback on any issues encountered. Miss Keaveney’s models was the first PN to be modelled by PYCROSS.
Nova V4362 Sagittarii (Harvey <i>et al.</i>, 2020)	Model developed by Dr Eamonn Harvey. Dr Harvey has adapted PYCROSS to all of his most recent publications and is the longest user of the code. In this instance, photoionisation models were used to support findings that this particular nova was oxygen flaring and not nitrogen flaring as previously thought.

Table 3.1: PYCROSS case studies: development and findings. Models were chosen based on the research users were carrying out at that time. Development of the code was ongoing prior to, during and post release of these publications. Users listed developed models while also acting as interface testers, providing feedback regarding issues they encountered during the creation of their models. This information was used to resolve any issues and/or adding to new user stories for the next iteration.

3.2 Modelling nova remnants

Novae are the result of an eruption on the surface of a white dwarf in a close binary system. The white dwarf's counterpart is normally a red dwarf or sub-giant, which has overfilled its Roche lobe and thus loses mass through an accretion stream onto the white dwarf surface. Pressure at the white dwarf-accreted envelope interface increases due to a buildup of hydrogen-rich material, eventually resulting in thermonuclear runaway. This subsequent eruption reaches luminosities $\gtrsim 10^4 L_{\odot}$, and ejects a mixture of material. A combination of that processed in the thermonuclear runaway, material dredged up from the white dwarf and the previously accreted outer layers of its companion. The ejected material reaches velocities of order 10^3 – 10^5 km s $^{-1}$. Emission line profiles indicate considerable spatial density and velocity structure. Immediately after a nova eruption the ejected material is dense, bright and optically thick. This soon fades after revealing H I and He I emission lines. Over time [O III], [N II] and [Ne III] become stronger relative to the fading continuum (Williams, 2012). Over a few years the ejecta will be observed as a fading, constant-velocity expanding nebulous shell surrounding the post-nova star. These eruptions are not destructive enough to change either star and generally they return to their quiescent state, on decadal timescales. Classical novae repeat the process every $\sim 10^4$ – 10^5 yr (Osterbrock & Ferland, 2006). Although, a recurrent nova population also exists, with observed recurrence periods on human timescales. Shorter rates of recurrence are related to heightened accretion rates onto higher mass white dwarfs (Priyalnik & Kovetz, 1995; Yaron *et al.*, 2005; Shara *et al.*, 2010). The material ejected from the white dwarf surface generally forms an axisymmetric shell of gas and dust around the system. These 3D shell structures are difficult to untangle as viewed on the plane of the sky without additional velocity information.

While spectroscopic data can be used to yield approximate values for temperature, velocity, and density along the line of sight of the object, a photoionisation model is required to determine the chemical structure of a nebula (Bohigas, 2008). As discussed in Harvey *et al.* (2018), photoionisation modelling of ejected nova

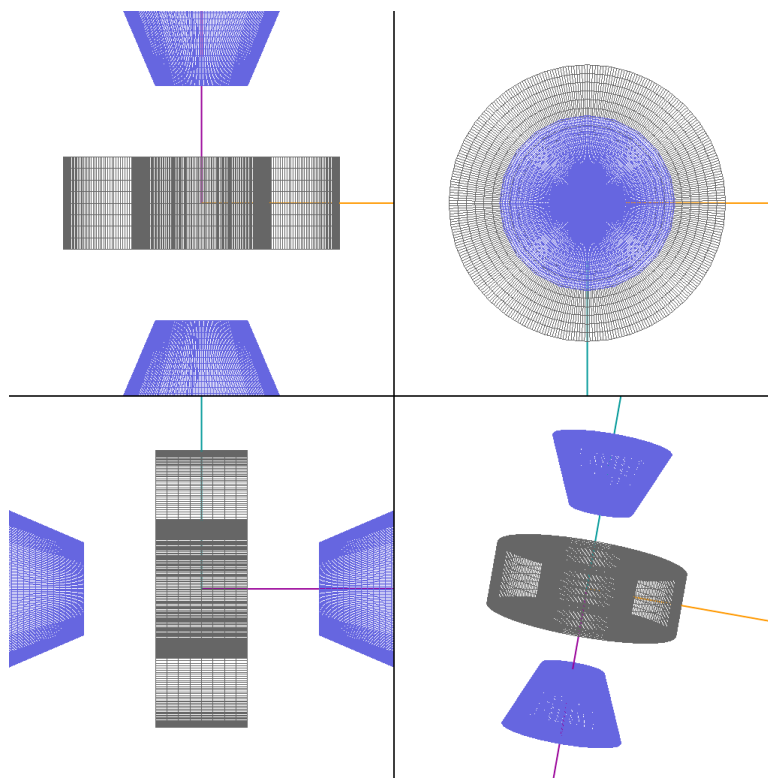


Figure 3.1: SHAPE model for V5668 Sgr. Figure adapted from [Harvey *et al.* \(2018\)](#)

shells during their nebular stage of evolution can contribute to estimates of the total mass and abundances of heavy elements ejected during nova events ([Helton *et al.*, 2011](#)). Examples of the ability to realise photoionisation models of novae, more specifically V5668 Sgr and V4362 Sgr, created by the PYCROSS pipelines, are outlined in [subsection 3.2.1](#) and [subsection 3.2.2](#).

3.2.1 V5668 Sagittarii (2015)

[Harvey *et al.* \(2018\)](#) investigated V5668 Sgr (2015), a slow-evolving extremely bright nova on the surface of a CO white dwarf. The nova event produced dust ([Gehrz *et al.*, 2018](#)), and was classified to be of the DQ Her-type¹⁹. The V5668 Sgr nova event holds the record for longest sustained gamma ray emission from such an event ([Siegert *et al.*, 2018](#)).

¹⁹Archetype for rich dust-forming slow novae, and historically significant following a major observed eruption in 1934, one of the first novae to be analysed with high-cadence spectroscopy observations where results were later used to classify nova spectra into 10/11 subclasses by [McLaughlin \(1942\)](#)

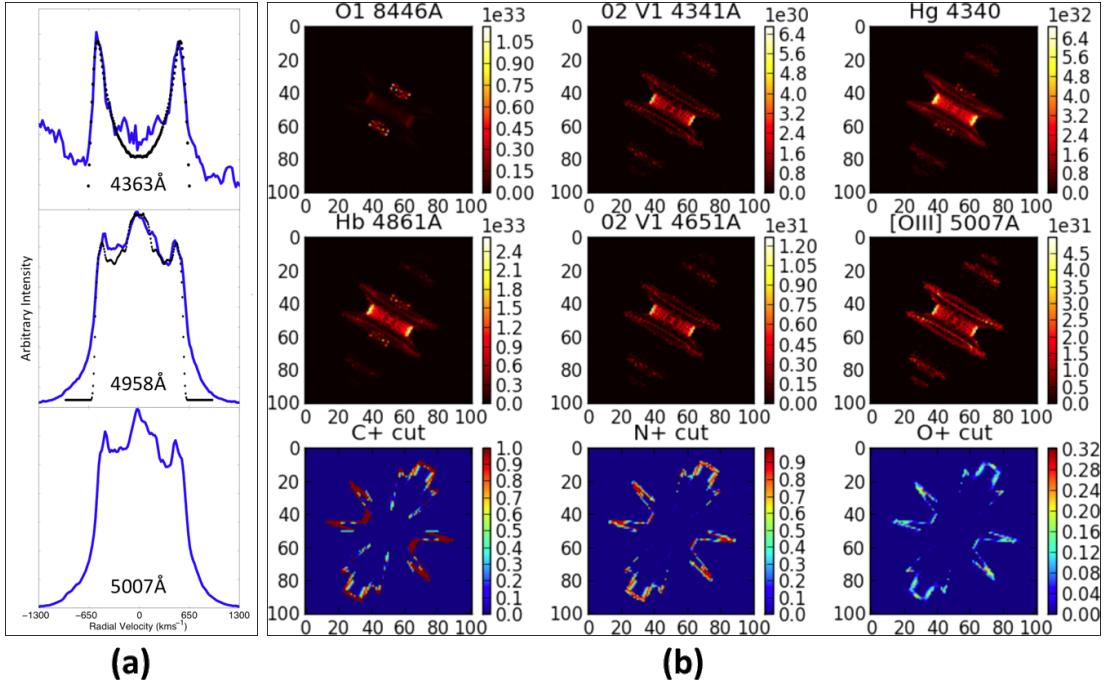


Figure 3.2: (a) Spectral line profile simulations of [O III] nebular and auroral lines of V5668 Sgr on day 822 post discovery. The blue-solid lines represent observed line profiles and were used in the fitting of a morpho-kinematical model with the SHAPE software, represented by overlaid black dots. The auroral line is fitted with an equatorial disk whereas the nebular lines fit an equatorial waist and polar cones morphology with a Hubble outflow velocity law. (b) PYCROSS emission models of V5668 Sgr, using nova abundances with the inclination angle set at 85° . Clumpiness was simulated using a Perlin noise modifier in SHAPE. The geometry used for this model is illustrated in Figure 3.1. Figure adapted from Harvey *et al.* (2018), O II 4341 Å was shown to demonstrate that the line emission is expected to arise from the same geometrical location and so to deblend it with 4340 Å the same line profile shape would be assumed. With regards the two nebular [O III] lines they were shown in Harvey *et al.* (2018) to show the consistency in the line shape as would be expected from 4959 Å and 5007 Å [O III] and how different the auroral [O III] line shape was. Colour-bars corresponds to the effective temperature of the ionising source, flux units in ergs s^{-1} . PYCROSS scientific pipeline is illustrated in Figure 3.3

A goal of the research carried out by Harvey *et al.* (2018), was to better understand the early evolution of classical nova shells in the context of the relationship between polarisation, photometry, and spectroscopy in the optical regime. Observations over five nights with the Dipol-2 instrument mounted on the William Herschel telescope (WHT) and the Royal Swedish Academy of Sciences (KVA) stellar telescope La Palma, yielded polarimetric data directly following the nova’s dust formation episode. In this study PYCROSS was used to model and visualise the ionisation structure of V5568 Sgr even though this nova shell was not yet resolvable with medium sized ground-based telescopes. The polarimetric and

spectroscopic data revealed conditions present in the expanding nova shell allowing for the creation of a SHAPE model. The proposed geometry consisted of an equatorial waist and polar cones, see [Figure 3.1](#).

Initial models consisted of broad parameter sweeps that were refined using PYCLOUDY ([Morisset, 2013](#)). This allowed examination of emission line ratios for the hot–dense–thick nova shell under study. A cylindrical primitive was used to construct the equatorial waist, where a density, thickness and Hubble velocity law were applied. The polar features were constructed using cone primitives. In this instance densities applied were estimations from CLOUDY simulations and velocity components were derived from measuring Doppler broadened characteristics of observed emission lines. Emission lines in fast outflows of unresolved structures are governed by their velocity field and orientation towards the observer. Analysis techniques available in SHAPE allow users to disentangle projection effects. The line shapes modelled in [Figure 3.2 \(a\)](#) are displayed at an inclination of 85° , a polar velocity of 940 km s^{-1} and an equatorial velocity of 640 km s^{-1} at their maximum extensions.

PYXCROSS emission models of V5668 Sgr, were created using optimum values derived from CLOUDY/PYCLOUDY parameter sweeps. The average number density was found to be $\sim 1.0 \times 10^9 \text{ cm}^{-3}$, luminosity and effective temperature were set to $\log(L_\odot) = 4.36$ and $1.8 \times 10^5 \text{ K}$ respectively. To recreate the nova conditions on day 141 post discovery an inner and an outer radius were set to $3.2 \times 10^{14} \text{ cm}$ and $6.4 \times 10^{14} \text{ cm}$, respectively. [Figure 3.2 \(b\)](#) illustrates the PYXCROSS emission models for V5568 Sgr, where a comparison of the locality of emission through the shell of the same species is presented in each column of three panels. These models show the ionic cuts for C, N and O, respectively. An ionic cut is a slice of the ionised structure for a specific ionisation state of a species. [Figure 3.2](#) presents the first state of ionisation for C, N and O. The colour-bar shows the ionised fraction for different geometrical locations of the appropriate ionisation state.

[Harvey *et al.* \(2018\)](#) revealed variability in polarisation suggesting internal

shocks in the nova outflow, supported by the presence of gamma-ray emission (Siegert *et al.*, 2018). The position angle of this nova was determined using the polarimetry observations. Spectroscopy allowed for derivation of the physical conditions, including outflow velocity and structure, nebular density, temperature and ionisation conditions. Photoionisation models generated from PYCROSS gave further insight into the nova system as a whole. Harvey *et al.* (2018) concluded that slow novae are regularly referred to “nitrogen flaring”, however based on their findings suggest that they are in fact more likely “oxygen flaring”.

3.2.2 V4362 Sagittarii (PTB 42)

More recently (Harvey *et al.*, 2020), utilised the current version of PYCROSS to aid in uncovering a previously undiscovered classical nova shell surrounding the nova system PTB 42 of the DQ Her type. Imaging was acquired from the Aristarchos telescope in Greece and consisted of two narrow-band filters; $H\alpha + [NII]$ ($6578\text{\AA}/40\text{\AA}$)²⁰ and $[OIII]$ ($5011\text{\AA}/30\text{\AA}$) with exposures of 30 - 40 minutes in each filter. High-resolution spectroscopic data was obtained using the Manchester Echelle Spectrograph (MES) instrument mounted on the 2.1 m telescope at the San Pedro Mártir (SPM) observatory, Mexico. The PTB 42 nova shell, was detected using the low-resolution, high-throughput SPRAT spectrograph on the Liverpool Telescope during August of 2016.

The PYCROSS pipeline (see Figure 3.3) was then used to generate emission models based on imaging and spectroscopic observations. Figure 3.3 is split into three main sections (1-3), 1 represents observational data used to derive the spatial structure of an emission nebula, 1(a) is narrow-band imaging used to inform the extent and axial ratio of the nebula. 1(b) is low-resolution spectroscopy, used to derive density, abundances and ionisation conditions. 1(c) is high-resolution spectroscopy used to derive the velocity information for individual spectral lines. 2(a) is a suitable SHAPE geometry, seen in full in panels A and B, but arranged in

²⁰The first number represents the centre wavelength and second number represents the filter width in Angstroms

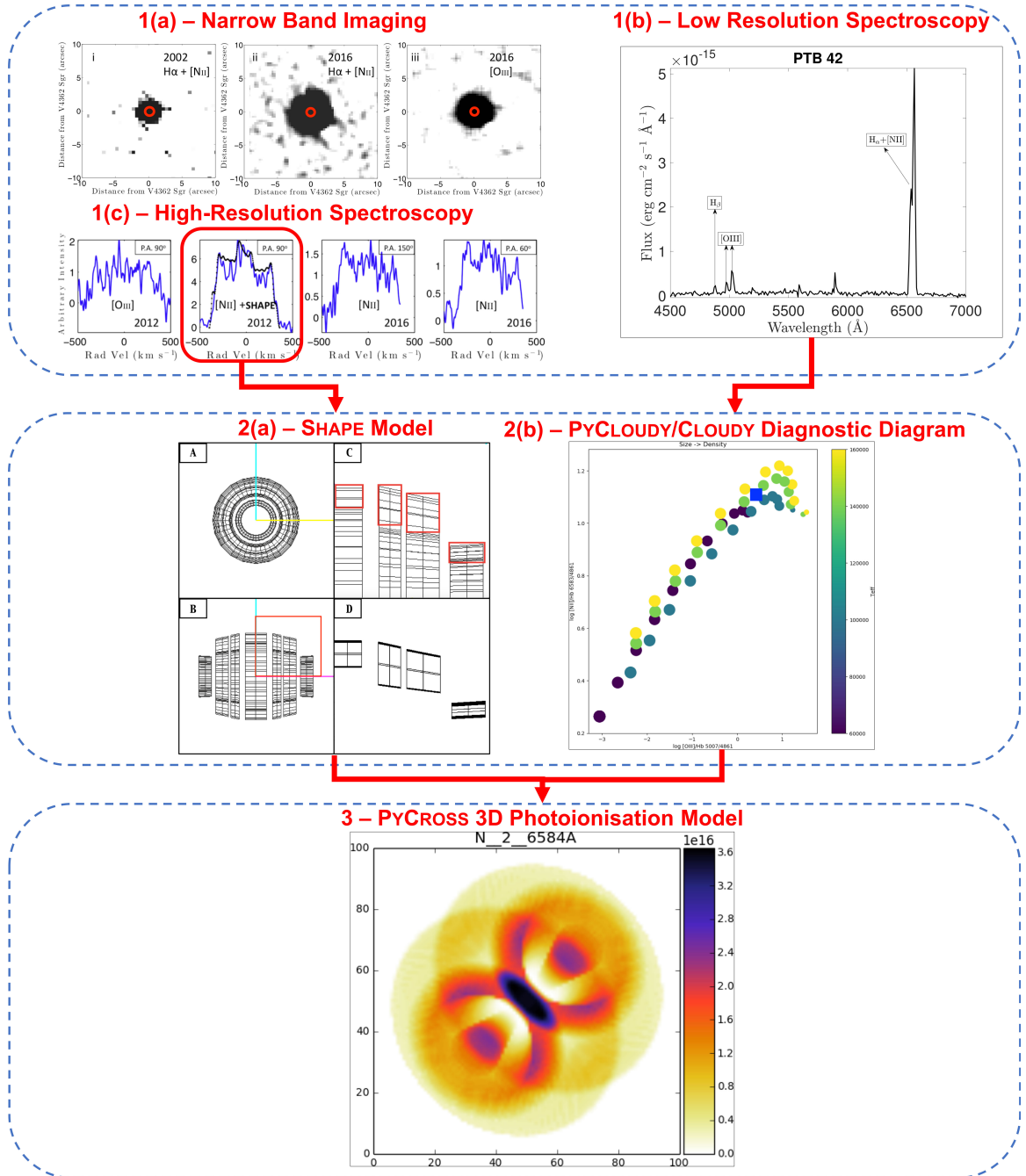


Figure 3.3: PYCROSS Scientific Pipeline for V4362 Sgr / PTB 42(1994).

panel D in a position to be output to a text file readable by PYCROSS, see section 2.4.2 and Harvey *et al.* (2020). 2(b) is a diagnostic diagram generated to interpret the emission line ratios measured from broadband low-resolution spectra. 3 is the final output PYCROSS model generated from applying the geometry and density at each geometrical point (i.e. from the SHAPE output text file). Other parameters such as the stellar luminosity, stellar effective temperature, and abundances are input to PYCROSS's GUI. A set of 1D Cloudy simulations are run through the 2D parameter space which are then wrapped in azimuth around the complete shell creating a pseudo 3D model for any observable emission line, here we show the [NII] 6584Å at a position angle of 60°. Colour-bars in 3 correspond to the effective temperature of the ionising source, flux units in ergs s^{-1} , the colour-bar in the PYCLOUDY diagnostic diagram, 2(b), is the effective temperature of the ionisation source, figure adapted from (Harvey *et al.*, 2020). Based on these observations, and PYCLOUDY simulations, the nova shell was reproduced in SHAPE and then passed to PYCROSS.

The P.A. for this target was chosen based on polarimetric observations presented in Evans *et al.* (2002), in addition to close examination of the major and minor axes in the narrow-band imaging (top left of Figure 3.3). High-resolution spectroscopy from MES was used to find the radial velocity of individual components within the nova shell. Difficult to derive parameters are the system inclination, covering and filling factors of the nova shell, as well as the opening angle of the polar cones.

In this study a number of morpho-kinematic SHAPE models were created to determine the best-fit relationship between image, PV array and 1D line spectrum to commonly proposed nova shells morphologies. While spatial information could not be resolved, structures within the nova could be resolved via line-of-sight velocities. The observed equatorial velocity is 350 km s^{-1} , as measured from the MES spectra. An axial ratio of 1.4 and polar velocity of 490 km s^{-1} was initially chosen based on the inclination corrected axial ratio for similar novae DQ Her and T Aur (Bode & Evans, 2008). Adjusting for inclination when fitting to the line

profile gives an equatorial velocity of 390 km s^{-1} and polar velocity of 550 km s^{-1} . This allowed for the remaining velocities to be set to $550 \times r/r_0$ (km s^{-1}). The observed [N II] line profile, taken from the 2012 observation (seen encircled in red at the top left of [Figure 3.3](#), was chosen for modelling the nova shell structure as it had the highest S/N.

The luminosity of the system was estimated based on that of the class archetype, namely DQ Her, during quiescence [Ferland *et al.* \(1984\)](#). The inner and outer radii of the shell are estimated based on the observed expansion velocity distribution and narrow-band imaging and shell age, although the actual shell thickness is difficult to know without resolving it spatially. Abundances used were for that of the archetypical slow nova, DQ Her ([Ferland *et al.*, 1984](#)).

In this work PYCROSS was employed to better understand observed ionised nebula structure by using broadband spectra from which line ratios are measured. A grid of models was generated to determine the best fitting model parameters which were then applied through the derived geometry. This geometry is determined from matching line profiles in high-resolution spectra and narrow-band imaging in SHAPE. Polarimetry and imaging was used to determine the position angle of the shell. Using abundances adapted from the DQ Her nova shell model of [Ferland *et al.* \(1984\)](#) PYCROSS generated a pseudo 3D simulation of the ionisation structure of PTB 42 as seen in top centre of [Figure 3.3](#). Results show the difference in emission regions for the strongest nebular lines, i.e. [N II] and [O III]. The PYCROSS model presented in [Harvey *et al.* \(2020\)](#) detailed observed components i.e. equatorial ring, higher latitude rings and polar features of the nova, allowing their individual behaviour to be examined.

3.3 Modelling PNe

Post-main sequence low to intermediate mass stars ($\sim 0.8 M_{\odot} - 8 M_{\odot}$) will over time evolve to become PNe as the outer layers of the star are ejected through thermal pulses after the AGB phase. This exposes hotter layers that can ionise

the previous ejected material. A detailed description of the evolutionary track and mechanics a star undergoes on its journey to become a PN at each phase is presented in Prialnik (2009) and see also (Herwig, 2005).

There are complications to this simple picture, particularly in the role of binarity and the possibility of ‘mimics’ such as symbiotic systems (Boffin & Jones, 2019). As a result, there is no universal observational definition for PNe, but their existence is usually dependent on two components: a circumstellar shell of sufficient mass and density to be detectable, and a hot central star to ionise it. PNe candidates are usually discovered by objective-prism surveys or by direct imaging in a narrow spectral region around a strong emission line or line such as [O III] 4959Å, 5007Å or H α and [N II] 6548Å, 6583Å (Osterbrock & Ferland, 2006). Their expanding shell sizes (~ 0.2 pc) and expansion velocities (~ 25 km s $^{-1}$) imply a dynamical lifetime of $\sim 10^4$ yr (Kwok, 2000).

As intermediate mass stars make up a large portion of the stellar mass in our galaxy, studying how their nuclear-processed interiors are ejected into intricate nebulae and eventually into the interstellar medium, can lead to a deeper understanding of the galaxy’s chemical evolution. PNe spectra are rich in emission lines, including the interesting *forbidden lines*, and serve as a laboratory for the physics and chemistry of photoionisation. Modelling the 3D spatiokinematic structure, along with the 3D photoionisation of PNe and their mimics can contribute to understanding how these spectacular nebulae are formed.

3.3.1 Planetary nebula LoTr 1

The previous section described PYCROSS and its use in modelling and investigating novae emissions. In this subsection, and for the first time, PYCROSS will be used in modelling emissions for LoTr 1, a PN believed to contain a binary central star system consisting of a KL-type III giant and white dwarf, first discovered by Longmore & Tritton (1980).

Tyndall *et al.* (2013) published imaging and spectroscopy from long-slit Echelle spectroscopy acquired using the Anglo-Australian Telescope/University College

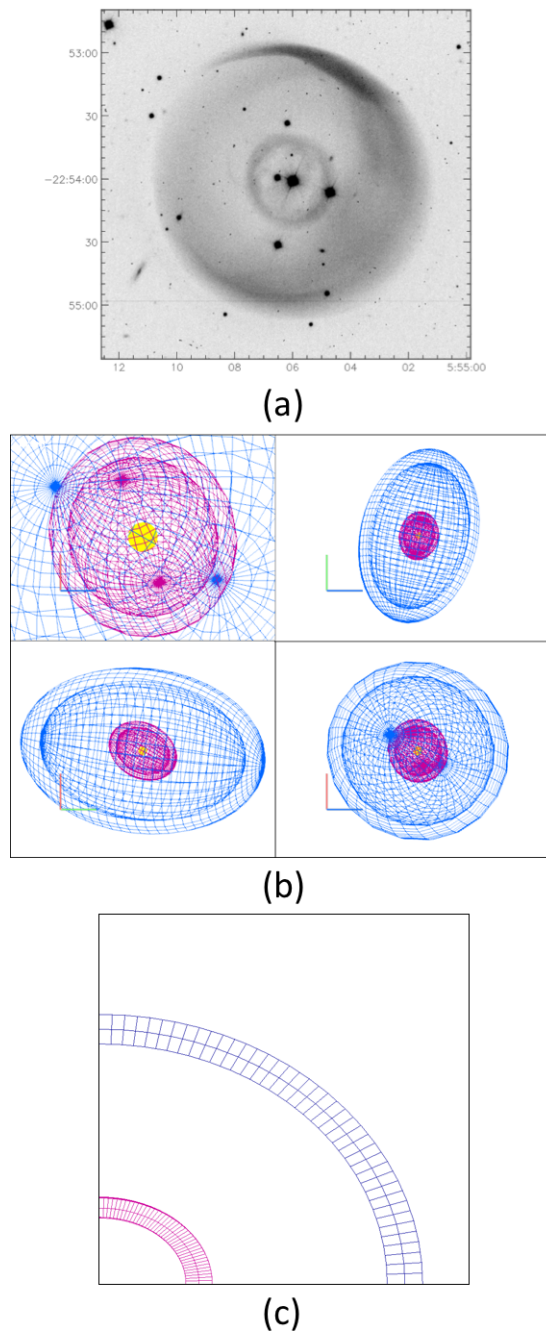


Figure 3.4: (a) Deep, narrowband images of PN LoTr 1, in $[\text{O III}] 5007\text{\AA}$. North is to the top of the image, East is to the left. Image acquired using European Southern Observatory (ESO) Multi-Mode Instrument (EMMI), mounted on the 3.6m New Technology Telescope (NTT) of La Silla Observatory. The outer shell appears brighter in both the northeast and southeast directions of the image, which could suggest the possibility of an inclined, elongated structure due to the projection effect. *Image credit and* © Tyndall *et al.* (2013). (b) 3D SHAPE model of LoTr1 from different views. The view in the bottom right quadrant of (b) represents the nebula as in (a). (c) SHAPE quadrant slit of LoTr 1 where shells have been aligned. The resulting data cube is then passed to PYCROSS.

	Radius (cm)	Expansion Velocity (km/s)	Morphology	Kinematical Age (yrs)
Outer Shell	2.84×10^{16}	25 ± 4	Elliptical	$35,000 \pm 7,000$
Inner Shell	9.14×10^{15}	17 ± 4	Elliptical	$17,000 \pm 5,500$

Table 3.2: Table of parameters for both inner and outer shells of LoTr 1 from Tyndall *et al.* (2013).

London Echelle Spectrograph (AATUCLES) and the New Technology Telescope-ESO Multi-Mode Instrument (NTT-EMMI) focused on the [O III] 5007Å emissions over eight different slit positions. Analysis revealed a double-shelled structure with evidence of an elliptical and slightly inclined outer shell, with an inner shell consisting of a similar morphology at a different orientation. Careful measuring of axes and relative sizes yielded a model constructed of two elongated shells with inner and outer shell radii of 5'' and 12'' respectively. Each shell is at different inclinations, with an angle of 50° difference in position angle, and a difference of 57° inclination (see Figure 3.4 (a)). A new SHAPE model was created based on this data. Both inner and outer shells were create using sphere primitives with modifiers applied to elongate the inner and outer shells along the z-axis by a factor of 1.3 and 1.5 respectively.

A comparison of the first slit acquired by Tyndall *et al.* (2013) compared to that recreated in SHAPE can be seen in Figure 3.5. The observed slit position is in the left hand panel and the right panel shows the theoretical PV array. The systemic velocity, V_{sys} of the central shell was determined to be 14 ± 4 km/s (Tyndall *et al.*, 2013), for the observations, which result from the velocity axis of this data being relative to the V_{sys} . An important similarity correspond to the major axis in that it has the same length as the diameter of the inner shell. This contributes to the assumption that it is a closed, isolated structure rather than a bipolar nebula. A bipolar nebular structure viewed from above would not give this regular shape. These ellipses seen along the velocity axis appear symmetric in both images, in agreement with a spherical shell or elongated ovoids.

Minor modifications were made to align the shells of LoTr1 prior to creating a data cube slice in order to create a photoionisation model using PYCROSS

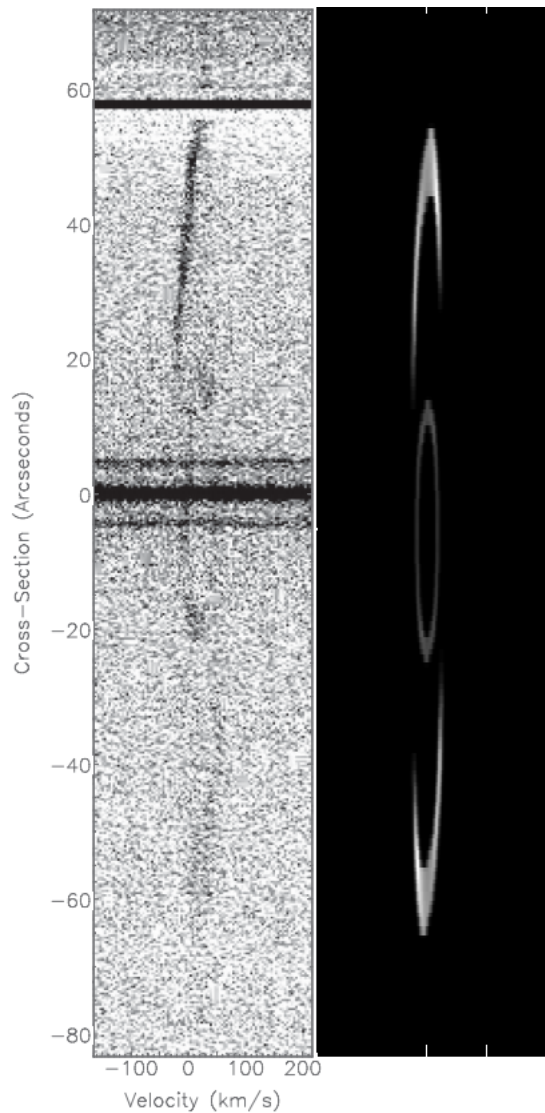


Figure 3.5: Left: Recreation of slit position 1 acquired by Tyndall *et al.* (2013). Right: Theoretical PV diagram created in SHAPE. West is up.

(Figure 3.4 (b)). This is done to ensure that the model is completely axisymmetric in order for it to work with PYCROSS; PYCROSS does not currently have the capacity to generate fully 3D photoionisation models. Default PN abundances were used from Aller & Czyzak (1983) and Khromov (1989), with high depletions for elements not listed. Emission models generated from PYCROSS for LoTr 1 can be seen in Figure 3.7. These models are set at an inclination angle of 40° , with a blackbody effective temperature of $\sim 100,000$ K (Gruendl *et al.*, 2001) and a luminosity of $100 L_\odot$ (Henry *et al.*, 1999). These parameters were chosen as they were ascertained from the Helix nebula (NGC 7293), one of the closest and

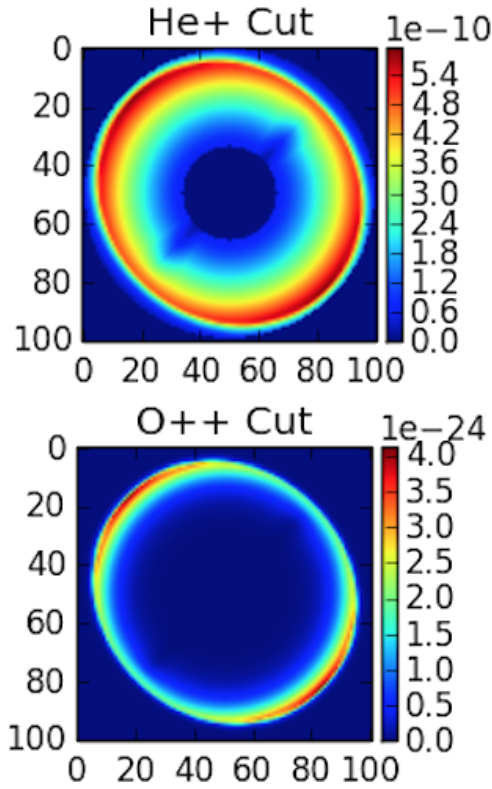


Figure 3.6: LoTr 1 PYCROSS photoionisation cuts of He^+ and O^{++} , using PN abundances with the inclination angle set at 40° . Colour-bars correspond to the effective temperature of the ionising source, flux units in ergs s^{-1} .

brightest PN (Hora *et al.*, 2006). While a hot black body spectrum is used for the modelling here, it is possible to use more complex central star spectra such as, for example, WR-type spectra, as applicable to HB4 (Derlopa *et al.*, 2019) and generally found in around 10% of PNe (DePew *et al.*, 2011). Figure 3.6 shows ionic cuts of He^+ and O^{++} , top and bottom respectively, at an inclination angle of 90° for the top figure, and 40° for the bottom figure. It is worth noting that the object appears entirely spherical at 90° because this angle shows a cut through the object head on. Similar observations were made by Tyndall *et al.* (2013) who reported clear asymmetry in the nebular structure, additionally but it is close to a head on view.

In this scenario and for simplicity, attention is limited to two elements: oxygen and helium. While diffuse nebulae contain vast quantities of material, they have relatively low densities (approximately 10^3 particles cm^{-3}). They are rich with emission lines such as Balmer lines of hydrogen, as well as those which arise from

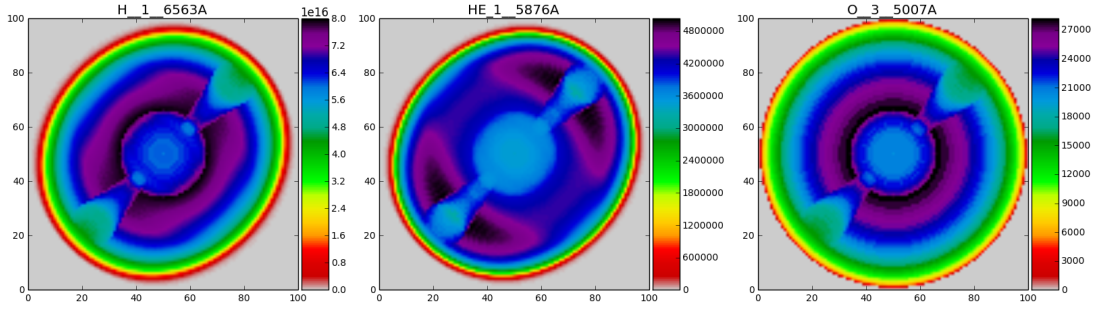


Figure 3.7: LoTr 1 PYCROSS photoionisation model using PN abundances with the inclination angle set at 40° . The input SHAPE model is seen in Figure 3.4 with changes made to the inclination angles of the two shells to make the entire object symmetrical. Colour-bars correspond to the effective temperature of the ionising source, flux units in ergs s^{-1} .

the transitions between energy levels which result in ions such as O^+ , O^{++} , N^+ , etc. As the lifetime of ionised hydrogen is very short (fractions of a microsecond due to the fast nature of electric dipole transitions), the probability of excited hydrogen is negligible, so any hydrogen can be assumed to be in its ground state for the purpose of ionisation rate calculations.

Figure 3.6 compares O^{++} and He^+ in this model for LoTr 1 showing predicted emissions maps of this PN in spectral lines other than those observed, to be compared with future observations. The stellar spectrum and nebular analysis could be developed further from this starting point based on more information regarding the central star. This would require a more extensive data-set for further investigation into the morphology of LoTr 1 in order to confirm its true structure and inclination. A data-set with a higher signal-to-noise ratio would be necessary to resolve the very faint outer shell.

Oxygen is a particularly useful ion in analysing the physical structure of a nebula. The well known $[\text{O III}]$ 5007\AA optical line strongly contributes to nebula cooling, while more highly ionised O VI lines can radiate in at higher energies in hotter parts of the nebula. Where ionised hydrogen is found, we expect to find ionised oxygen as the first ionisation potential of oxygen is almost identical to that of hydrogen. The difference between the two however, is that oxygen can be ionised more than once (Dyson & Williams, 1997).

3.4 Summary and conclusion

To summarise, this chapter has described how early versions, and the first release of PYCROSS were employed in researching and modelling novae V5668 Sagittarii (2015) (Harvey *et al.*, 2018), V4362 Sagittarii (PTB 42) (Harvey *et al.*, 2020) and PN LoTr 1 (Fitzgerald *et al.*, 2020). In each scenario new photoionisation models (created using PYCROSS) for various emissions have been created, an operational overview and scientific pipelines were discussed.

Harvey *et al.* (2018) used PYCROSS in conjunction with other codes and techniques to better understand the early evolution of classical nova shells by modelling and visualising the ionisation structure of nova V5668. PYCLOUDY was used to examine emission line ratios by refining parameters acquired from a pool derived from a broad parameter of literature and data acquired from observations. The resulting new PYCROSS photoionisation models gave further insight into the nova system as a whole, and using the acquired spectroscopy, the authors were able to visualise multiple emission models even though the target itself was not full resolvable.

Harvey *et al.* (2020) acquired high-resolution spectroscopy from MES to find the radial velocity of individual components within the shell and created a number of morpho-kinematic SHAPE models to determine best-fit relationships between image, PV arrays and 1D line spectrum. PYCROSS models generated in this study detailed observed components such as the equatorial and higher latitude rings, as well as polar features. The PYCROSS photoionisation models were used to support findings that this particular nova was oxygen flaring and not nitrogen flaring as previously thought.

In Fitzgerald *et al.* (2020), and for the first time, PYCROSS was applied to a PN, namely LoTr 1. Long-slit Echelle spectroscopy over eight different slit positions focusing on the [O III] 5007Å emission line was used to create a 3D morpho-kinematic SHAPE model. Densities, velocities and inner and outer shell radii measurements were incorporated into the model which was then compared against the PV arrays acquired from previous published observational data. A

sweep of published literature yielded luminosity, black body temperatures and abundances were used as CLOUDY inputs into PYCROSS.

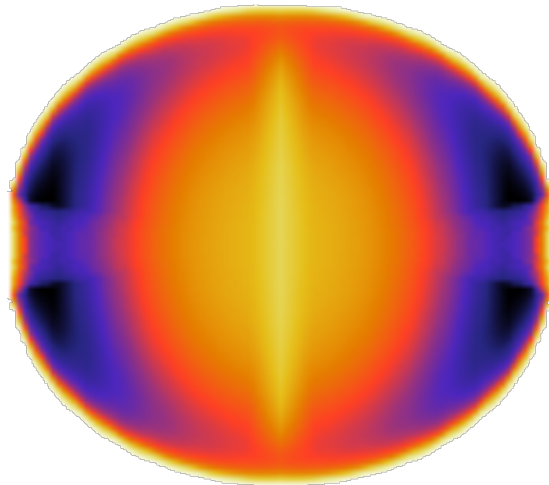
Feedback from testers, users and reviewers regarding the applications usability, functionality and errors encountered during the preparation and publication of these pieces of research were noted and where possible incorporated into the next iteration of the SDL. Examples included:

- Modifications to the interface to improve usability.
- Automatically saving new models
- Creation of a log file to track parameters entered/changed during a PYCROSS session
- Limiting the amount of models to be plotted at a single time to improve resolution.
- Providing automated feedback if a user entered data in error.
- Having online references available for checking emission lines.
- Being able to plot an archived/previously generated model.

In all cases, spectroscopic and observational data was used to create a 3D SHAPE model. Additional CLOUDY parameters were derived from acquired spectra or extrapolated from published literature as inputs into PYCROSS facilitating researchers with a tool to better understand observed ionised nebula structures.

Chapter 4

Photoionisation modelling of the Etched Hourglass Nebula – MyCn 18



4.1 Introduction

The first release of PYCROSS, (Fitzgerald *et al.*, 2020), and models therein, was developed using Python 2.7 for CLOUDY 13 (C13) and was only available for MAC OS. Since then, and based on requests from the wider astronomy community, it has been updated to Python 3.7 to work with CLOUDY 17 (C17).

One of the operational differences between C13 and C17 is the format the emission lines take as inputs. The newer version, C17, offers 290 emission lines (Morisset *et al.*, 2015) which are accessible directly from PYCROSS toolbar by selecting **References** — **Emission Line Index**. The structure of the emission lines from C13 and C17 are slightly different (see Table 4.1) and only function with their respective version of PYCROSS and PYCLOUDY²¹. All photoionisation models and data generated in this chapter was created using the latest version of PYCROSS using C17.

This chapter will describe the structure and kinematics of “*The Etched Hourglass Nebula*”, to show PYCROSS models were created from data acquired from previous research where authors investigated certain aspects concerning evolution, continuum, shaping and kinematics. Extrapolating necessary information from the literature allowed for the creation of a SHAPE model and yielded the necessary parameters (luminosity, blackbody temperature, abundances, etc.) as inputs into PYCROSS to create the models. The method outlined here differs slightly from that described in Fitzgerald *et al.* (2020), highlighting its ability to create models in different ways based on observations and information available.

4.2 The Etched Hourglass Nebula – MyCn 18

The *Etched Hourglass Nebula*, also known as MyCn 18, was the 18th of 39 objects detected by Mayall & Cannon (1940). It is a young PN (≈ 2500 yrs, Dayal *et al.* (2000)) located in the southern constellation of Musca (13h 39m

²¹They are distinguishable in that C17 includes a more detailed emission line correct to two decimal places postfixed with an **A**

CLOUDY Versions	
C13	C17
O 3 5007	O 3 5006.84A
PYCross V24	PYCross V26C

Table 4.1: C13 and C17 example emission line input comparison with corresponding PYCROSS versions. Emission lines used in C13 for PYCROSS V24 (Fitzgerald *et al.*, 2020) cannot be used with the new version of PYCROSS and vice versa. Emission line formats are restricted to be 8 characters for C13 and 12 characters for C17. Emission parameters are listed as they are inputted in C17 such that, for example, O 3 corresponds to [O III]

35.12s right ascension, $-67^{\circ} 22' 51.5''$ declination) at a distance of 3092 ± 507 pc (Miszalski *et al.*, 2018). Its symmetric hourglass structure and striking etchings were captured using narrowband filters on the Hubble Space Telescope’s (HST) WFPC2 camera, Figure 4.1, and published in Sahai *et al.* (1999). This image has intrigued astronomers, authors, and artists across the globe making it one of the most famous PN; since its publication, it has featured on album covers, in movies/video games, and on the cover of Kwok (2000) – “*The Origin and Evolution of Planetary Nebulae*”.

Previous research on this nebula may be categorised as MyCn 18 specific or part of a collection of targets where authors are investigating certain aspects concerning evolution, continuum, shaping, knots and kinematics. Over the last three decades astronomers have investigated MyCn 18 to determine the spatio-kinematics of its distinctive extreme bipolar morphology, of an open-ended hourglass with a narrow waist. Two of the most extensive studies were carried out by Sahai *et al.* (1999) and Dayal *et al.* (2000), who obtained emission-line and continuum images of MyCn 18. Observations were acquired using the HST Wide Field Planetary Camera 2 (WFPC2)²², in four narrowband filters: $H\alpha$ (green), [N II] (red), [O III] (blue) and [O I], and one continuum image using the medium band filter F547M which covers a section of the spectrum that has no discernible emission lines, (Sahai *et al.*, 1999).

Sahai *et al.* (1999) presented the images acquired from the observations and described in detail the structure, discussing their observational results. They cat-

²²The WFPC2 has a field of view of $34'' \times 30''$ and a scale of $0''.0456 \text{ pixels}^{-1}$

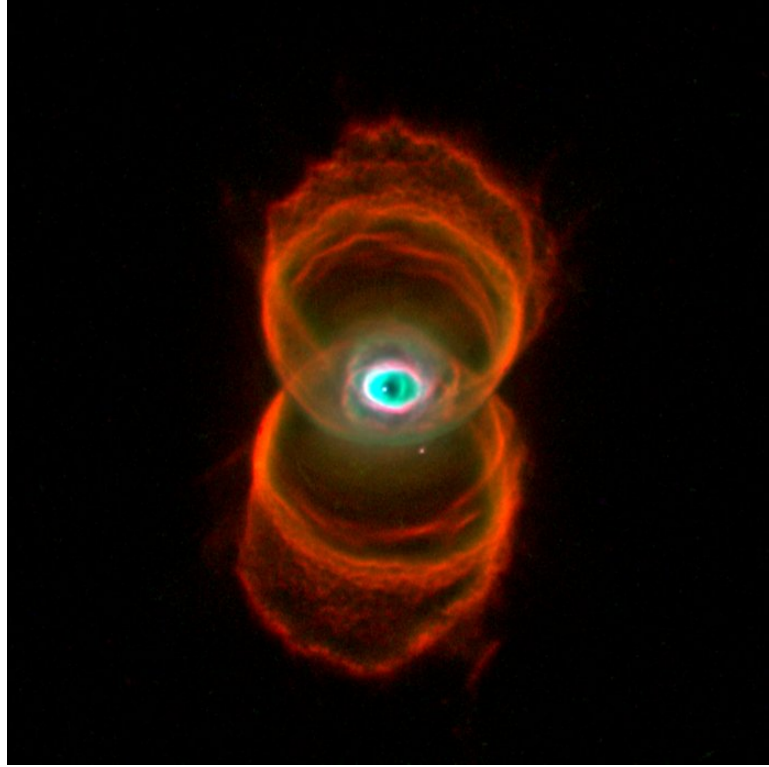


Figure 4.1: HST WFPC2 composite $H\alpha$ (green), $[\text{NII}]$ (red) and $[\text{OIII}]$ (blue) emission image. This famous image, originally created by [Sahai *et al.* \(1999\)](#), covers an area $24''.59 \times 23''.32$ ($540 \text{ pixels} \times 512 \text{ pixels}$), and required additional post processing to enhance and emphasise sharp structures such that the overlapping $[\text{NII}]$ and $H\alpha$ regions appear bright reddish–orange. Image reproduced from <https://www.spacetelescope.org/images/opo9607a/>.

egorised MyCn 18 into several distinct regions as a function of observed distances from the geometric centre of the nebula; hourglass walls, smooth and filamentary components, bright rims, mottled emissions and elongated knots that are approximately 220–250 AU wide and 550–1100 AU long see, [Figure 4.2 \(a\)](#). [Sahai *et al.* \(1999\)](#) concluded that the distinctive hourglass walls adhere to the interacting-winds hypothesis for PN formation, but the inner region, i.e. hourglass, ring and offset central star, require further study. Multiple mechanisms are discussed that may produce offsets within the central region, suggesting a preferred scenario being that of a wide binary companion, which has recently been found in [Miszalski *et al.* \(2018\)](#). Photometry of the central star inferred a $T_{eff} = 51,000 \text{ K}$ and $L_{bol} \approx 990 L_{\odot}$

[Dayal *et al.* \(2000\)](#) presented a 3D spatio-kinematic model using the $H\alpha$ (F656N) filter image, [Figure 4.2 \(b\)](#), and additional ground–based spectra. This model

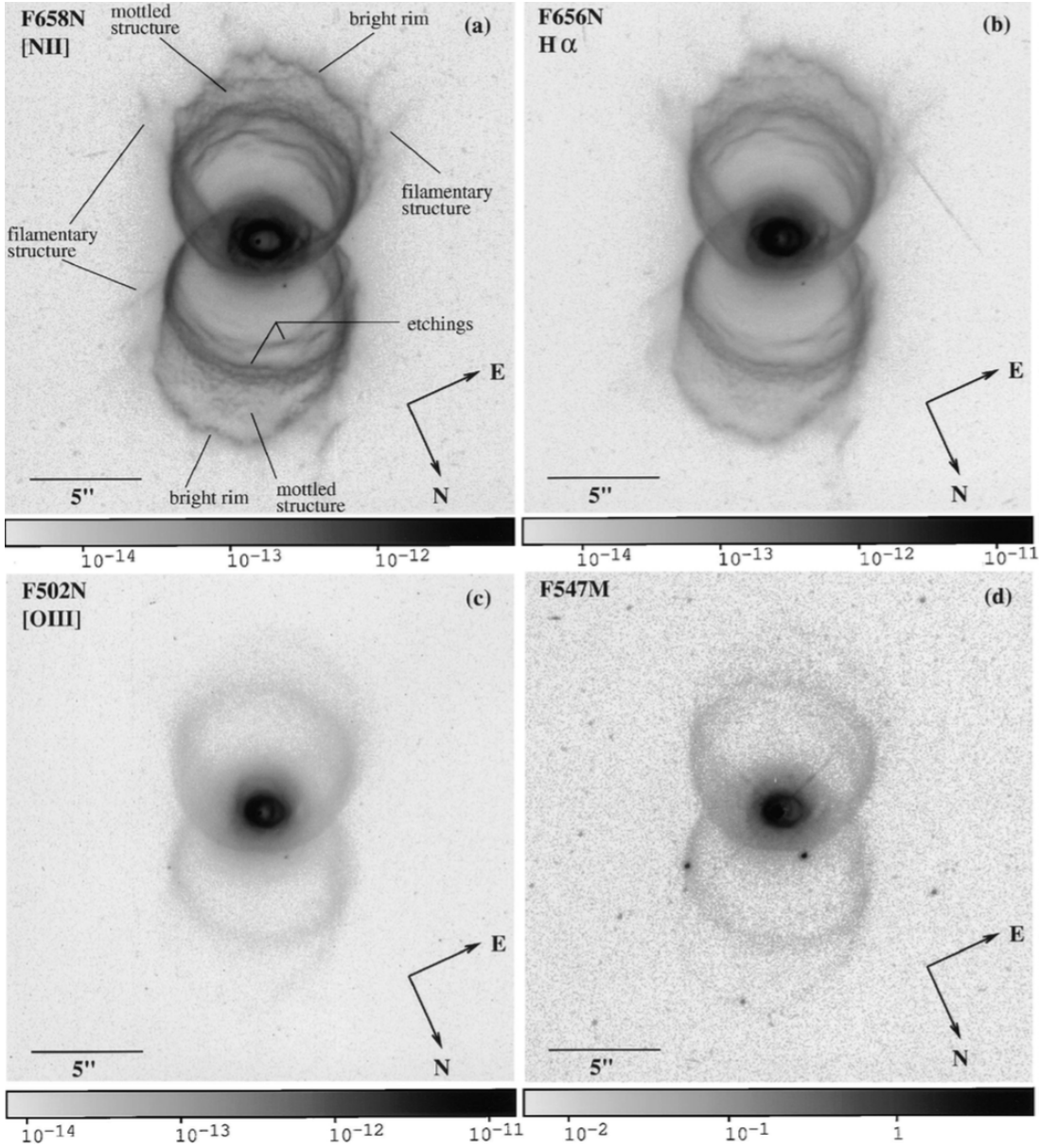


Figure 4.2: HST WFPC2 narrowband filters: (a) F658N ([NII] 6586Å), (b) F656N (H α), (c) F502N ([OIII]), and (d) continuum filter, F547M. Images are covering an area $22''.8 \times 22''.8$ (500×500 pixels). A logarithmic scale was used with maximum (*black*) and minimum (*white*) intensity values on a reverse grey scale being 8.43×10^{-12} and 2.93×10^{-13} ergs s $^{-1}$ cm $^{-2}$ arcsec $^{-2}$. Figure adapted from [Sahai et al. \(1999\)](#).

was used to determine the shape of the nebula walls as well as the density and kinematics of the emitting gas. A distance of 2.4 kpc to MyCn18 was adopted to model the outer hourglass as a pair of truncated paraboloids, however, the model did not attempt to describe the more complex inner hourglass and rings. [Dayal et al. \(2000\)](#) stated a reasonable fit to the data and assumed the nebula ex-

pands radially outwards following the radial power law, setting the radial velocity $V_r = 24 \text{ km s}^{-1}$, with a wall thickness of $(1.6 \pm 0.8) \times 10^{16} \text{ cm}$, again assuming a constant wall thickness throughout the nebula. An expansion timescale for the thin shell nebula, was estimated to be between 1000 – 2500 years. The spatial and kinematical constraints inferred an inclination of $\theta \approx 35^\circ - 38^\circ$ with respect to the line of sight, with an outer hourglass diameter of $\sim 4 \times 10^{16} \text{ cm}$ at the waist and, a height of $\sim 2.9 \times 10^{17} \text{ cm}$ from the centre of the nebula²³. Dayal *et al.* (2000), reiterates the generalised interacting stellar winds (GISW) model hypothesis for shaping outlined in Sahai *et al.* (1999), and approximates the total mass of ionised gas in the hourglass walls to be $0.013 M_\odot$ with an upper limit of $0.006 M_\odot$ of material inside the walls. Dayal *et al.* (2000) conclude that the walls of the nebula are density bound at higher latitudes and ionisation bound near the waist of the hourglass, potentially resulting from the mass-loss rate of the progenitor asymptotic giant branch (AGB) star during a thermal pulse or complex interaction between stellar winds.

A detailed optical and infrared study of MyCn 18 was carried out by Clyne *et al.* (2014) using the VLT Infrared Spectrometer And Array Camera (ISAAC) infrared spectra and long-slit optical Echelle spectra. This study not only yielded a geometric dimensional analysis of the nebula’s inner regions (Figure 4.3), but also its distant hyper-sonic knotty overflow. Clyne *et al.* (2014) surmise that the structure and shape of the inner hourglass are similar to that of the main hourglass inferring the same mechanism created both, and in theory, should follow a similar expansion velocity law ($V_{\text{exp}} \propto R^{0.6 \pm 0.4}$) described by Dayal *et al.* (2000). Clyne *et al.* (2014) discuss the statistical method used by Schwarz *et al.* (1992) to determine the distance to MyCn 18²⁴ and emphasises that distances calculated using this method are underestimated for nebulae of this type. A revised distance of 3.2kpc, based on the re-analysis by Stanghellini *et al.* (2008) of the statistical methods previously mentioned, was established.

²³These values are estimated with uncertainties of about $\pm 5\%$.

²⁴2.4kpc – Corradi & Schwarz (1993), 3.2kpc – Clyne *et al.* (2014); Miszalski *et al.* (2018). It is important to note that no confirmed value for distance to MyCn 18 has yet been accepted.

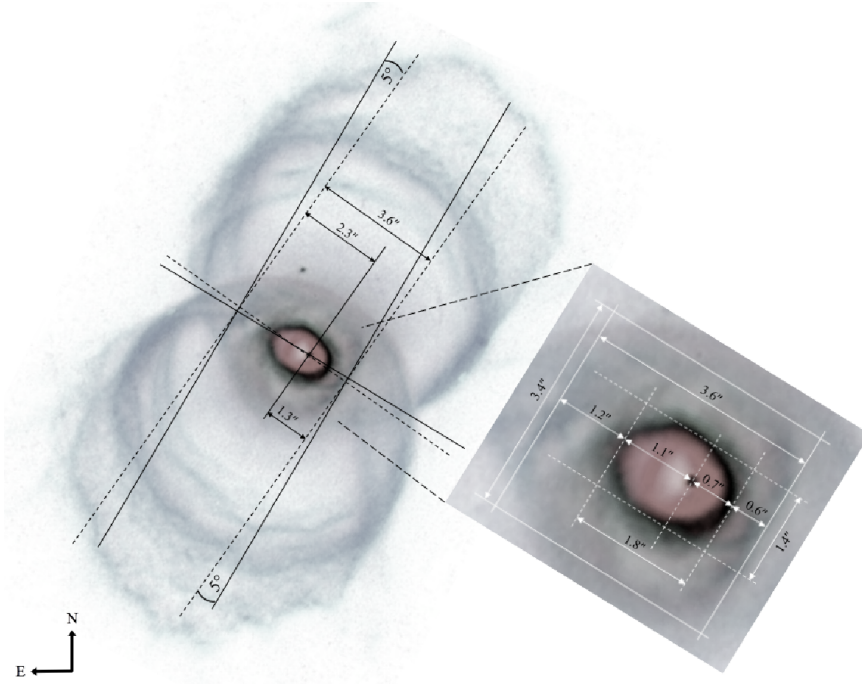


Figure 4.3: HST [NII] 6584 Å image of MyCn 18 with an overlaying geometric dimensional analysis showing the asymmetry and offset of the outer and inner hourglass respectively. [Clyne *et al.* \(2014\)](#) ascertained an offset and slightly tilted ($\approx 5^\circ$) inner hourglass, with respect to the main hourglass shell. Also observable is the offset central star with respect to the nebula centre. Figure adapted from [Clyne *et al.* \(2014\)](#).

A 3D morpho-kinematic SHAPE model of MyCn 18 was created using three main structures; the outer hourglass, the inner hourglass and central eye regions that were represented using a cylinder, sphere and torus. Velocity, density, thickness, squeeze and size modifiers were applied to achieve the desired shape and synthetic position–velocity (P–V) arrays; which were used to determine the kinematics of the nebula. Velocities within the nebula ranged from 0 km s^{-1} at the centre to 70 km s^{-1} at the poles (outer hourglass), 0 km s^{-1} at the centre to 30 km s^{-1} at the poles (inner hourglass), and 0 km s^{-1} at the centre to 10 km s^{-1} edge (inner ring). An arbitrary density scaling factor was used across the nebula with the outer hourglass set to 1, the etchings varying from 2 to 5, and the inner regions varied from 10–20. Assuming a distance of 3.2 kpc, [Clyne *et al.* \(2014\)](#) inferred from the model that the kinematical age of the fastest knots was $\sim 1650 \text{ yr}$, with an inner hourglass expansion velocity of $30 \pm 5 \text{ km s}^{-1}$, corresponding to a timescale of $1750 \pm 250 \text{ yr}$, and a kinematical age of the nebula of

~ 2700 yr. [Clyne *et al.* \(2014\)](#) hypothesise that the displacement of the central star, misalignment of the inner region and hypersonic knotty overflow may be due to the accretion of the material of a hot Jovian exoplanet after being engulfed during the AGB phase, leading to a nova-type explosion.

Regarding MyCn 18's complex inner offset structure, it has long been hypothesised that this might be the result of the engulfment of a Jovian planet during the AGB phase ([Bear & Soker, 2015](#); [Soker, 1997](#); [Clyne *et al.*, 2014](#)) or a companion to the offset central star ([Sahai *et al.*, 1999](#); [Dayal *et al.*, 2000](#); [O'Connor *et al.*, 2000](#); [Miszalski *et al.*, 2018](#)). Existence of a binary companion was confirmed by [Miszalski *et al.* \(2018\)](#) who presented South Africa Large Telescope (SALT) High-Resolution Spectrograph (HRS) observations of MyCn 18's nucleus. Radial velocity measurements from 26 spectra proved the presence of a post-common envelope binary nucleus; [Miszalski *et al.* \(2018\)](#) state that the formation scenario for MyCn 18 may be due to material from the common envelope ejection forming the main nebula and that this material, still bound to the binary, falls back to envelop the binary. This may then lead to the formation of the inner hourglass and jets. However, they note that the exact process in which this occurs remains uncertain and requires detailed simulations but is similar to that described by [Soker \(2017\)](#). [Miszalski *et al.* \(2018\)](#) also ruled out a previous hypothesis that MyCn 18 formed as a classical nova explosion ([O'Connor *et al.*, 2000](#)) as the orbital separation of 0.124 AU or $26.6 R_{\odot}$ is too large to allow for mass transfer via Roche-lobe overflow. Furthermore, an M5V secondary cannot provide the average accretion rate of $M_{acc} \sim 10^{-8} - 10^{-7} M_{\odot} \text{yr}^{-1}$ required to accrete the $M_{env} \sim 10^{-5} - 10^{-4} M_{\odot}$ mass required to form a classical nova in the ~ 1500 yr time-frame between the main nebula ejection when the jets are launched ([Clyne *et al.*, 2014](#)). While a classical nova origin may be ruled out, it does not however rule out a symbiotic one ([Clyne *et al.*, 2015](#)).

4.3 SHAPE morpho-kinematic Model

A new SHAPE morpho-kinematic model was created whose morphology reflects the findings in the previously discussed literature. This model consisted of three parts; an outer hourglass and inner hourglass and ring. In this instance, the model was not created in the manner discussed in [Harvey *et al.* \(2018\)](#); [Fitzgerald *et al.* \(2020\)](#); [Harvey *et al.* \(2020\)](#) but instead focused on re-creating the morphology of MyCn 18 from [Figure 4.1](#); offering users of PYCROSS the ability to model nova and nebula based on other observables. Once the model was created it is then scaled to the dimensions of the nebula and input into PYCROSS.

This SHAPE model originally consisted of a outer hourglass, inner hourglass and ring in [Figure 4.4](#), are coloured as blue, green and black respectively. The nebula is modelled from its centre to the extremity of the outer hourglass wall, the fast knots are excluded from this model as a code required that the model be axisymmetric. The model was then scaled and rotated to align the HST image of MyCn 18 in [Figure 4.1](#). A good geometrical fit and alignment were achieved resulting in a derived nebular inclination of 34° (in agreement with $38^\circ \pm 5^\circ$, determined by [Miszalski *et al.* \(2018\)](#) for the binary). Further modifications were required to enhance the etchings in the outer hourglass, this was achieved by replacing the single outer hourglass with six rings. Each ring is positioned at intervals along the outer hourglass, which are symmetrical around the nebula centre. These rings represented the denser region (etching) along the hourglass walls, see [Figure 4.5](#). This technique was recommended from a user of PYCROSS who used a similar approach to show denser regions of nebula (see [Figure 3.1](#) and [Figure 3.3 2\(a\)](#))

All components in the model are constructed from spheres, each having density, size, squeeze, and velocity modifiers applied. The SHAPE density modifier allows users to set the spatial distribution of density within a primitive and can be a constant or vary across the primitive. A number of constant and varying density models were tested, the model presented here consists of a fixed density across the nebula. Velocity modifiers were applied using the same radial Hubble,

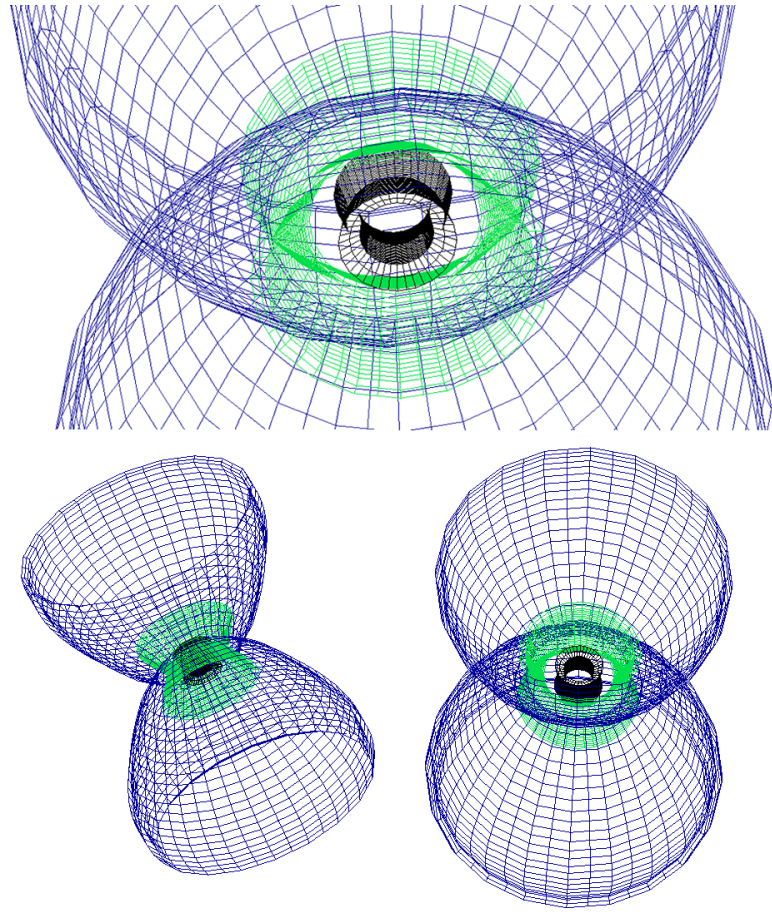


Figure 4.4: 3D Mesh Model of MyCn 18 at random orientations. The model is colour coded as follows: outer hourglass – blue, inner hourglass – green and ring – black.

and power laws outlined in [Clyne *et al.* \(2014\)](#); while all primitives have velocity modifiers, they are not required to construct a PYCROSS model but instead were used to ensure an accurate model in SHAPE. The finished structure shown in [Figure 4.5](#) shows the ring formation in frontal view, this model was then rendered and superimposed on the original image in [Figure 4.6](#).

Once a good morphological fit was achieved, the model was then orientated such that the long axis was pointing along the x-axis, as shown in [Figure 4.5](#). The *Image* and *Camera* parameters, within the SHAPE render module, were then adjusted to show a quadrant of the model, [Figure 4.7](#) (a). Finally, each primitive was reduced to create the “*slice*”, [Figure 4.7](#) (b), which was rendered to produce the data cube file required by PYCROSS. To create a data cube users must specify the name of the file (*.txt*) in the “*Renderer*” section. This file

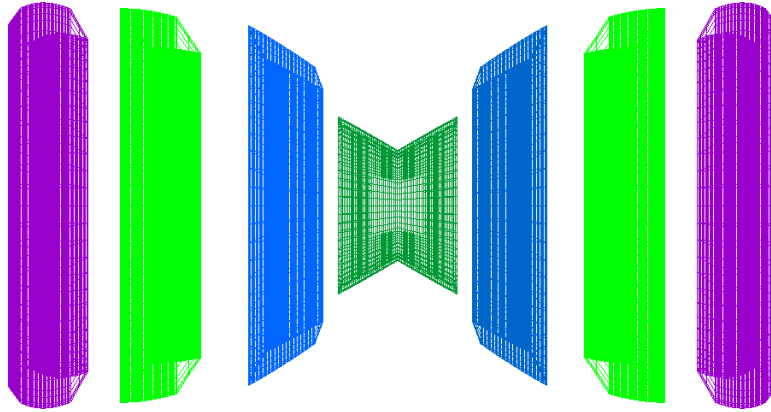


Figure 4.5: Frontal view of MyCn 18 3D SHAPE model. In this model 6 concentric rings (purple, light green and dark blue), represent the denser regions of the etchings in the outer hourglass.

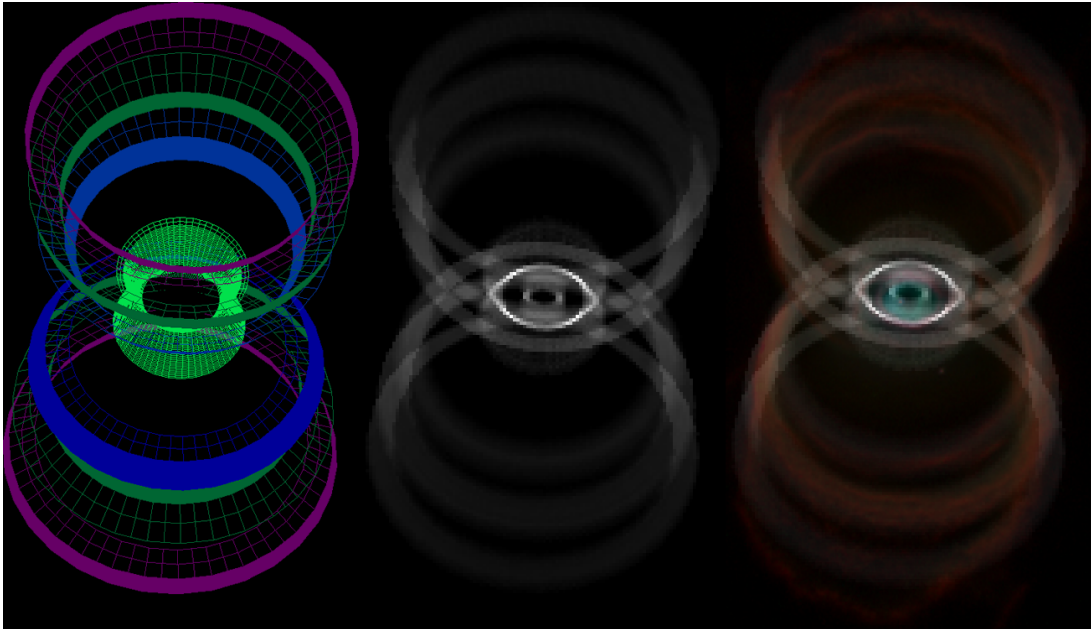


Figure 4.6: Left: 3D SHAPE mesh model. Centre: rendered view. Right: rendered image superimposed on HST image (Sahai *et al.*, 1999) to ascertain good geometrical fit. All have a position angle of 8° and inclination of 38° matching that of HST image in Figure 4.1

contains information relating to the name of the primitive, the (x,y,z) coordinates and corresponding velocity, density and temperature²⁵. An example of this is illustrated in Figure 4.8.

²⁵Not all parameters recorded are used in this release of PYCROSS

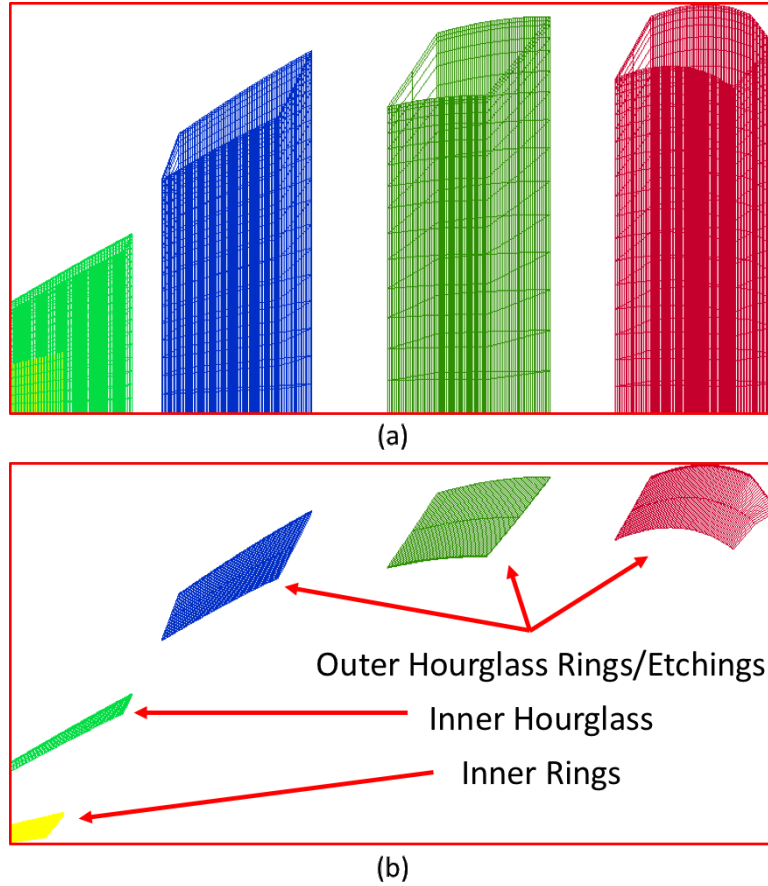


Figure 4.7: (a) Quadrant of MyCn18 SHAPE model model (Figure 4.5) viewed from the side at an angle of 0° . (b) Each primitive is then reduced by taking a slice which is then rendered to produce a data cube for input into PYCROSS. Slices of primitives are achieved by setting $\phi_{min} = 90^\circ$, $\phi_{max} = 180^\circ$, $\theta_{min} = -91^\circ$ and $\theta_{max} = -89^\circ$. An example of the data cube generation is illustrated in Figure 4.8

4.4 PYCROSS photoionisation modelling

A blackbody temperature of 51000 K (Sahai *et al.*, 1999) and a range of $\log L/L_\odot = 3 - 3.7$ were tested. The model follows CLOUDY recommendations of having a closed geometry with a small central object relative to the nebula; this is set via the “*sphere*” parameter. Setting the sphere parameter also sets another parameter to indicate that the nebula is expanding. Abundance sets are available and stored within CLOUDY for PNe, and selected by inputting “*abundances planetary no grains*” in the “*Cloudy Options*” window in PYCROSS. These abundances are derived from Aller & Czyzak (1983), and Khromov (1989) with high depletions assumed for elements they do not list. Finally, thirty angles were sam-

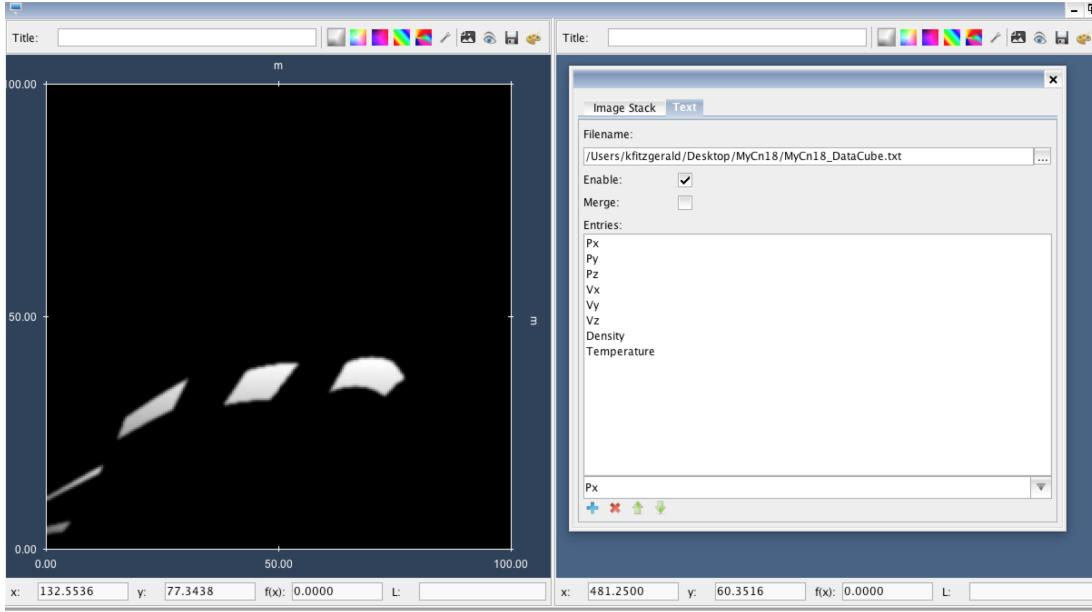


Figure 4.8: Example of the data cube generation in SHAPE. The image on the left shows render window and the orientation and centring required. the dialog window on the right of this shows how the data cube is generated with location of file, x,y,z spatial positions, velocity, density and temperature parameters exported. This data cube is then inputted into PYCROSS.

pled between $0^\circ - 90^\circ$. [Table 4.2](#) lists all parameters and emissions used in the generation of this model.

Two important emission lines in PNe include $[\text{O III}] 5007\text{\AA}$ and $[\text{N II}] 6584\text{\AA}$, as they reflect the thermal and ionising structure due to their cooling effect on the nebula ([Bohigas, 2008](#)). When ionised hydrogen is present, likely, ionised oxygen will also be present as the first ionisation potential of oxygen is almost identical to that of hydrogen; oxygen, however can be ionised more than once ([Dyson & Williams, 1997](#)). It is of no surprise that the images and spatio-kinematic model created by [Sahai *et al.* \(1999\)](#) and [Dayal *et al.* \(2000\)](#) focus on these two emissions.

Photoionisation models generated for $[\text{N II}]$, $\text{H}\alpha$, and $[\text{O III}]$ are displayed in [Figure 4.9](#) where the model is viewed at 0° on the left column and orientated on the right column to match a view similar to that shown in [Figure 4.2](#). Visual inspections of the models suggest that the $[\text{N II}]$ emission (see [Figure 4.9a](#) and [Figure 4.9b](#)) represents both the inner regions and its detailed etchings within the hourglass walls; structurally, this is consistent with the HST $[\text{N II}]$ image shown in [Figure 4.2 \(a\)](#). Good detail is shown in the inner regions of the $\text{H}\alpha$ and $[\text{O III}]$

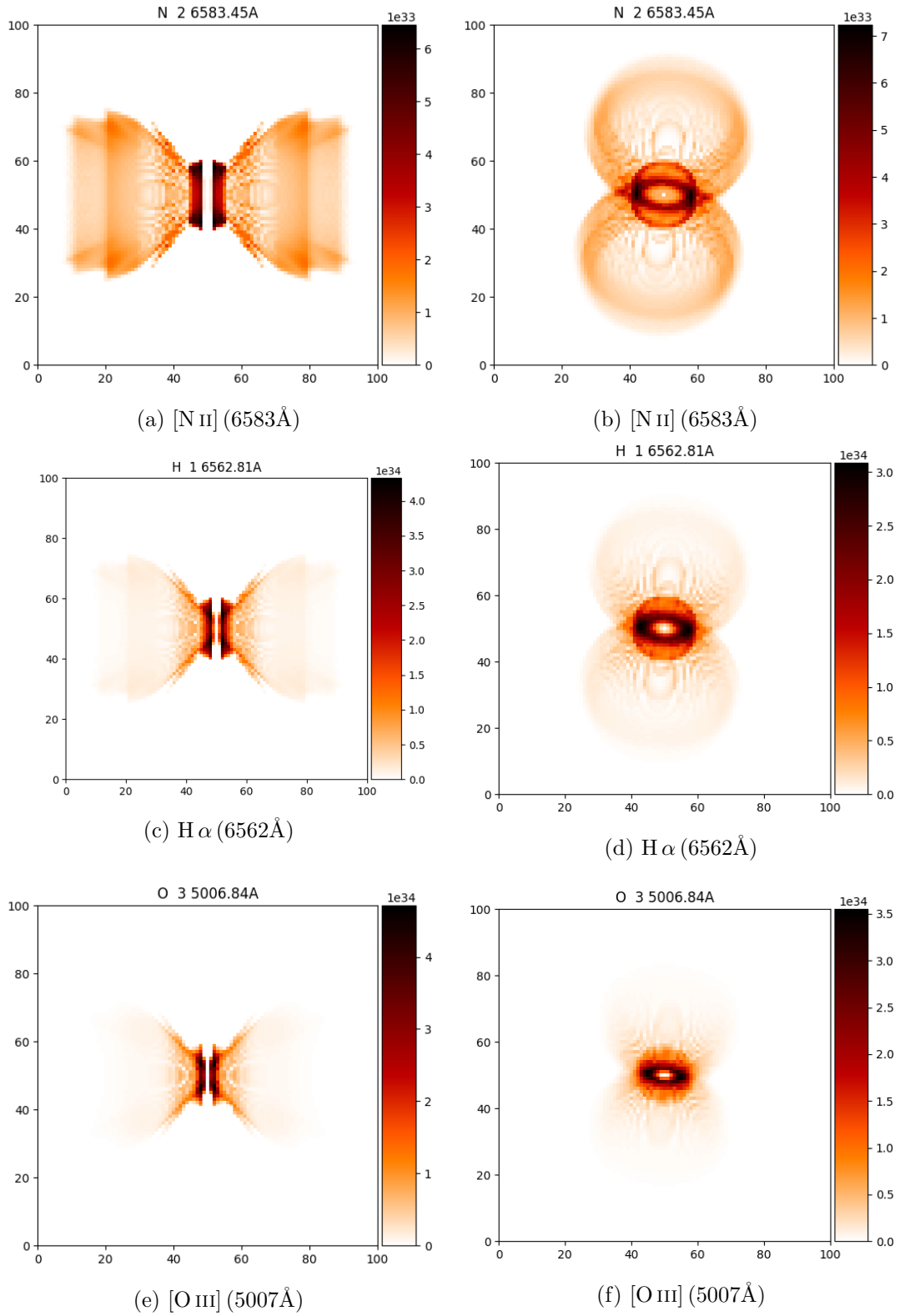


Figure 4.9: MyCn 18 photoionisation model views of [NII], H α , and [OIII]. Images on the left column show a frontal view of the model, and images on the right column are orientated to match a similar view as that shown in Figure 4.2. Colour Map: gist.heat.r.

<i>Parameter</i>	<i>Value</i>
Black Body	51000 K
Luminosity Sol	3.0
Start Angle	0°
Finish Angle	90°
Number of angles	30
Cloudy Options	abundances planetary no grains sphere
Emissions	H 1 6562.81A
	O 3 5006.84A
	N 2 6583.45A
	Fe 3 4658.01A
	O 1 6300.30A
	H 1 4861.33A
	He 2 4685.64A

Table 4.2: CLOUDY (C17) parameters used in PYCROSS. Emission parameters are listed as they are inputted in C17 such that, for example, O 3 corresponds to [O III]

models, however, the structure becomes faint towards the poles, similar to the images shown in Figure 4.9c and Figure 4.9e respectively. The $H\alpha$ structure is fainter towards the poles in the outer hourglass than that in Figure 4.2 (b). This might be due to the contamination this image experienced from [N II] as described by Sahai *et al.* (1999). Regarding the [OIII] region, while faint towards the poles in the outer hourglass, it can be seen that it forms near the $H\alpha$ region and is more centrally confined than [N II]. [OIII] forming near the $H\alpha$ ionising region may be due to rapid charge transfer between H and O.

Etchings in the outer hourglass wall are seen in greater contrast in [N II], Figure 4.9a than in $H\alpha$, and [OIII], and disappear at smaller radii where the walls become smoother. Figure 4.9b, which is rotated and aligned to match that in Figure 4.2 (a) also displays the open-ended hourglass geometry, inner regions are best resolved in $H\alpha$, and [O III]. Sahai *et al.* (1999) note that the inner regions is almost invisible in [O I], indicating that this region consists of more highly excited gas due to its proximity to the central star. Neither Sahai *et al.* (1999) or Dayal *et al.* (2000) present an image for [O I], however, the PYCROSS generated [O I] 6300Å photoionisation model shown in Figure 4.11a supports the

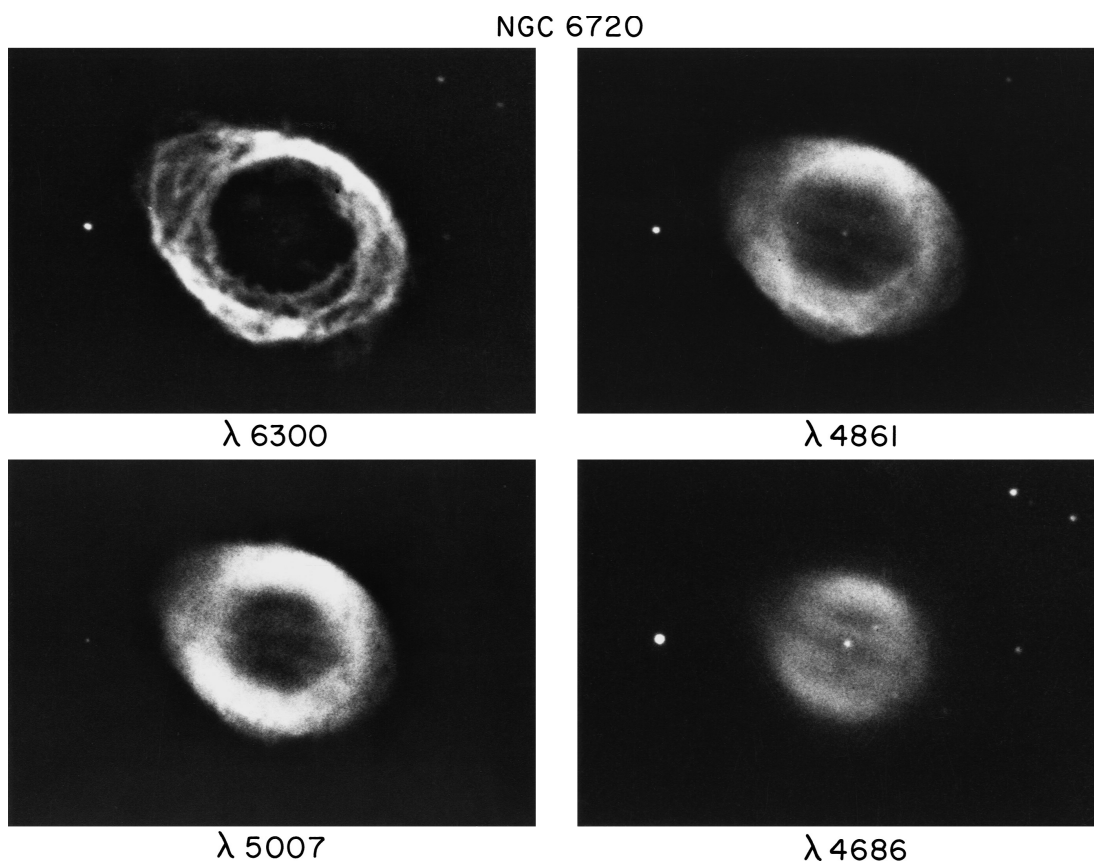


Figure 4.10: NGC 6720 – The Ring Nebula in [O I] 6300Å, H I 4861Å, [O III] 5007Å and He II 4686Å, emissions. The [O III] central hole may be as a result of a stellar wind of high-speed gas flowing out from the outer layers of the central star that evacuates the central region Figure adapted from <https://noirlab.edu/public/images/noao-02178/>.

observation by [Sahai *et al.* \(1999\)](#).

The ability to model emissions in this manner is a valuable tool in an astronomer’s arsenal, for example, [Osterbrock & Ferland \(2006\)](#) describes how the centre of many PN observed in the [O III] line has a central “hole” where the emission line is seen. This hole may be as a result of a stellar wind of high-speed gas flowing out from the outer layers of the central star that evacuates the central region, which can shock-heat temperature to $\geq 10^6$ K. There are cases where gas is present but is photoionised to high stages of ionisation that it emits little [O III] or other forbidden lines, such examples include He II and [Ne V].

[Osterbrock & Ferland \(2006\)](#) demonstrated this using four images of NGC 6720 (The Ring Nebula) in the following emissions: [O I] 6300Å, H I 4861Å, [O III]

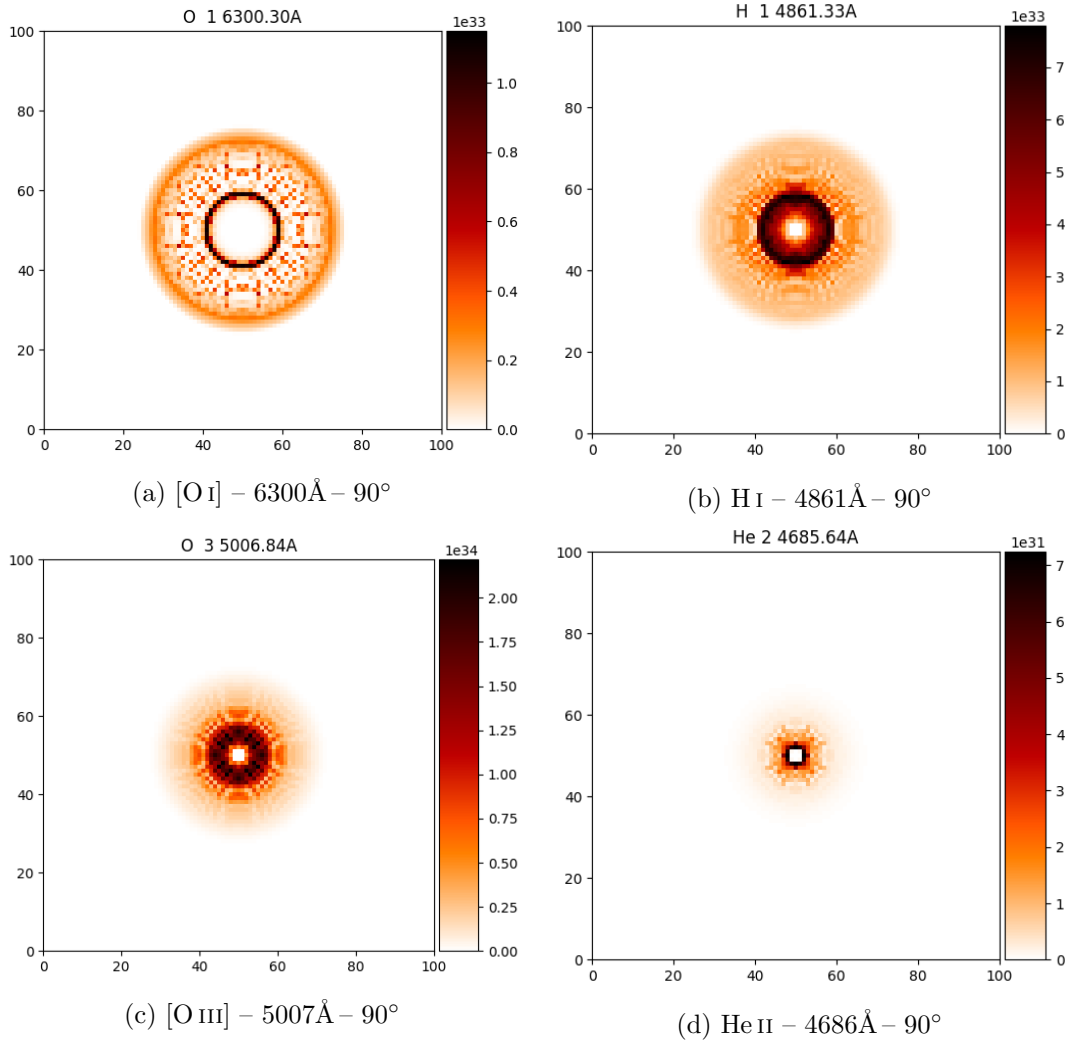


Figure 4.11: MyCn 18 photoionisation model views of [O I], H I, [O III] and He II. Models are arranged by emission to match that of Figure 4.10. Plots are viewed along the nebula poles (90°). Colour Map: gist_heat_r.

5007Å and He II 4686Å, see Figure 4.10. In this example a He II ionisation front occurs inside the [O I] region, accounting for the ring-like appearance in the [O III] image. Furthermore, the [O I] image marks the outer edge of the H I zone; [O I] regions forms near the H I ionisation front due to rapid charge transfer between H and O.

Using the photoionisation emission models generated here, it is possible to generate the same emissions, and rotate the model to determine if MyCn 18 shares the same characteristics. Proposed photoionisation models in [O I] 6300Å, H I 4861Å, [O III] 5007Å and He II 4686Å were created. These figures follow a

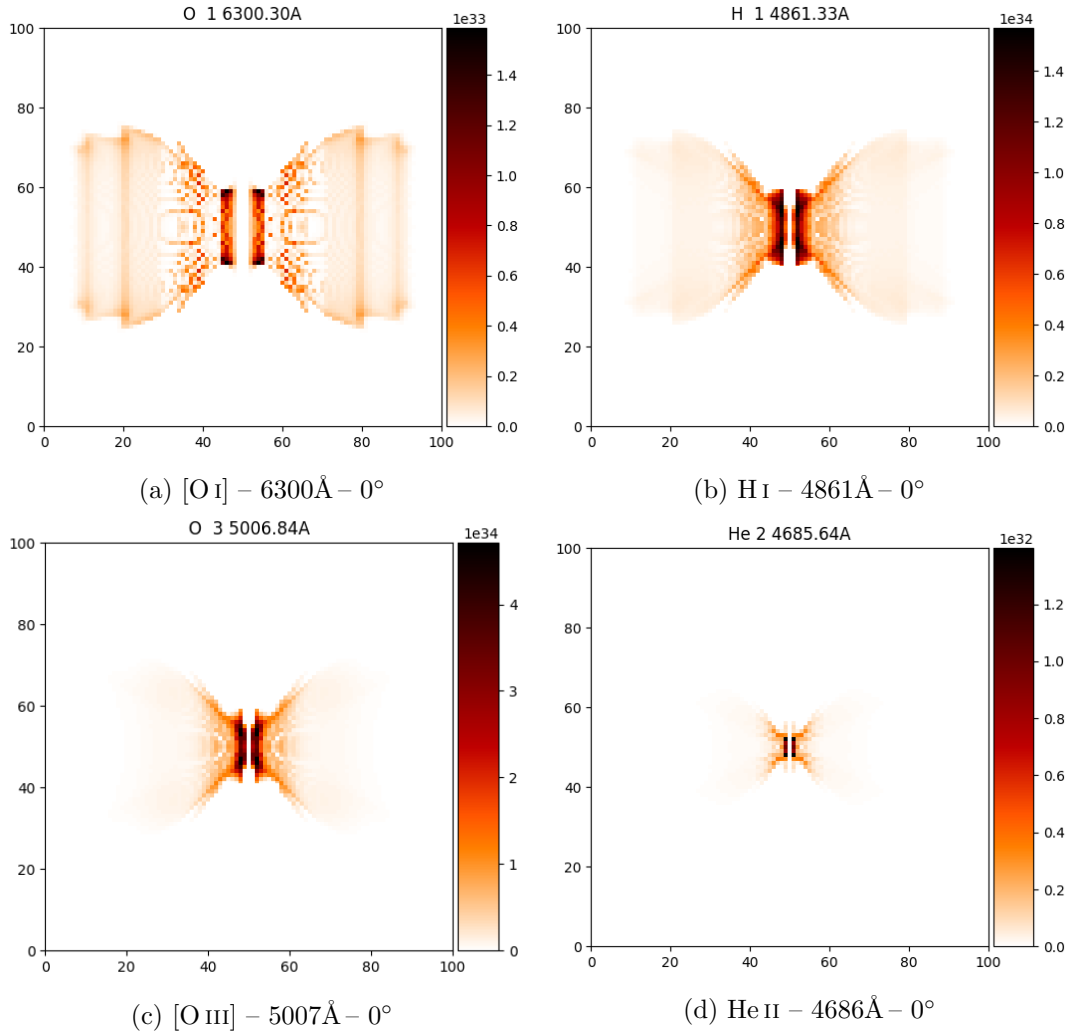


Figure 4.12: MyCn 18 photoionisation model views of [O I], H I, [O III] and He II. Models are arranged by emission to match that of Figure 4.10. Plots show a frontal view of the nebula. Colour Map: gist_heat_r.

similar layout to that presented by Osterbrock & Ferland (2006) in Figure 4.10; a view along the pole (90°) is shown in Figure 4.11, and an equatorial view (0°) is shown in Figure 4.12, for each emission model. While the [O I] region is extremely faint it can be seen that similar characteristics are observed where the He II ionisation front occurs inside this region in addition to this region forming near the H I ionisation front. The presence of gas in the central region suggests that the gas has been photoionised to such high stages of ionisation that it emits little [O III] or other low-ionisation forbidden lines, and is not evacuated due to the momentum of winds.

4.5 PYCROSS CLOUDY nebular diagnostics

PNe research often deals with the object as a point source while others work on spatially resolved structure, furthermore, photoionised nebulae are frequently assumed to have a uniform temperature, yet, photoionisation codes demonstrate the existence of temperature variations across each nebula. The existence of other physical processes suggests the existence of larger variations (Peimbert *et al.*, 2017).

CLOUDY generated data relating to the model is available to users and can be accessed by navigating to the *PyCloudy_Archive* folder, located in the home or C:\ drive. Data for each model is contained within a *.zip* file with the name, set by the user, and a timestamp for when that model was created. Users must extract the contents of the *.zip* file and navigate to the *MakeData* directory. This directory contains multiple files for each angle, with each file containing hundreds of lines of information relating to databases that play a role in the calculations, emissions over multiple iterations during CLOUDY calculations; the name of the line, species wavelength, flux and ratio relative to $H\beta$, electron temperature (t_e), electron density (n_e) and ionic abundances for the different regions. Experienced users of CLOUDY understand the structure and layout of this information and can navigate it with confidence. New users to CLOUDY and PYCLOUDY face a steep learning curve and this is something PYCROSS strives to eliminate.

The following information has been extrapolated from the CLOUDY files located in the *MakeData* directory for this MyCn 18 model. The latest version of PYCLOUDY was modified to examine the files to determine t_e , n_e , oxygen temperatures and ratios relative to H within the nebula. This feature offers users the opportunity to investigate different regions of the nebula, for example, [Figure 4.13](#) shows the SHAPE model slice of the nebula broken down into 5 parts. Each part has an associated angle from the nebula centre. CLOUDY files with angles that pass through these regions allow users to investigate specific parts of the nebula. In this scenario, the 9° angle passes through the equatorial region of the inner hourglass and ring, while the 43° , 53° and 65° angles pass through the denser

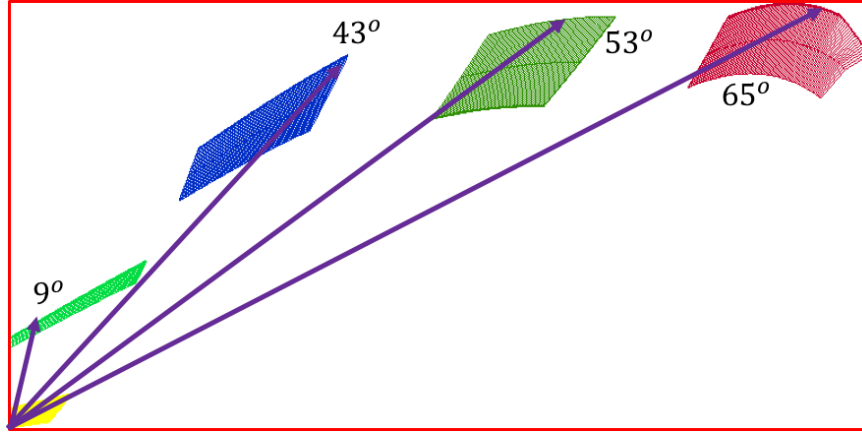


Figure 4.13: SHAPE model angle components; 9° picks up the inner ring and hourglass, for the outer hourglass, the first, second and third etchings are picked up by 43° , 53° , and 65° a breakdown of their components are listed in [Table 4.3](#)

Region: Inner hourglass and ring Region – 9°		
$H^+/H = 0.92$	$He^+/He = 0.89$	
$O^{++}/O = 0.19$	$O^+/O = 0.72$	
$N^{++}/N = 0.27$	$N^+/N = 0.69$	
$T(O^{+++}) = 9849$	$T(O^{++}) = 10032$	$T(O^+) = 10240$
Region: Outer hourglass ring/etching 1 – 43°		
$H^+/H = 0.90$	$He^+/He = 0.86$	
$O^{++}/O = 0.14$	$O^+/O = 0.74$	
$N^{++}/N = 0.21$	$N^+/N = 0.73$	
$T(O^{+++}) = 9507$	$T(O^{++}) = 9589$	$T(O^+) = 9823$
Region: Outer hourglass ring/etching 2 – 53°		
$H^+/H = 0.89$	$He^+/He = 0.85$	
$O^{++}/O = 0.13$	$O^+/O = 0.75$	
$N^{++}/N = 0.19$	$N^+/N = 0.74$	
$T(O^{+++}) = 9428$	$T(O^{++}) = 9485$	$T(O^+) = 9692$
Region: Outer hourglass ring/etching 3 – 65°		
$H^+/H = 0.88$	$He^+/He = 0.84$	
$O^{++}/O = 0.12$	$O^+/O = 0.75$	
$N^{++}/N = 0.17$	$N^+/N = 0.75$	
$T(O^{+++}) = 9344$	$T(O^{++}) = 9358$	$T(O^+) = 9536$

Table 4.3: MyCn18 model temperature diagnostics with temperatures in Kelvin. The nebula is dominated by neutral and first ionisation states of the species under study i.e. oxygen and nitrogen.

etchings on the outer hourglass. Oxygen temperatures and ionic abundances for four different regions are presented in [Table 4.3](#).

Given the whole ensemble of the integrated flux from the shell would imply,

for this model and geometry, temperatures across the different ionised states of oxygen decreases further from the ionisation source. The inner region at 9° is composed of approximately 19% O^{++}/O and 72% O^+/O with a temperature of 10032 K. The ionisation states in the detailed etchings of the outer hourglass walls also decreases the further from the ionising source with the outermost etching composing of approximately 12% O^{++}/O and 75% O^+/O with a temperature of 9358 K.

A study carried out by [Tsamis *et al.* \(2003\)](#) presented deep optical spectrophotometry of twelve Galactic PNe and three PNe, nine of which were observed by scanning a slit of the spectrograph across each nebula. In this study, MyCn 18 was a candidate with data acquired via ESO optical observations. The data was acquired from a fixed slit positioned through the nebular centre and passed through the brightest parts of the nebula using the central star as a guide. [Tsamis *et al.* \(2003\)](#) calculated electron densities and temperatures derived from several collisionally excited line diagnostic ratios using a software package called EQUIB. The slit position described by [Tsamis *et al.* \(2003\)](#) through the centre and brightest parts of the nebula, would also encompass the etchings and poles can be compared to the data generated via this model's 65° angle ([Table 4.3](#)), which also encompasses both the inner region, etchings of the nebula. However, there will be some discrepancy as [Tsamis *et al.* \(2003\)](#) focused on a fixed slit while this technique calculated the whole ensemble of the integrated flux from the shell.

4.6 Summary and conclusion

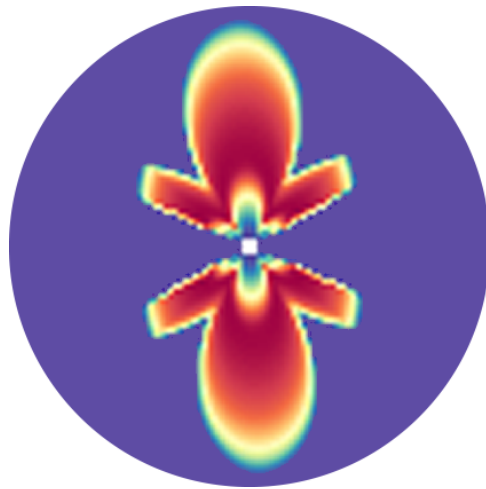
In this chapter, an updated version of PYCROSS is presented. The PN MyCn 18 was chosen as a target to demonstrate its compatibility with C17 and highlight its new functionality. Previous research into the structure and kinematics of MyCn 18 was discussed and a new morpho-kinematic SHAPE model was presented. The 3D SHAPE model and parameters from the literature generated multiple new PYCROSS photoionisation models of MyCn 18 that details

both its complex inner region and outer hourglass etchings in multiple emissions. Models generated were then used to show how users could infer the presence of species and distinguish between species boundaries (ionisation stratification). The determination of the ionisation structure of nebulae will offer astronomers greater insight into its kinematics and morphology and the ability to determine the presence of weaker lines which often go undetected if observations are not deep enough. (Peimbert *et al.*, 2017). Finally, new features were demonstrated to show how regions within the nebula can be analysed to determine densities and temperatures of different ionised states of O, N, H and He.

The blobs, knots and mottled structure described in Sahai *et al.* (1999); Clyne *et al.* (2014) does not exist in this model as this technique is limited to symmetrical, non-clumpy objects. Additionally, the inner regions are also symmetrical and not offset as described in the literature. The nebular diagnostic functionality described in the last section is not currently integrated or available in the versions of PYCROSS that are available online and will be included in the next release PYCROSS Version 27.

Chapter 5

Summary and future work



5.1 Summary

To summarise, research into the processes of photoionised gas plays a huge part in our understanding of stellar evolution, modelling non-stellar objects beyond our solar system however, is difficult as 3D volumetric objects are observed as 2D projections. As such, much effort has been invested into creating tools to model and visualise photoionised species within PNe and nova. These codes use various analytical or statistical techniques for the transfer of continuum radiation, mainly under the assumption of spherical symmetry. Increased computing power over the last 4 decades has further enhanced the development of photoionisation codes, allowing for the construction of more complex models reconstructed into 3D. The assumption of spherical symmetry has been retained in some, to help reduce computational overhead, in all cases however, the quality of data used to create the model, as well as a competent acquaintance with the assumptions that are made, are as important to improving our knowledge of a particular physical object or situation. Interactive databases (PyNeb, [Luridiana, V. *et al.*, 2015](#)) are now available to assist in determining temperature, density chemical composition, and other physical quantities to aid in defining the initial values for 3D photoionisation models.

Spectroscopic data of emission nebula, analysed with the tools of atomic physics and interstellar extinction models, yield little more than average values for the velocity, density, and temperature of a few regions along the line of sight. Photoionisation modelling is essential to researchers who wish to investigate the physical structure of their targets. It is important to note that while models are not a direct and exact depiction of reality, they can help extend or reconstruct our understanding of it ([Bohigas, 2008](#)).

The goal of this research was to develop a new pipeline and application for generating photoionisation models, created in SHAPE using CLOUDY and PY-CLOUDY, the resulting code was named PYCROSS ([Fitzgerald *et al.*, 2020](#)). This was achieved over the course of this thesis where various modelling techniques were described, outlining the importance to adhere to a specific SDLC that best

suited the project (Fitzgerald *et al.*, 2019). Employing and adhering to a SDLC when developing software applications for astronomy is essential to guarantee milestones are met while also giving greater control over complex projects and most importantly to ensure reliability and quality in use. PYCROSS was also developed to reduce the steep learning curves traditionally encountered when using specialist astronomy photoionisation codes. In Chapter 2, a detailed account of the installation, functionality, user interface and an operational overview was given using a theoretical model generated in SHAPE.

Utilising a SDLC proved instrumental in realising the objectives of this research. Over each iteration it was necessary to swap between many roles i.e. user-stories/requirements collection, developer/coder, tester and overall project manager. Adhering to the process allowed for consistency, clarity in project objectives, requirements and estimates while also building a rapport with experts in the field. Having a well-defined structure also helped with returning to research during occasions when work had to be halted, due to family and/or work commitments.

Numerous scientific applications were discussed in Chapter 3, where PYCROSS was employed in researching and modelling novae V5668 Sagittarii (2015) (Harvey *et al.*, 2018), V4362 Sagittarii (PTB 42) (Harvey *et al.*, 2020) and PN LoTr 1 (Fitzgerald *et al.*, 2020). Harvey *et al.* (2018) used PYCROSS in conjunction with other codes and techniques to better understand the early evolution of classical nova shells by modelling and visualising the ionisation structure of nova V5668. PYCLOUDY was used to examine emission line ratios by refining parameters acquired from a pool derived from a broad parameter of literature and data acquired from observations. The resulting PYCROSS photoionisation models gave further insight into the nova system as a whole. In Harvey *et al.* (2020) high-resolution spectroscopy was acquired from MES to find the radial velocity of individual components within the shell and created a number of morpho-kinematic SHAPE models to determine best-fit relationships between image, PV arrays and 1D line spectrum. PYCROSS models generated in this study detailed observed compo-

nents such as the equatorial and higher latitude rings, as well as polar features. PYCROSS was also applied to a PN, namely LoTr 1. Long-slit Echelle spectroscopy over eight different slit positions focusing on the [O III] 5007Å emission line was used to create a 3D morpho-kinematic SHAPE model. Densities, velocities and inner and outer shell radii measurements were incorporated into the model which was then compared against the PV arrays acquired from previous published observational data. A parameter sweep from literature who had previously determined luminosity, black body temperatures and abundances were used as CLOUDY inputs into PYCROSS.

Feedback from testers, users and reviewers regarding the applications usability, functionality and errors encountered during the preparation and publication of these pieces of research were noted and where possible incorporated into the next iteration of SDL. In all cases, spectroscopic and observational data was used to create a 3D SHAPE model. Additional CLOUDY parameters were derived from acquired spectra or extrapolated from published literature as inputs into PYCROSS, this has facilitated researchers with a tool to better understand and visualise the observed ionised nebula structures.

An updated version of PYCROSS was discussed in Chapter 4 with a demonstration given on the “*The Etched Hourglass Nebula*” (MyCn 18). This nebula was chosen to demonstrate its compatibility with C17 and highlight new functionality. Here the structure and kinematics of MyCn 18 are described with PYCROSS photoionisation models created on data acquired from previous research where authors investigated certain aspects concerning evolution, continuum, shaping and kinematics. The 3D SHAPE model and CLOUDY parameters needed were acquired from the literature, generated multiple new PYCROSS photoionisation models that details both its complex inner region and outer hourglass etchings in multiple emissions. Models generated were then used to show how it possible to infer the presence of species where a central cavity might be present in observations, while also allowing to distinguish between species boundaries (ionisation stratification). The determination of the ionisation structure of nebulae

will offer astronomers greater insight into its kinematics and morphology and the ability to determine the presence of weaker lines which often go undetected if observations are not deep enough (Peimbert *et al.*, 2017). Finally, new features were demonstrated to show how regions within the nebula can be analysed to determine densities and temperatures of different ionised states of O, N, H and He. The PYNEB nebular diagnostic functionality described in this chapter are not currently integrated or available in the versions of PYCROSS that are online. these will be included in the next release PYCROSS.

5.2 Future work

In 2017, PYCROSS was first presented to an international panel of Nova researchers and was positively received. During this seminar a sample of theoretical models were presented to demonstrate its capability at the time. The attendees did not see any user interfaces as this functionality was not part of the development during that iteration of the code. All contributed to the discussion and gave constructive feedback and recommendations for additional features that they deem essential or would like to see included, these formed additional user stories for the next iteration. All acknowledged its potential in their respective fields. Since then the code has gone through many iterations of the SDLC but it must be acknowledged that their contributions lead to the concept becoming a reality. Furthermore their use and promotion of PYCROSS will help drive its development into the future. As such, the scope and future potential for PYCROSS is extremely positive, feedback and requests from collaborators, users and reviewers is reassuring. In one known instance a user is attempting to apply the technique and code for research other than what is was designed for; to model and investigate the information about the composition and prospective atmospheric absorption predicted in exponents through investigating the small fraction of deflected source star light around the night-time side of the exoplanet.

However, with any new application there are always improvements to be made

and new features to be incorporated. To date, additional features and improvements have been requested by users and reviewers while others were discovered as a result of the iterative SDLC used in the development of PYCROSS. Listed below are some of the improvements and possible avenues that PyCross can take. To date these avenues are open ended and are listed in terms of their priority, with timescales in square brackets for the expected duration to take for completion. These estimates are based upon a single developer working part-time. It is hoped that some of this work would be expanded upon and developed as part of a research group.

Tutorial/Learning supports [4 months]: One of the most common requests from new users of PYCROSS is support material in the form of example SHAPE models, data cubes and parameter sets to generate models. Requests for accompanying screencasts to show the process in generating photoionisation models is also high, this includes creating a basic SHAPE model to loading the resulting data cube into PYCROSS, navigating the archive directory and plotting models. It is the hope to develop a set of tutorial screen-casts that will be freely available online. It is hoped that in the near future a set of short screencasts will be created to describe the above processes and will be similar and in keeping with that offered by [ShapeScience YouTube](#)²⁶ channel which offers screen-casts for the SHAPE software.

Open-source Software [6 - 8 months]: Currently PYCROSS is a bundled application developed using Python, this means that all code, necessary libraries and any additional packages are contained within a single application. This was to overcome any issues user may encounter with downloading and installing packages, which may prove problematic for both new and experienced astronomers alike. These Python libraries and packages are constantly being updated to either remove bugs, become more efficient or add additional features. To keep updating

²⁶ShapeScience YouTube channel offering screencasts for SHAPE Software:
<https://www.youtube.com/channel/UCqsrlnBFpTPZfS10lgkUHRA>

the application based on new libraries etc. would be extremely time-consuming and over time, may be off-putting to users with multiple releases over a short period. A solution to this is to make the source code available to the general public, this is referred to as open-source software.

Open-source software is source code that has been released under a license in which the copyright holder grants users the rights to use, study, change, and distribute the software to anyone and for any purpose. Making the source code available to the general public has multiple benefits. It removes the need to constantly bundle and release new updates as users can download the necessary libraries and packages depending on their own requirements. Having the source code open-source allows for future development in a collaborative public manner, this brings greater insights and experience into the fold with future development. Finally, making open-source code will allow future and existing astronomers the ability to develop their coding skills with working examples.

Grids of models [> 1 year]: Currently there is no facility in PYCROSS to generate and run a grid of models, users must run a single model at a time. The general consensus from users and reviewers is to include the facility in future releases that will allow for this. This feature could be developed using external files containing the requirements and parameters which is automated to run via a terminal between specific ranges. This feature may be better suited for an open-source release.

Line Intensity Diagrams [> 1 year]: Recent discussions and correspondence with Christophe Morisset, developer of PYCLOUDY ([Morisset, 2013](#)), have already proved fruitful with current and future collaborations regarding PYCROSS. During recent discussions a new feature was identified where users will be able to define slits using their cursor on a model to produce the line intensities (normalised to $H\beta$) through this slit. This feature is planned for the next release.

SHAPE photoionisation module [> 2 years]: It is without doubt that SHAPE has proven its value in astrophysics research since its release over a decade ago. One feature missing from SHAPE is a module that can generate photoionisation models. Both Nico Koning and Wolfgang Steffen, (creators of SHAPE) have shown their support of PYCROSS and more recently have supported this idea. A possible evolution from PYCROSS could be developed to be integrated into SHAPE as an extension/module. Incorporating a module in this manner would also allow for the automated rotation, positioning and generation of slice that users must currently do manually.

Incorporating light curve fitting functionality [6 months]: The Galway Ultra-Fast Imager (GUFU) located on the 1.8m Vatican Advanced Technology Telescope (VATT) was tasked to monitor tight brown dwarf binaries. However, due to the close separation between the components in these binaries, the GUFU photometer could not image each component of binary systems as a point source. Therefore, a novel application was developed called the “Light Curve Fitter”. This application was developed using the same SDLC as PYCROSS (also written in Python), and is capable of distinguishing two superimposed sinusoidal waves. Integrating this code into PYCROSS would allow users to, in a scenario where they were developing photoionisation models of systems with close binaries, investigate the photometric data where fluxes are combined to distinguish two superimposed sinusoidal waves revealing the variability signature from the more dominant primary variability.

To conclude, PYCROSS has proven its use not only in astrophysics research but also as a educational tool as it is currently being used by undergraduate and masters students to develop models. The examples of future works above, while summarised, show considerable scope both for research opportunities and future collaborations.

Bibliography

- ABELL, G.O. & GOLDREICH, P. (1966). On the Origin of Planetary Nebulae. *Publications of the Astronomical Society of the Pacific*, **78**, 232. [5](#)
- AKASHI, M. & SOKER, N. (2017). Shaping planetary nebulae with jets in inclined triple stellar systems. *Monthly Notices of the Royal Astronomical Society*, **469**, 3296–3306. [23](#)
- AKASHI, M., BEAR, E. & SOKER, N. (2018). Forming H-shaped and barrel-shaped nebulae with interacting jets. *Monthly Notices of the Royal Astronomical Society*, **475**, 4794–4808. [23](#)
- AKRAS, S., CLYNE, N., BOUMIS, P., MONTEIRO, H., GONÇALVES, D.R., REDMAN, M.P. & WILLIAMS, S. (2016). Deciphering the bipolar planetary nebula Abell 14 with 3D ionization and morphological studies. *Monthly Notices of the Royal Astronomical Society*, **457**, 3409–3419. [43](#)
- AKRAS, S., GUZMAN-RAMIREZ, L., LEAL-FERREIRA, M.L. & RAMOS-LARIOS, G. (2019a). A census of symbiotic stars in the 2mass, wise, and gaia surveys. *The Astrophysical Journal Supplement Series*, **240**, 21. [25](#), [26](#)
- AKRAS, S., LEAL-FERREIRA, M.L., GUZMAN-RAMIREZ, L. & RAMOS-LARIOS, G. (2019b). A machine learning approach for identification and classification of symbiotic stars using 2MASS and WISE. *Monthly Notices of the Royal Astronomical Society*, **483**, 5077–5104. [25](#)
- ALLEN, A. & SCHMIDT, J. (2015). Looking before leaping: Creating a software registry. *Journal of Open Research Software*, 3(1), p.e15,. [45](#)

- ALLER, L. & CZYZAK, S. (1983). Chemical compositions of planetary nebulae. *The Astrophysical Journal Supplement Series*, **51**, 211–247. [85](#), [101](#)
- ASTELS, D. (2003). *Test-Driven Development: A Practical Guide*. Prentice Hall, 1st edn. [45](#)
- BALICK, B., PERINOTTO, M., MACCIONI, A., TERZIAN, Y. & HAJIAN, A. (1994). FLIERs and other microstructures in planetary nebulae, 2. *The Astrophysical Journal*, **424**, 800–816. [14](#)
- BALLESTER, P., GABASCH, A., JUNG, Y., MODIGLIANI, A., TAYLOR, J., COCCATO, L., FREUDLING, W., NEESER, M. & MARCHETTI, E. (2015). The High Level Data Reduction Library. In A.R. Taylor & E. Rosolowsky, eds., *Astronomical Data Analysis Software and Systems XXIV (ADASS XXIV)*, vol. 495 of *Astronomical Society of the Pacific Conference Series*, 383. [45](#)
- BAUER, A.E., BELLM, E.C., BOLTON, A.S., CHAUDHURI, S., CONNOLLY, A.J., CRUZ, K.L., DESAI, V., DRLICA-WAGNER, A., ECONOMOU, F., GAFFNEY, N., KAVELAARS, J., KINNEY, J., LI, T.S., LUNDGREN, B., MARGUTTI, R., NARAYAN, G., NORD, B., NORMAN, D.J., O’MULLANE, W., PADHI, S., PEEK, J.E.G., SCHAFER, C., SCHWAMB, M.E., SMITH, A.M., TOLLERUD, E.J., WEIJMANS, A.M. & SZALAY, A.S. (2019). Petabytes to science. Workshop on Instrumentation and Methods for Astrophysics, Las Vegas. [44](#)
- BEAR, E. & SOKER, N. (2015). Planetary systems and real planetary nebulae from planet destruction near white dwarfs. *ArXiv e-prints*. [97](#)
- BECK, K. (2002). *Test Driven Development. By Example (Addison-Wesley Signature)*. Addison-Wesley Longman, Amsterdam. [45](#)
- BECK, K., BEEDLE, M., VAN BENNEKUM, A., COCKBURN, A., CUNNINGHAM, W., FOWLER, M., GRENNING, J., HIGHSMITH, J., HUNT, A., JEFFRIES, R., KERN, J., MARICK, B., MARTIN, R.C., MELLOR, S.,

-
- SCHWABER, K., SUTHERLAND, J. & THOMAS, D. (2001). Manifesto for agile software development. <http://agilemanifesto.org>, accessed: 2016-09-20. 48
- BELCZYŃSKI, K., MIKOŁAJEWSKA, J., MUNARI, U., IVISON, R.J. & FRIEDJUNG, M. (2000). A catalogue of symbiotic stars. *Astronomy & Astrophysics, Supplement*, **146**, 407–435. 25
- BODE, M.F. (2010). The outbursts of classical and recurrent novae. *Astronomische Nachrichten*, **331**, 160. 30
- BODE, M.F. & EVANS, A. (2008). *Classical Novae*. University Press, 2nd edn. xii, 28, 29, 30, 33, 80
- BOFFIN, H. & JONES, D. (2019). *The Importance of Binaries in the Formation and Evolution of Planetary Nebulae*. SpringerBriefs in Astronomy, Springer International Publishing. 23, 82
- BOHIGAS, J. (2008). Photoionization models applied to planetary nebulae. *The Astrophysical Journal*, **674**, 954. 74, 102, 113
- BOND, H.E. (1976). Objects common to the Catalogue of Galactic Planetary Nebulae and the General Catalogue of Variable Stars. *Publications of the Astronomical Society of the Pacific*, **88**, 192–194. 22
- BOWEN, I.S. (1928). Additional Series Lines in the Spectra of C II and N II. *Physical Review*, **34**, 534–536. 5
- BOYLE, L. (2018). *Planet engulfment and the planetary nebula morphology mystery*. Ph.D. thesis, Centre for Astronomy, School of Physics, National University of Ireland, Galway. xv, 21
- BRAY, E.M. (2014). Astropy: Building Blocks for Astronomy Software. In N. Manset & P. Forshay, eds., *Astronomical Data Analysis Software and Systems XXIII*, vol. 485 of *Astronomical Society of the Pacific Conference Series*, 343. 45

- CHU, Y.H., JACOBY, G.H. & ARENDT, R. (1987). Multiple-shell planetary nebulae. I - Morphologies and frequency of occurrence. *The Astrophysical Journal, Supplement*, **64**, 529–544. [14](#)
- CLYNE, N., REDMAN, M.P., LLOYD, M., MATSUURA, M., SINGH, N. & MEABURN, J. (2014). VLT observations of the asymmetric Etched Hourglass Nebula, MyCn 18. *Astronomy & Astrophysics*, **569**, A50. [xiii](#), [42](#), [95](#), [96](#), [97](#), [99](#), [111](#)
- CLYNE, N., AKRAS, S., STEFFEN, W., REDMAN, M.P., GONALVES, D.R. & HARVEY, E. (2015). A morpho-kinematic and spectroscopic study of the bipolar nebulae: M 2-9, mz 3, and hen 2-104. *Astronomy & Astrophysics*, **582**. [28](#), [97](#)
- COLLINS, K.A., KIELKOPF, J.F., STASSUN, K.G. & HESSMAN, F.V. (2017). AstroImageJ: Image processing and photometric extraction for ultra-precise astronomical light curves. *The Astronomical Journal*, **153**, 77. [45](#)
- CORRADI, R.L.M. & SCHWARZ, H.E. (1993). Bipolar nebulae and binary stars : the family of crabs He 2-104, BI Crucis and MyCn 18. *Astronomy & Astrophysics*, **268**, 714–725. [95](#)
- CORRADI, R.L.M., LIVIO, M., BALICK, B., MUNARI, U. & SCHWARZ, H.E. (2001). The southern crab from a new perspective. *The Astrophysical Journal*, **553**, 211–218. [28](#)
- CORRADI, R.L.M., GARCÍA-ROJAS, J., JONES, D. & RODRÍGUEZ-GIL, P. (2015). Binarity and the Abundance Discrepancy Problem in Planetary Nebulae. *The Astrophysical Journal*, **803**, 99. [18](#)
- CURTIS, H.D. (1918). The Planetary Nebulae. *Publications of Lick Observatory*, **13**, 55–74. [12](#)
- DARNLEY, M.J., HENZE, M., BODE, M.F., HACHISU, I., HERNANZ, M., HORNOCH, K., HOUNSELL, R., KATO, M., NESS, J.U., OSBORNE, J.P.,

-
- PAGE, K.L., RIBEIRO, V.A.R.M., RODRÍGUEZ-GIL, P., SHAFTER, A.W., SHARA, M.M., STEELE, I.A., WILLIAMS, S.C., ARAI, A., ARCAVI, I., BARSUKOVA, E.A., BOUMIS, P., CHEN, T., FABRIKA, S., FIGUEIRA, J., GAO, X., GEHRELS, N., GODON, P., GORANSKIJ, V.P., HARMAN, D.J., HARTMANN, D.H., HOSSEINZADEH, G., HORST, J.C., ITAGAKI, K., JOSÉ, J., KABASHIMA, F., KAUR, A., KAWAI, N., KENNEA, J.A., KIYOTA, S., KUČÁKOVÁ, H., LAU, K.M., MAEHARA, H., NAITO, H., NAKAJIMA, K., NISHIYAMA, K., O'BRIEN, T.J., QUIMBY, R., SALA, G., SANO, Y., SION, E.M., VALEEV, A.F., WATANABE, F., WATANABE, M., WILLIAMS, B.F. & XU, Z. (2016). M31n 2008-12a—THE REMARKABLE RECURRENT NOVA IN m31: PANCHROMATIC OBSERVATIONS OF THE 2015 ERUPTION. *The Astrophysical Journal*, **833**, 149. [31](#)
- DARNLEY, M.J., HOUNSELL, R., O'BRIEN, T.J., HENZE, M., RODRÍGUEZ-GIL, P., SHAFTER, A.W., SHARA, M.M., VAYTET, N.M.H., BODE, M.F., CIARDULLO, R., DAVIS, B.D., GALERA-ROSILLO, R., HARMAN, D.J., HARVEY, E.J., HEALY, M.W., NESS, J.U., RIBEIRO, V.A.R.M. & WILLIAMS, S.C. (2019). A recurrent nova super-remnant in the andromeda galaxy. *Nature*, **565**, 460–463. [31](#)
- DAVIES, R.I., AGUDO BERBEL, A., WIEZORREK, E., CIRASUOLO, M., FÖRSTER SCHREIBER, N.M., JUNG, Y., MUSCHIELOK, B., OTT, T., RAMSAY, S., SCHLICHTER, J., SHARPLES, R. & WEGNER, M. (2013). The Software Package for Astronomical Reductions with KMOS: SPARK. *Astronomy & Astrophysics*, **558**, A56. [45](#)
- DAYAL, A., SAHAI, R., WATSON, A.M., TRAUGER, J.T., BURROWS, C.J., STAPELFELDT, K.R. & GALLAGHER, I., JOHN S. (2000). The Etched Hourglass Nebula MyCN 18. II. A Spatio-kinematic Model. *The Astronomical Journal*, **119**, 315–322. [91](#), [92](#), [93](#), [94](#), [95](#), [97](#), [102](#), [104](#)
- DE MARCO, O. (2009). The origin and shaping of planetary nebulae: Putting the binary hypothesis to the test. *Publications of the Astronomical Society of*

-
- the Pacific*, **121**, 316–342. [24](#)
- DEPEW, K., PARKER, Q.A., MISZALSKI, B., DE MARCO, O., FREW, D.J., ACKER, A., KOVACEVIC, A.V. & SHARP, R.G. (2011). Newly discovered Wolf-Rayet and weak emission-line central stars of planetary nebulae. *Monthly Notices of the Royal Astronomical Society*, **414**, 2812–2827. [86](#)
- DERLOPA, S., AKRAS, S., BOUMIS, P. & STEFFEN, W. (2019). High-velocity string of knots in the outburst of the planetary nebula Hb4. *Monthly Notices of the Royal Astronomical Society*, **484**, 3746–3754. [42](#), [86](#)
- DOYLE, S., BALICK, B., CORRADI, R.L.M. & SCHWARZ, H.E. (2000). The evolving morphology of the bipolar nebula m2-9. *The Astronomical Journal*, **119**, 1339–1344. [43](#)
- DUNCAN, J.C. (1937). Photographic Studies of Nebulae. Fifth Paper. *The Astrophysical Journal*, **86**, 496. [14](#)
- DYSON, J.E. & WILLIAMS, D.A. (1997). *The physics of the interstellar medium*. Taylor & Francis, 2nd edn. [32](#), [87](#), [102](#)
- ECONOMOU, F., HOBLITT, J.C. & NORRIS, P. (2014). Your data is your dog-food: DevOps in the astronomical observatory. *arXiv e-prints*. [45](#)
- ERCOLANO, B. (2005). New Advances in Photoionisation Codes: How and what for? In R. Szczerba, G. Stasińska & S.K. Gorny, eds., *Planetary Nebulae as Astronomical Tools*, vol. 804 of *American Institute of Physics Conference Series*, 35–43. [41](#)
- ERCOLANO, B., BARLOW, M.J., STOREY, P.J. & LIU, X.W. (2003). MO-CASSIN: a fully three-dimensional Monte Carlo photoionization code. *mnras*, **340**, 1136–1152. [35](#), [41](#)
- EVANS, A., YUDIN, R.V., NAYLOR, T., RINGWALD, F.A. & KOCH MIRAMOND, L. (2002). Broadband polarimetry of novae in outburst. *Astronomy & Astrophysics*, **384**, 504–512. [80](#)

- FANG, X., ZHANG, Y., KWOK, S., HSIA, C.H., CHAU, W., RAMOS-LARIOS, G. & GUERRERO, M.A. (2018). Extended Structures of Planetary Nebulae Detected in H₂ Emission. *The Astrophysical Journal*, **859**, 92. [43](#)
- FERLAND, G.J., WILLIAMS, R.E., LAMBERT, D.L., SHIELDS, G.A., SLOVAK, M., GONDHALEKAR, P.M. & TRURAN, J.W. (1984). IUE observations of DQ Herculis and its nebula, and the nature of the cold nova shells. *The Astrophysical Journal*, **281**, 194–204. [81](#)
- FERLAND, G.J., KORISTA, K.T., VERNER, D.A., FERGUSON, J.W., KINGDON, J.B. & VERNER, E.M. (1998). CLOUDY 90: Numerical Simulation of Plasmas and Their Spectra. *Publications of the Astronomical Society of the Pacific*, **110**, 761–778. [3](#), [35](#), [41](#)
- FERLAND, G.J., PORTER, R.L., VAN HOOF, P.A.M., WILLIAMS, R.J.R., ABEL, N.P., LYKINS, M.L., SHAW, G., HENNEY, W.J. & STANCIL, P.C. (2013). The 2013 Release of Cloudy. *Revista Mexicana de Astronomia y Astrofisica*, **49**, 137–163. [3](#), [35](#), [41](#)
- FERLAND, G.J., CHATZIKOS, M., GUZMÁN, F., LYKINS, M.L., VAN HOOF, P.A.M., WILLIAMS, R.J.R., ABEL, N.P., BADNELL, N.R., KEENAN, F.P., PORTER, R.L. & STANCIL, P.C. (2017). The 2017 Release Cloudy. *Revista Mexicana de Astronomia y Astrofisica*, **53**, 385–438. [3](#), [35](#), [37](#), [41](#)
- FITZGERALD, K., BROWNE, L.M. & BUTLER, R. (2019). Using the agile software development lifecycle to develop a standalone application for generating colour magnitude diagrams. *Astronomy and Computing*, **28**, 100283. [v](#), [36](#), [44](#), [45](#), [58](#), [70](#), [114](#)
- FITZGERALD, K., HARVEY, E., KEAVENEY, N. & REDMAN, M. (2020). Introducing PYCROSS: PYCLOUDY rendering of SHAPE software for pseudo 3d ionisation modelling of nebulae. *Astronomy and Computing*, **32**, 100382. [v](#), [36](#), [37](#), [70](#), [73](#), [88](#), [91](#), [92](#), [98](#), [113](#), [114](#)

- FREW, D.J., BENTO, J., BOJII, I.S. & PARKER, Q.A. (2014). D_t serpentis: neither a symbiotic star nor a planetary nebula associate. *Monthly Notices of the Royal Astronomical Society*, **445**, 1605–1613. [25](#)
- GEHRZ, R.D., TRURAN, J.W., WILLIAMS, R.E. & STARRFIELD, S. (1998). Nucleosynthesis in classical novae and its contribution to the interstellar medium. *Publications of the Astronomical Society of the Pacific*, **110**, 3–26. [30](#)
- GEHRZ, R.D., EVANS, A., WOODWARD, C.E., HELTON, L.A., BANERJEE, D.P.K., SRIVASTAVA, M.K., ASHOK, N.M., JOSHI, V., EYRES, S.P.S., KRAUTTER, J., KUIN, N.P.M., PAGE, K.L., OSBORNE, J.P., SCHWARZ, G.J., SHENOY, D.P., SHORE, S.N., STARRFIELD, S.G. & WAGNER, R.M. (2018). The Temporal Development of Dust Formation and Destruction in Nova Sagittarii 2015#2 (V5668 SGR): A Panchromatic Study. *The Astrophysical Journal*, **858**, 78. [75](#)
- GESICKI, K., ZIJLSTRA, A.A. & MORISSET, C. (2016). 3D pyCloudy modelling of bipolar planetary nebulae: Evidence for fast fading of the lobes. *Astronomy & Astrophysics*, **585**, A69. [35](#)
- GONÇALVES, D.R., CORRADI, R.L.M. & MAMPASO, A. (2001). Low-Ionization Structures in Planetary Nebulae: Confronting Models with Observations. *The Astrophysical Journal*, **547**, 302–310. [14](#)
- GOODMAN, A.A. (2012). Principles of high-dimensional data visualization in astronomy. *Astronomische Nachrichten*, **333**, 505. [45](#)
- GREENFIELD, P. (2011). What Python Can Do for Astronomy. In I.N. Evans, A. Accomazzi, D.J. Mink & A.H. Rots, eds., *Astronomical Data Analysis Software and Systems XX*, vol. 442 of *Astronomical Society of the Pacific Conference Series*, 425. [44](#)

- GRUENDL, R.A., CHU, Y.H., ODWYER, I.J. & GUERRERO, M.A. (2001). Variable $h\alpha$ line emission from the central star of the helix nebula. *The Astrophysical Journal*, **122**, 308. [85](#)
- HARVEY, E., REDMAN, M.P., BOUMIS, P. & AKRAS, S. (2016). Modelling the structure and kinematics of the Firework nebula: The nature of the GK Persei nova shell and its jet-like feature. *Astronomy & Astrophysics*, **595**, A64. [42](#)
- HARVEY, E.J., REDMAN, M.P., DARNLEY, M.J., WILLIAMS, S.C., BERDYUGIN, A., PIROLA, V.E., FITZGERALD, K.P. & O’CONNOR, E.G.P. (2018). Polarimetry and spectroscopy of the “oxygen flaring” DQ Herculis-like nova: V5668 Sagittarii (2015). *Astronomy & Astrophysics*, **611**, A3. [v](#), [xiii](#), [36](#), [73](#), [74](#), [75](#), [76](#), [77](#), [78](#), [88](#), [98](#), [114](#)
- HARVEY, E.J., REDMAN, M.P., BOUMIS, P., AKRAS, S., FITZGERALD, K., DULAIMI, S., WILLIAMS, S.C., DARNLEY, M.J., LAM, M.C., KOPSACHEILLI, M. & DERLOPA, S. (2020). Two new nova shells associated with V4362 Sagittarii and DO Aquilae. *Monthly Notices of the Royal Astronomical Society*, **499**, 2959–2976. [v](#), [36](#), [73](#), [78](#), [80](#), [81](#), [88](#), [98](#), [114](#)
- HELTON, L.A., EVANS, A., WOODWARD, C.E. & GEHRZ, R.D. (2011). Atypical dust species in the ejecta of classical novae. In C. Joblin & A.G.G.M. Tielens, eds., *EAS Publications Series*, vol. 46 of *EAS Publications Series*, 407–412. [75](#)
- HENRY, R., KWITTER, K. & DUFOUR, R. (1999). Morphology and composition of the helix nebula. *The Astrophysical Journal*, **517**, 782. [85](#)
- HERNANZ, M. & JOSÉ, J. (2008). The recurrent nova rs oph: A possible scenario for type ia supernovae. *New Astronomy Reviews*, **52**, 386–389, astronomy with Radioactivities. VI. [31](#)
- HERWIG, F. (2005). Evolution of Asymptotic Giant Branch Stars. *Annu. Rev. Astron. Astrophys.*, **43**, 435–479. [8](#), [82](#)

- HORA, J.L., LATTER, W.B., SMITH, H.A. & MARENGO, M. (2006). Infrared observations of the helix planetary nebula. *The Astrophysical Journal*, **652**, 426. [86](#)
- HUBBLE, E.P. (1922). The source of luminosity in galactic nebulae. *The Astrophysical Journal*, **56**. [4](#)
- HUGGINS, W. & MILLER, W.A. (1864a). On the Spectra of Some of the Fixed Stars. *Philosophical Transactions of the Royal Society of London Series I*, **154**, 413–435. [4](#)
- HUGGINS, W. & MILLER, W.A. (1864b). On the Spectra of Some of the Nebulae. By William Huggins, F.R.A.S. A Supplement to the Paper “On the Spectra of Some of the Fixed Stars William Huggins F.R.A.S., and W. A. Miller, M.D., LL.D., Treas. and V.P.P.S.”. *Philosophical Transactions of the Royal Society of London Series I*, **154**, 437–444. [4](#)
- ILKIEWICZ, K. & MIKOLAJEWSKA, J. (2017). Distinguishing between symbiotic stars and planetary nebulae. *Astronomy & Astrophysics*, **606**, A110. [24](#), [25](#), [28](#)
- JONES, D. & BOFFIN, H.M.J. (2017). Binary stars as the key to understanding planetary nebulae. *Nature Astronomy*, **1**, 0117. [20](#), [23](#)
- KAFKA, S. & HONEYCUTT, R.K. (2004). Detecting Outflows from Cataclysmic Variables in the Optical. *The Astronomical Journal*, **128**, 2420–2429. [31](#)
- KENT, B.R. (2013). Visualizing Astronomical Data with Blender. *Publications of the Astronomical Society of the Pacific*, **125**, 731–748. [45](#)
- KHROMOV, G. (1989). Planetary nebulae. *Space Science Reviews*, **51**, 339–423. [85](#), [101](#)
- KONSTANTOPOULOS, I.S. (2015). The starfish diagram: Visualising data within the context of survey samples. *Astronomy and Computing*, **10**, 116–120. [45](#)

-
- KWOK, S. (2000). *The Origin and Evolution of Planetary Nebulae*. Cambridge Astrophysics, Cambridge University Press. [6](#), [9](#), [12](#), [82](#), [92](#)
- KWOK, S. (2003). Symbiotic Stars and Planetary Nebulae. In R.L.M. Corradi, J. Mikolajewska & T.J. Mahoney, eds., *Symbiotic Stars Probing Stellar Evolution*, vol. 303 of *Astronomical Society of the Pacific Conference Series*, 428. [24](#)
- KWOK, S., PURTON, C.R. & FITZGERALD, P.M. (1978). On the origin of planetary nebulae. *The Astrophysical Journal, Letters*, **219**, L125–L127. [19](#)
- LEAU, Y.B., LOO, W.K., THAM, W.Y. & TAN, S.F., eds. (2012). *Software Development Life Cycle AGILE vs Traditional Approaches*, vol. 37, International Conference on Information and Network Technology (ICINT), Singapore. [xv](#), [48](#), [52](#)
- LONGMORE, A. & TRITTON, S. (1980). A second list of new planetary nebulae found on united kingdom 1.2-m schmidt telescope plates. *Monthly Notices of the Royal Astronomical Society*, **193**, 521–524. [82](#)
- LURIDIANA, V., MORISSET, C. & SHAW, R. A. (2015). Pyneb: a new tool for analyzing emission lines - i. code description and validation of results. *Astronomy & Astrophysics*, **573**, A42. [40](#), [113](#)
- MAYALL, M.W. & CANNON, A.J. (1940). New Peculiar Spectra. *Harvard College Observatory Bulletin*, **913**, 7–7. [91](#)
- MCLAUGHLIN, D.B. (1939). The Light Curves of Novae (concluded). *Popular Astronomy*, **47**, 538. [30](#)
- MCLAUGHLIN, D.B. (1942). Spectral Stages of Novae. *apj*, **95**, 428. [75](#)
- MCMULLIN, J.P., WATERS, B., SCHIEBEL, D., YOUNG, W. & GOLAP, K. (2007). CASA Architecture and Applications. In R.A. Shaw, F. Hill & D.J. Bell, eds., *Astronomical Data Analysis Software and Systems XVI*, vol. 376 of *Astronomical Society of the Pacific Conference Series*, 127. [45](#)

- MEHDIPOUR, M., KAASTRA, J.S. & KALLMAN, T. (2016). Systematic comparison of photoionised plasma codes with application to spectroscopic studies of agn in x-rays. *Astronomy & Astrophysics*, **596**, A65. [41](#)
- MERC, J., GÁLIS, R. & WOLF, M. (2019). First Release of the New Online Database of Symbiotic Variables. *Research Notes of the American Astronomical Society*, **3**, 28. [25](#), [26](#)
- MISZALSKI, B., ACKER, A., MOFFAT, A.F.J., PARKER, Q.A. & UDALSKI, A. (2009a). Binary planetary nebulae nuclei towards the Galactic bulge. I. Sample discovery, period distribution, and binary fraction. *Astronomy & Astrophysics*, **496**, 813–825. [22](#)
- MISZALSKI, B., ACKER, A., PARKER, Q.A. & MOFFAT, A.F.J. (2009b). Binary planetary nebulae nuclei towards the Galactic bulge. II. A penchant for bipolarity and low-ionisation structures. *Astronomy & Astrophysics*, **505**, 249–263. [22](#)
- MISZALSKI, B., MANICK, R., MIKOAJEWSKA, J., VAN WINCKEL, H. & IKIEWICZ, K. (2018). Salt hrs discovery of the binary nucleus of the etched hourglass nebula mycn 18. *Publications of the Astronomical Society of Australia*, **35**. [92](#), [93](#), [95](#), [97](#), [98](#)
- MOMCHEVA, I. & TOLLERUD, E. (2015). Software Use in Astronomy: an Informal Survey. *ArXiv e-prints*. [43](#), [44](#)
- MORISSET, C. (2013). pyCloudy: Tools to manage astronomical Cloudy photoionization code. Astrophysics Source Code Library. [35](#), [41](#), [68](#), [77](#), [118](#)
- MORISSET, C., DELGADO-INGLADA, G. & FLORES-FAJARDO, N. (2015). A virtual observatory for photoionized nebulae: the Mexican Million Models database (3MdB). *Revista Mexicana de Astronomia y Astrofisica*, **51**, 103–120. [91](#)

- MULUMBA, P., GAIN, J., MARAIS, P. & WOUTD, P. (2015). Scientific Visualization of Radio Astronomy Data using Gesture Interaction. In A.R. Taylor & E. Rosolowsky, eds., *Astronomical Data Analysis Software and Systems XXIV (ADASS XXIV)*, vol. 495 of *Astronomical Society of the Pacific Conference Series*, 145. [46](#)
- MUNARI, U., CORRADI, R.L.M., SIVIERO, A., BALDINELLI, L. & MAITAN, A. (2013). Discovery of a planetary nebula surrounding the symbiotic star dt serpentis. *Astron. Astrophys.*, **558**, A2. [25](#)
- NORDHAUS, J. & BLACKMAN, E.G. (2006). Low-mass binary-induced outflows from asymptotic giant branch stars. *Monthly Notices of the Royal Astronomical Society*, **370**, 2004–2012. [xii](#), [21](#), [22](#)
- NORDHAUS, J. & BLACKMAN, E.G. (2006). Low-mass binary-induced outflows from asymptotic giant branch stars. *Monthly Notices of the Royal Astronomical Society*, **370**, 2004–2012. [33](#)
- O'BRIEN, T.J. & LLOYD, H.M. (1994). Shock-heated gas in the outbursts of classical novae. *Astrophysics and Space Science*, **216**, 167–172. [33](#)
- O'CONNOR, J.A., REDMAN, M.P., HOLLOWAY, A.J., BRYCE, M., LOPEZ, J.A. & MEABURN, J. (2000). The hypersonic, bipolar, knotty outflow from the engraved hourglass planetary nebula MyCn 18. *The Astrophysical Journal*, **531**, 336–344. [97](#)
- O'DELL, C.R. & HANDRON, K.D. (1996). Cometary Knots in the Helix Nebula. *The Astronomical Journal*, **111**, 1630. [14](#)
- O'DELL, C.R., BALICK, B., HAJIAN, A.R., HENNEY, W.J. & BURKERT, A. (2002). Knots in Nearby Planetary Nebulae. *The Astronomical Journal*, **123**, 3329–3347. [14](#)
- OSAKI, Y. (1996). Dwarf-nova outbursts. *Publications of the Astronomical Society of the Pacific*, **108**, 39–60. [31](#)

- OSTERBROCK, D.E. & FERLAND, G.J. (2006). *Astrophysics of gaseous nebulae and active galactic nuclei*. University Science Books, 2nd edn. [32](#), [39](#), [74](#), [82](#), [105](#), [107](#)
- PACZYŃSKI, B. (1971a). Evolution of Single Stars. VI. Model Nuclei of Planetary Nebulae. *Acta Astronautica*, **21**, 417. [8](#)
- PACZYŃSKI, B. (1971b). The Formation of Planetary Nebulae. *Astrophysical Letters*, **9**, 33. [8](#)
- PARKER, Q.A., ACKER, A., FREW, D.J., HARTLEY, M., PEYAUD, A.E.J., OCHSENBEIN, F., PHILLIPPS, S., RUSSEIL, D., BEAULIEU, S.F., COHEN, M., KÖPPEN, J., MISZALSKI, B., MORGAN, D.H., MORRIS, R.A.H., PIERCE, M.J. & VAUGHAN, A.E. (2006a). The Macquarie/AAO/Strasbourg H α Planetary Nebula Catalogue: MASH. *Monthly Notices of the Royal Astronomical Society*, **373**, 79–94. [21](#)
- PARKER, Q.A., ACKER, A., FREW, D.J., HARTLEY, M., PEYAUD, A.E.J., PHILLIPPS, S., RUSSEIL, D., BEAULIEU, S.F., COHEN, M., KÖPPEN, J., MARCOUT, J., MISZALSKI, B., MORGAN, D.H., MORRIS, R.A.H., OCHSENBEIN, F. & PIERCE, M.J. (2006b). VizieR Online Data Catalog: MASH Catalogues of Planetary Nebulae (Parker+ 2006-2008). *VizieR Online Data Catalog*, **5127**. [19](#)
- PEIMBERT, M. (1978). Chemical abundances in planetary nebulae. In Y. Terzian, ed., *Planetary Nebulae*, vol. 76 of *IAU Symposium*, 215–223. [18](#)
- PEIMBERT, M., PEIMBERT, A. & DELGADO-INGLADA, G. (2017). Nebular Spectroscopy: A Guide on Hii Regions and Planetary Nebulae. *Publications of the Astronomical Society of the Pacific*, **129**, 082001. [18](#), [108](#), [111](#), [116](#)
- PERRINE, C.D. (1929). The Origin and Internal Motions of the Planetary Nebulae. *Astronomische Nachrichten*, **237**, 89. [5](#)

- PERSSON, M.V. (2014). Proposed internal structure of AGB star. Accessed: 2018-03-26. [9](#)
- PHILLIPS, J.P., CUESTA, L.C. & RAMOS-LARIOS, G. (2010). Mapping and spectroscopy of the planetary nebula NGC 7009 in the visual and infrared. *Monthly Notices of the Royal Astronomical Society*, **409**, 881–902. [15](#)
- PRIALNIK, D. (2009). *An Introduction to the Theory of Stellar Structure and Evolution*. Cambridge University Press. [6](#), [8](#), [9](#), [10](#), [82](#)
- PRIALNIK, D. & KOVETZ, A. (1995). An Extended Grid of Multicycle Nova Evolution Models. *The Astrophysical Journal*, **445**, 789. [74](#)
- REHKOPF, M. (2017). Atlassian agile coach - user stories. <https://www.atlassian.com/agile/project-management/user-stories>, accessed: 2018-09-13. [49](#)
- SABIN, L., GÓMEZ-MUÑOZ, M.A., GUERRERO, M.A., ZAVALA, S., RAMOS-LARIOS, G., VÁZQUEZ, R., CORRAL, L., BLANCO CÁRDENAS, M.W., GUILLÉN, P.F., OLGUÍN, L., MORISSET, C. & NAVARRO, S. (2017). Catching a grown-up starfish planetary nebula - I. Morpho-kinematical study of PC 22. *Monthly Notices of the Royal Astronomical Society*, **467**, 3056–3065. [43](#)
- SAHAI, R., DAYAL, A., WATSON, A.M., TRAUGER, J.T., STAPELFELDT, K.R., BURROWS, C.J., III, J.S.G., SCOWEN, P.A., HESTER, J.J., EVANS, R.W., BALLESTER, G.E., CLARKE, J.T., CRISP, D., GRIFFITHS, R.E., HOESSEL, J.G., HOLTZMAN, J.A., KRIST, J. & MOULD, J.R. (1999). The Etched Hourglass Nebula MyCn 18. I. HUBBLE SPACE TELESCOPE Observations. *The Astronomical Journal*, **118**, 468–476. [xiii](#), [92](#), [93](#), [94](#), [95](#), [97](#), [100](#), [101](#), [102](#), [104](#), [105](#), [111](#)
- SAHAI, R., MORRIS, M., CONTRERAS, C.S. & CLAUSSEN, M. (2007). Pre-planetary nebulae: A hubble space telescope imaging survey and a new morphological classification system. *The Astronomical Journal*, **134**, 2200. [12](#)

- SAHAI, R., MORRIS, M.R. & VILLAR, G.G. (2011). Young Planetary Nebulae: Hubble Space Telescope Imaging and a New Morphological Classification System. *The Astronomical Journal*, **141**, 134. [xv](#), [12](#), [13](#)
- SAMI, M. (2012). Choosing the right software development life cycle model. <https://melsatar.blog/2012/03/21/choosing-the-right-software-development-life-cycle-model/>, accessed: 2017-09-20. [xv](#), [48](#), [52](#)
- SANTAMARÍA, E., GUERRERO, M.A., RAMOS-LARIOS, G., TOALÁ, J.A., SABIN, L., RUBIO, G. & QUINO-MENDOZA, J.A. (2020). Angular expansion of nova shells. *The Astrophysical Journal*, **892**, 60. [xii](#), [30](#), [33](#), [34](#), [35](#)
- SANTANDER-GARCÍA, M., CORRADI, R.L.M., MAMPASO, A., MORISSET, C., MUNARI, U., SCHIRMER, M., BALICK, B. & LIVIO, M. (2008). Hen 2-104: a close-up look at the southern crab*. *Astron. Astrophys.*, **485**, 117–126. [26](#), [27](#)
- SANTANDER-GARCIA, M., BUJARRABAL, V., ALCOLEA, J., CASTRO-CARRIZO, A., SÁNCHEZ CONTRERAS, C., QUINTANA-LACACI, G., CORRADI, R.L.M. & NERI, R. (2017). ALMA high spatial resolution observations of the dense molecular region of NGC 6302. *Astronomy & Astrophysics*, **597**, A27. [43](#)
- SCHÖENBERNER, D. (1979). Asymptotic giant branch evolution with steady mass loss. *Astronomy & Astrophysics*, **79**, 108–114. [8](#)
- SCHÖENBERNER, D. (1981). Late stages of stellar evolution - Central stars of planetary nebulae. *Astronomy & Astrophysics*, **103**, 119–130. [8](#)
- SCHÖENBERNER, D. (1987). Mass loss and the transformation of AGB stars into central stars of planetary nebulae. In S. Kwok & S.R. Pottasch, eds., *Late Stages of Stellar Evolution*, vol. 132 of *Astrophysics and Space Science Library*, 337–346. [8](#)

- SCHWARZ, H.E., CORRADI, R.L.M. & MELNICK, J. (1992). A catalogue of narrow band images of planetary nebulae. *Astronomy & Astrophysics, Supplement*, **96**, 23–113. [95](#)
- SCOTT, A.D. (2000). Nova outbursts on rotating oblate white dwarfs. *Monthly Notices of the Royal Astronomical Society*, **313**, 775–782. [33](#)
- SHARA, M.M., YARON, O., PRIALNIK, D., KOVETZ, A. & ZUREK, D. (2010). An Extended Grid of Nova Models. III. Very Luminous, Red Novae. *The Astrophysical Journal*, **725**, 831–841. [74](#)
- SHAW, R.A. (2012). Shape, structure, and morphology in planetary nebulae. In *IAU Symposium*, vol. 283 of *IAU Symposium*, 156–163. [15](#), [16](#)
- SHKLOVSKY, I.S. (1956a). A new scale of distances of planetary nebulae. *Astronomicheskii Zhurnal*, **33**, 222–235. [5](#)
- SHKLOVSKY, I.S. (1956b). The nature of planetary nebulae and their nuclei. *Astronomicheskii Zhurnal*, **33**, 315–329. [5](#)
- SHKLOVSKY, I.S. (1957). On the nature of planetary nebulae. In G.H. Herbig, ed., *Non-stable stars*, vol. 3 of *IAU Symposium*, 83. [5](#)
- SIEGERT, T., COC, A., DELGADO, L., DIEHL, R., GREINER, J., HERNANZ, M., JEAN, P., JOSE, J., MOLARO, P., PLEINTINGER, M., SAVCHENKO, V., STARRFIELD, S., TATISCHEFF, V. & WEINBERGER, C. (2018). Gamma-ray observations of Nova Sgr 2015 No. 2 with INTEGRAL. *Astronomy & Astrophysics*, **615**, A107. [75](#), [78](#)
- SOKER, N. (1992). Planetary nebulae. *Scientific American*, **266**, 78–85. [xii](#), [19](#)
- SOKER, N. (1996). What Planetary Nebulae Can Tell Us about Planetary Systems. *The Astrophysical Journal, Letters*, **460**, L53. [20](#)
- SOKER, N. (1997). Properties That Cannot Be Explained by the Progenitors of Planetary Nebulae. *The Astrophysical Journal, Supplement*, **112**, 487–505. [xv](#), [20](#), [21](#), [97](#)

- SOKER, N. (2017). Energizing the last phase of common-envelope removal. *Monthly Notices of the Royal Astronomical Society*, **471**, 4839–4843. [97](#)
- STANGHELLINI, L., CORRADI, R.L.M. & SCHWARZ, H.E. (1993). The correlations between planetary nebula morphology and central star evolution. *Astronomy & Astrophysics*, **279**, 521–528. [12](#)
- STANGHELLINI, L., SHAW, R.A. & VILLAVER, E. (2008). The magellanic cloud calibration of the galactic planetary nebula distance scale. *The Astrophysical Journal*, **689**, 194–202. [95](#)
- STARRFIELD, S., ILIADIS, C. & HIX, W.R. (2016). The thermonuclear runaway and the classical nova outburst. *Publications of the Astronomical Society of the Pacific*, **128**, 051001. [30](#)
- STEFFEN, W. & KONING, N. (2011). Shape 2010. In *Asymmetric Planetary Nebulae 5 Conference*, Bowness-on-Windermere, UK. ASP Conference Series. [3](#), [35](#)
- STEFFEN, W., KONING, N., WENGER, S., MORISSET, C. & MAGNOR, M. (2011). Shape: A 3D Modeling Tool for Astrophysics. *IEEE Transactions on Visualization and Computer Graphics, Volume 17, Issue 4, p.454-465*, **17**, 454–465. [42](#)
- SURACE, J., LAHER, R., MASCI, F., GRILLMAIR, C. & HELOU, G. (2015). The Palomar Transient Factory: High Quality Realtime Data Processing in a Cost-Constrained Environment. In A.R. Taylor & E. Rosolowsky, eds., *Astronomical Data Analysis Software and Systems XXIV (ADASS XXIV)*, vol. 495 of *Astronomical Society of the Pacific Conference Series*, 197. [45](#)
- SYBILSKI, P.W., PAWŁASZEK, R., KOZŁOWSKI, S.K., KONACKI, M., RATAJCZAK, M. & HELMINIAK, K.G. (2014). Software for autonomous astronomical observatories: challenges and opportunities in the age of big data. In *Software and Cyberinfrastructure for Astronomy III*, vol. 9152 of *Proceedings of SPIE*, 91521C. [45](#)

- TAYLOR, A.R. & ROSOLOWSKY, E., eds. (2015). *Astronomical Data Analysis Software and Systems XXIV (ADASS XXIV)*, vol. 495 of *Astronomical Society of the Pacific Conference Series*. [45](#)
- TORRES-PEIMBERT, S. (2015). Chemical composition of planetary nebulae: The abundance discrepancy problem. In *American Institute of Physics Conference Series*, vol. 1697 of *American Institute of Physics Conference Series*, 040003. [18](#)
- TSAMIS, Y.G., BARLOW, M.J., LIU, X.W., DANZIGER, I.J. & STOREY, P.J. (2003). A deep survey of heavy element lines in planetary nebulae I. Observations and forbidden-line densities, temperatures and abundances. *Monthly Notices of the Royal Astronomical Society*, **345**, 186–220. [xv](#), [17](#), [110](#)
- TSEBRENKO, D. & SOKER, N. (2013). Type ia supernovae inside planetary nebulae: shaping by jets. *Monthly Notices of the Royal Astronomical Society*, **435**, 320328. [32](#)
- TYNDALL, A., JONES, D., BOFFIN, H., MISZALSKI, B., FAEDI, F., LLOYD, M., BOUMIS, P., LÓPEZ, J., MARTELL, S., POLLACCO, D. *et al.* (2013). Two rings but no fellowship: Lotr 1 and its relation to planetary nebulae possessing barium central stars. *Monthly Notices of the Royal Astronomical Society*, **436**, 2082–2095. [xv](#), [82](#), [83](#), [84](#), [85](#), [86](#)
- VALLEJO, J.C., LOPEZ, F.P., ORTIZ, I., MACFARLANE, A., OSUNA, P., GILL, R. & CASALE, M. (2015). Flexible and Modular Design for the Bepi-Colombo Science Operations Control System. In A.R. Taylor & E. Rosolowsky, eds., *Astronomical Data Analysis Software and Systems XXIV (ADASS XXIV)*, vol. 495 of *Astronomical Society of the Pacific Conference Series*, 277. [45](#)
- VAN HOOFF, P.A.M., MARTIN, P.G. & FERLAND, G.J. (2000). Current Development of Cloudy. In J. Franco, L. Terlevich, O. López-Cruz & I. Aretxaga, eds., *Cosmic Evolution and Galaxy Formation: Structure, Interactions, and*

- Feedback*, vol. 215 of *Astronomical Society of the Pacific Conference Series*, 220. [3](#), [35](#), [41](#)
- VANDERPLAS, J., CONNOLLY, A.J., IVEZIC, Z. & GRAY, A. (2012). Introduction to astroML: Machine learning for astrophysics. [45](#)
- WANG, B. (2018). Mass-accreting white dwarfs and type ia supernovae. *Research in Astronomy and Astrophysics*, **18**, 049. [31](#)
- WANG, B. & HAN, Z. (2012). Progenitors of type ia supernovae. *New Astronomy Reviews*, **56**, 122–141. [31](#)
- WARNER, B. (1995). *Cataclysmic Variable Stars*. Cambridge Astrophysics, Cambridge University Press. [31](#)
- WHITELOCK, P.A. (1987). Symbiotic Miras. *Publications of the Astronomical Society of the Pacific*, **99**, 573–591. [26](#)
- WILLIAMS, R. (2012). Origin of the “He/N” and “Fe II” Spectral Classes of Novae. *The Astronomical Journal*, **144**, 98. [74](#)
- YARON, O., PRIALNIK, D., SHARA, M.M. & KOVETZ, A. (2005). An Extended Grid of Nova Models. II. The Parameter Space of Nova Outbursts. *The Astrophysical Journal*, **623**, 398–410. [74](#)